
Search for diboson resonances with CMS and Pixel Barrel Detector Calibration and Upgrade

Dissertation

zur

Erlangung der naturwissenschaftlichen Doktorwürde
(Dr. sc. nat.)

vorgelegt der Mathematisch-naturwissenschaftlichen Fakultät
der
Universität Zürich



von
Jennifer Ngadiuba

Promotionskomitee

Prof. Dr. Benjamin Kilminster
Prof. Dr. Florencia Canelli
Prof. Dr. Laura Baudis
Prof. Dr. Ueli Straumann

Zürich 2016

Contents

CHAPTER 1

Introduction

The Standard Model and beyond

2.1 The Standard Model

2.1.1 Particles and interactions

2.1.2 Spontaneous symmetry breaking

2.1.3 The Higgs mechanism

2.1.4 The Higgs boson discovery at LHC

2.2 The hierarchy problem and other SM limitations

2.3 Theories of new physics

2.3.1 Warped Extra dimensions

2.3.2 Compositeness

2.3.3 Heavy vector triplet

The CMS Experiment at the LHC

3.1 The Large Hadron Collider

The Large Hadron Collider (LHC) [?] is a proton-proton (pp) collider located at the European Particle Physics Laboratory (CERN) near Geneva, Switzerland. It is situated in the former CERN Large Electron-Positron Collider (LEP) tunnel with a circumference of 27 km about 100 m under ground crossing the border between France and Switzerland. A hadron collider has been chosen to allow higher center-of-mass energies (\sqrt{s}) compared to electron-positron colliders, the latter limited by synchrotron radiation due to the low mass of the particles to be accelerated. High centre of mass energies are required for the production of heavy SM particles such as the top quark and the Higgs boson, and to search for new BSM interactions at the TeV scale. For this purpose, the LHC is designed to produce pp collisions up to a center-of-mass energy of 14 TeV, superseding previous high energy hadron colliders by a factor of 7. In addition to colliding protons, the LHC is also capable of accelerating and colliding heavy nuclei, which is, however, not considered in this work.

The LHC is the final element in a succession of machines that accelerate protons to increasingly higher energies. Protons, obtained from a hydrogen source, are first accelerated by a linear accelerator (LINAC 2) to energies of 50 MeV. The beam is then injected into the Proton Synchrotron Booster (PSB), which accelerates the protons to 1.4 GeV, followed by the Proton Synchrotron (PS), which pushes the beam to 25 GeV. Protons are then sent to the Super Proton Synchrotron (SPS) where they are accelerated to 450 GeV. Finally, the beam is injected in the LHC ring, where it completes several revolutions to reach the targeted energy. The LHC ring and the acceleration chain are sketched in Fig. ??.

Inside the ring, the two proton beams circulate in opposite directions in two tubes kept at ultrahigh vacuum, referred as beam pipes. The acceleration of protons inside LHC is made by radio-frequency cavities (400 MHz), giving a 492 keV energy gain per revolution, with a 7 keV loss per turn due to synchrotron radiation. It takes 4 minutes and 20 seconds to fill each LHC ring, and 20 minutes for the protons to reach their maximum energy of 7 TeV. The maximum energy of the protons is limited by the strength of the magnetic field required for keeping the protons inside the ring. For 7 TeV-protons a magnetic field of 8.3 T has to be produced, which can only be reasonably obtained by superconducting magnets. The ring is equipped with 1232 dipole magnets for bending and 392 quadrupole magnets for focussing made of niobium-titanium (NbTi), which are cooled down to a temperature of 1.9 K with the help of super-fluid helium. After acceleration the protons move through the ring in separate bunches of protons with a fixed spatial separation.

The LHC ring has four interaction points at which the two counter rotating beams are made to cross and located in the center of the four LHC experiments. Just prior to collision, particles from the incoming beams must be squeezed closer together in order to maximize the chances of interaction. For this purpose, a system of three quadrupole magnets, so-called inner triplet, is located at both sides of each interaction point, which squeeze the beams and lead them to collisions in the center of the detector. Inner triplets tighten the beam, making it 12.5 times narrower from 0.2 mm down to 16 μm across.

Besides the high center-of-mass energy required for the production of heavy particles, a high event rate has to be obtained to allow the discovery of processes with low production cross sections. The instantaneous luminosity \mathcal{L} characterizes the interaction rate. For a process with a cross section σ , the interaction rate is given by

$$\frac{dN_{ev}}{dt} = \sigma \mathcal{L}. \quad (3.1)$$

The instantaneous luminosity depends only on the beam parameters and can be written for a Gaussian beam distribution as:

$$\mathcal{L} = \frac{N_b^2 n_b f_{rev} \gamma_r}{4\pi \sigma_x \sigma_y}, \quad (3.2)$$

where N_b is the number of particles per bunch, n_b the number of bunches per beam, f_{rev} the revolution frequency, γ_r the relativistic gamma factor, while σ_x and σ_y characterize the widths of the transverse beam profiles in the horizontal and vertical direction, respectively. The number of interaction events in a period of running time of the collider can be derived as

$$N_{ev} = \sigma \int \mathcal{L} dt = \sigma L, \quad (3.3)$$

where L is called the integrated luminosity. It is a measurement of the collected data size and it is usually expressed in inverse of cross section.

The LHC beams can reach very high luminosity with a high frequency bunch crossing and a high density of protons per bunch. In the ring, 2808 bunches of $1.15 \cdot 10^{11}$ protons are circulated, with an average length of 7.5 cm, a width of about 16 μm and a bunch spacing of 25 ns (collision frequency of 40 MHz). This corresponds to the design instantaneous luminosity of $10^{34} \text{ cm}^{-2} \text{ s}^{-1}$ for pp collisions, which supersedes by a factor of 100 the luminosity reached by previous hadron colliders.

Proton collisions take place in four points of the LHC tunnel where the four main experiments are located: ATLAS (*A Toroidal LHC ApparatuS*) [?], CMS (*Compact Muon Solenoid*) [?], LHCb (*LHC beauty experiment*) [?] and ALICE (*A Lead Ion Collider Experiment*) [?]. ATLAS and CMS are general purpose experiments, designed to get an extensive study of SM and BSM physics and to operate at the design luminosity. The LHCb experiment is instead optimized for bottom quark physics studies while the ALICE experiment is dedicated to the study of the lead-lead collisions at the design luminosity of $10^{27} \text{ cm}^{-2} \text{ s}^{-1}$.

LHC operation officially started at the beginning of September 2008 but it was interrupted after a short period, due to the breakdown of superconducting magnets. The collider has been reactivated in November 2009 with first pp collisions at $\sqrt{s} = 900$ GeV, officially starting a new era in the particle physics experiments. The operating center-of-mass energies in pp collisions have so far been 7 TeV in 2010-2011, 8 TeV in 2012 and 13 TeV in 2015-2016. The 7 and 8 TeV periods together make out the *LHC Run 1*, while the 13 TeV period is called the *LHC Run 2*. The work presented in this document is based on both dataset collected at 8 TeV in 2012 and at 13 TeV in 2015.

In the whole Run 1, the LHC operated with a 50 ns bunch spacing. The peak of instantaneous luminosity in 2011 has been $\sim 0.4 \cdot 10^{34} \text{ cm}^{-2} \text{ s}^{-1}$ with a total delivered integrated luminosity of 6.1 fb^{-1} [?]. In 2012 the beam energy increased to 4 TeV per beam with a peak luminosity of $\sim 0.8 \cdot 10^{34} \text{ cm}^{-2} \text{ s}^{-1}$ and 23.3 fb^{-1} delivered integrated luminosity by the end of that year [?]. The increment of the instantaneous luminosity leads to a no more negligible number of simultaneous interactions per bunch crossing, the so-called *pileup* (PU) events.

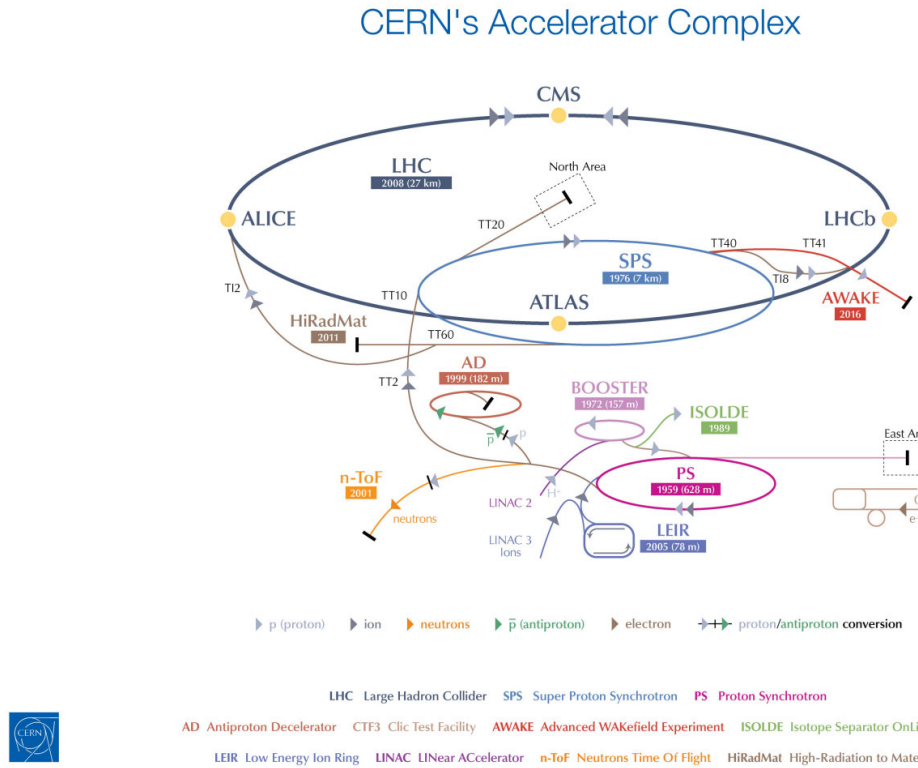


Figure 3.1: The LHC scheme together with its injection chain and the locations of the four main experiments ATLAS, CMS, LHCb and ALICE [?].

It depends on the cross section of inelastic collisions (75 mb at $\sqrt{s} = 8 \text{ TeV}$ [?]) and it is directly linked to the instantaneous luminosity. The average PU of the data collected in 2012 is equal to 21 (Fig. ??) while it has been around 15 in 2011 [?].

A shut-down period for the LHC (LS1) occurred in the whole 2013 and 2014, where upgrades and technical improvements have been performed in order to reach the designed instantaneous luminosity and center-of-mass energy. On March, 21st 2015 the first $p\bar{p}$ collisions at $\sqrt{s} = 13 \text{ TeV}$ has been obtained, a new record-breaking energy. For the first three months the machine operated with 50 ns bunch spacing while, from August 2015, it has been reduced to the designed 25 ns and the number of bunches per beam has been increased. The first part of this Run 2 phase ended on November 2015 with a total delivered integrated luminosity of 4.2 fb^{-1} and a peak luminosity of $\sim 0.5 \cdot 10^{34} \text{ cm}^{-2} \text{ s}^{-1}$ with an average pileup of 12 [?].

The LHC Run 2 has been restarted in April 2016, after an end-of-the-year technical stop, reaching a peak luminosity of $\sim 1.2 \cdot 10^{34} \text{ cm}^{-2} \text{ s}^{-1}$ (change this number at some point). The machine has remained in operation at $\sqrt{s} = 13 \text{ TeV}$ for the whole year with a total delivered integrated luminosity of 30 fb^{-1} (change this number at some point). Accordingly to the current LHC schedule, the Run 2 will proceed up to the end of 2018 with a total expected integrated luminosity of 100 fb^{-1} . The data collected in 2016 are not considered in this work.

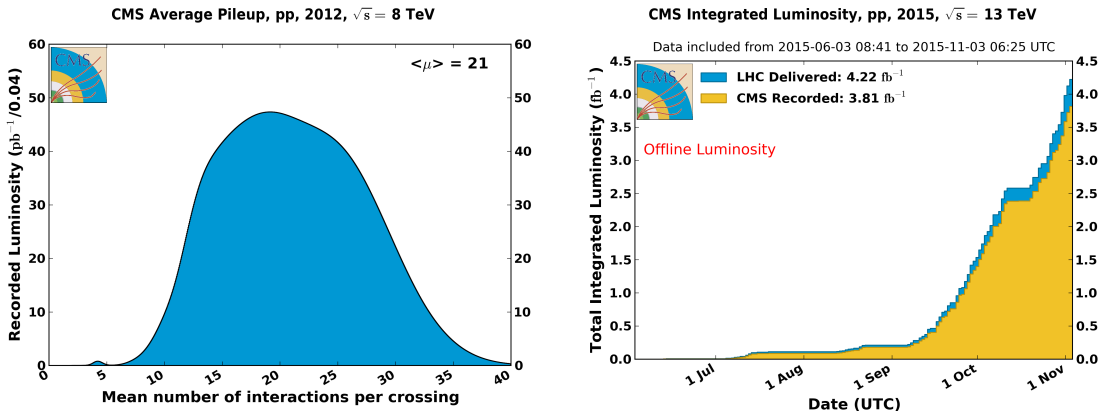


Figure 3.2: Mean number of interactions per bunch crossing in data collected in 2012 by the CMS experiment at LHC (left). Cumulative luminosity versus day (right) delivered by LHC (blue) in 2015; the off-line luminosity recorded by the CMS experiment is also reported (orange). [?]

3.2 The CMS Detector

The CMS detector is a general purpose detector installed 100 m underground at the LHC interaction point 5 (P5) near the village of Cessy in France. It has been designed to exploit the different properties of the wide range of particles and phenomena produced in high-energy collisions in the LHC. The design of the CMS detector is driven by the challenges of a physics experiment in the LHC environment. Many of the physics benchmark channels have a small cross section and the background from QCD jet production is overwhelmingly dominant. In order to achieve high rejection power with an optimal efficiency for rare channels, the detector has to be able to reconstruct the primary interaction entirely and to reduce the influence of overlapping events. Therefore, one needs to collect all possible information on the particles passing through the detector. Since these have different properties, a mixture of sub-detectors is required for a complete event reconstruction. The reconstruction of lepton signatures is essential for the extraction of rare processes and an excellent muon and electron identification and momentum resolution is desired. A precise measurement of secondary vertices and impact parameters is necessary for an efficient identification of heavy flavor quarks and τ -leptons. Moreover, a large hermetic geometric coverage is preferred, which allows for a precise estimate of the transverse momentum carried away by invisible particles through the sum of all visible particles.

The high peak luminosities of LHC lead to large pileup imposing further challenges to the design. As a consequence of pileup, the products of an interaction under study may be confused with those from other interactions in the same bunch crossing. This effect can be reduced by using high-granularity detectors resulting in low occupancy. In addition, the short bunch crossing requires fast response time and good time resolution of each detector element in order to discriminate the interaction under study from the interactions occurring in neighboring bunch crossings. Hence, a large number of detector channels and an excellent synchronization among them are required. Another challenge arises from the large flux of particles near the interaction point which leads to high radiation levels and the need of radiation hard detectors and front-end electronics.

Figure ?? shows the layout of the CMS detector. The detector is built in a cylindrical structure composed of a barrel in the center and endcaps at both sides. This structure is

21.6-m-long, 14.6-m in circumference and 12500-tons-heavy. The detector design and layout was driven by the choice of the magnetic field configuration. Large bending power is needed for a precise measurement of the momentum of high-energy charged particles. Within the CMS detector this is achieved by a superconducting solenoid with a length of 12.9 m and an inner diameter of 5.9 m generating a magnetic field of 4 T. The bore of the magnet coil is large enough to accommodate the inner tracker and the calorimetry inside. The inner tracker consists of a pixel and a strip detector both made out of Silicon, and it is the key component of CMS to measure the momenta of charged particles and identify primary and secondary vertices. The calorimetry system comprises a crystal electromagnetic calorimeter (ECAL) and a brass and scintillator hadronic calorimeter (HCAL), which provide information on the energies and directions of all charged and neutral particles. Outside the magnet are the large muon detectors, which, integrated inside the return yokes of the magnet, provide identification of muons and measurement of their momenta.

For the description of the CMS detector the following coordinate system is used. The origin is centered at the nominal collision point inside the experiment with the y -axis pointing vertically upward, the x -axis pointing radially inward toward the center of the LHC, and the z -axis points along the beam direction. The azimuthal angle ϕ is measured from the x -axis in the x - y plane. The polar angle θ is measured from the z -axis. Pseudorapidity is defined as $\eta = -\ln \tan(\theta/2)$. Thus, the momentum and energy measured transverse to the beam direction, denoted by p_T and E_T , respectively, are computed from the x and y components.

In the following sections the three main components of the CMS detector will be described together with a section on the triggering system.

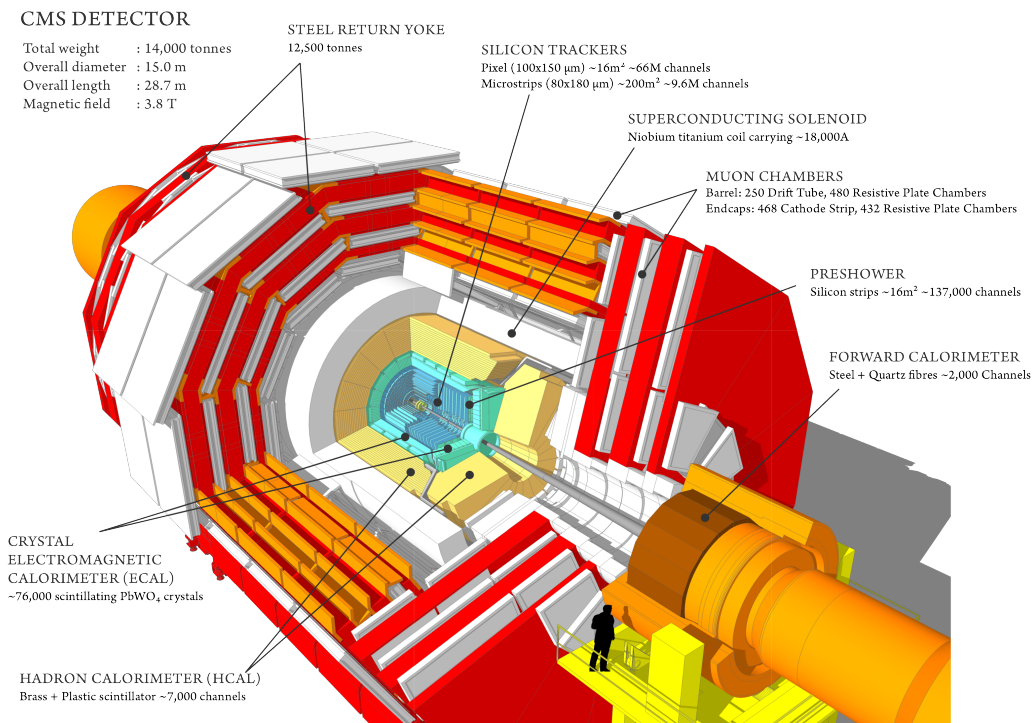


Figure 3.3: Layout of the CMS experiment and its sub-detectors.

3.2.1 Tracking detectors

The tracking system of CMS (Fig. ??) is designed to provide a precise and efficient measurement of the trajectories of charged particles emerging from the LHC collisions, as well as a precise reconstruction of secondary vertices [?]. It surrounds the interaction point and has a length of 5.8 m and a diameter of 2.5 m providing coverage up to $|\eta| < 2.5$. In order to achieve high tracking efficiency at the high luminosities of LHC, a detector technology featuring granularity, speed and radiation hardness is required. Furthermore, the material budget of the tracking system has to be as low as possible in order to avoid a worsening of the tracking efficiency and resolution due to material interaction effects of the charged particle, such as multiple scattering, bremsstrahlung, photon conversion or nuclear interactions. These requirements lead to a tracker design entirely based on silicon detector technology. With about 200 m^2 of active silicon area the CMS tracker is the largest silicon tracker ever built. It is divided into a pixel detector close to the interaction region and a strip detector in the outer region. At LHC design luminosity more than 1000 particles are hitting the tracking volume in each bunch crossing. This leads to a hit rate density of 1 MHz/mm^2 at a radius of 4 cm which imposes severe challenges to the design of the tracking detectors. With a pixel size of $100 \times 150 \mu\text{m}^2$ in $r\text{-}\phi$ and z , respectively, an occupancy of the order of 10^{-4} per pixel and LHC bunch crossing can be achieved. The hit rate density falls with the distance from the interaction point to 60 kHz/mm^2 at a radius of 22 cm and to 3 kHz/mm^2 at a radius of 115 cm. Therefore, at intermediate radii (20–55 cm), silicon micro-strip detectors are used, with a typical cell length of 10 cm and a pitch of $80 \mu\text{m}$. At the outermost radii (55–110 cm) the strip size can be further increased to $25 \text{ cm} \times 180 \mu\text{m}$. With this choice an occupancy of less than 3% is maintained in the strip detector. However, the strip capacitance scales with its length and therefore the electronics noise is a linear function of the strip length as well, becoming not negligible in the outermost region where the strip size is the largest. In order to maintain a good signal to noise ratio of well above 10, CMS uses thicker silicon sensors for the outer tracker region ($500 \mu\text{m}$ thickness as opposed to the $320 \mu\text{m}$ in the inner tracker) with correspondingly higher signal. To mitigate the radiation damage effects and prolong the lifetime of the detector modules, the tracking detectors are designed to run at subzero temperatures. The cooling is established using a mono-phase liquid cooling system with C_6F_{14} as cooling fluid. The whole tracker system operated at $+4^\circ\text{C}$ during Run 1. After this phase, several improvements have been implemented and an operative temperature of -15°C is currently maintained for Run 2.

The pixel detector is built from 3 barrel layers at radii of 4.4, 7.3 and 10.2 cm (BPix) and two end disks (FPix) on each side at a distance of $z = \pm 34.5, \pm 46.5 \text{ cm}$ from the interaction point. It consists of 1440 segmented silicon sensor modules with a total of 66 million readout channels covering an area of about 1 m^2 . The pixel detector is essential for the reconstruction of secondary vertices from bottom quarks and τ leptons decays. It provides precise tracking points in $r\text{-}\phi$ and z and therefore is responsible for a small impact parameter resolution that is important for good secondary vertex reconstruction. This is achieved thanks to the read out of the analog pulse height information. The sensor surface in the barrel layers is parallel to the magnetic fields, hence the charge carriers produced by a particle traversing experience a Lorentz drift, which leads to charge spreading over more than one pixel. The analog pulse height information can be used to calculate a center of gravity of the charge distribution improving the hit information. The forward detectors are tilted at 20° in a turbine-like geometry to induce charge-sharing. As shown in Fig. ??, a spatial resolution of $10 \mu\text{m}$ in the transverse plane and $30 \mu\text{m}$ in the longitudinal plane can be achieved for BPix. For FPix a spatial resolution of $20 \mu\text{m}$ is obtained. A detailed description of the design and

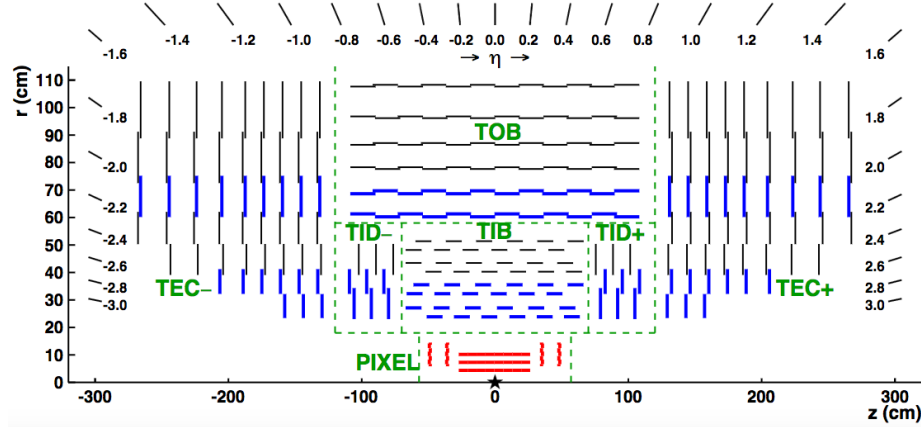


Figure 3.4: Longitudinal section of half of the CMS Tracker system; the different detector types are indicated.

the functioning of the CMS pixel barrel detector is given in Chapter ??.

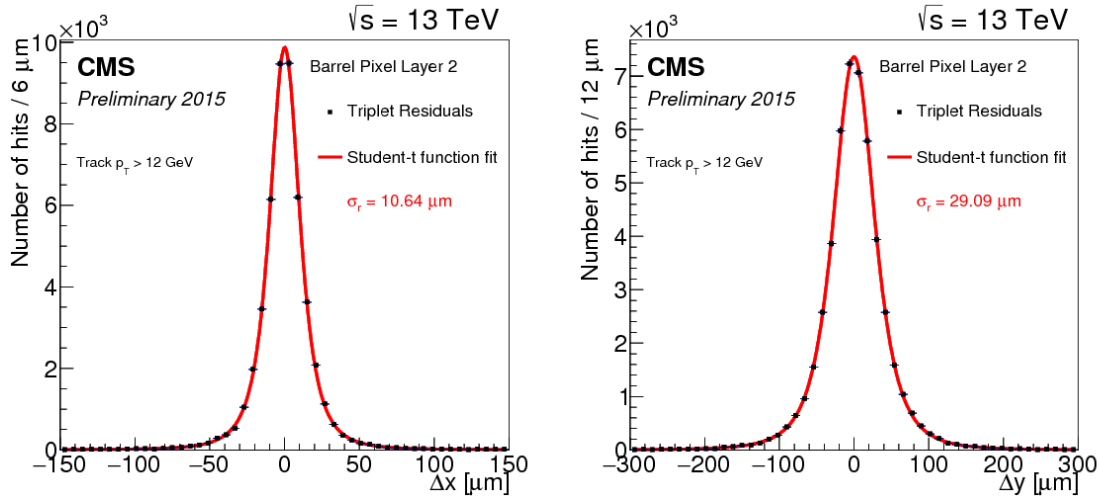


Figure 3.5: Distribution of hit residuals on pixel barrel layer 2 in the transverse (left) and longitudinal (right) direction with respect to the beam. The distributions are fitted with a Student's t-function for which sigma is shown on the plot [?].

The strip detector occupies the radial region between 20 cm and 1.16 m. As illustrated in Fig. ??, it is composed of four subsystems: the four-layer Tracker Inner Barrel (TIB), the six-layer tracker outer barrel (TOB) and on each side three-disk Tracker Inner Disks (TID) and nine-disk Tracker Endcaps (TEC). The silicon micro-strip sensors have strips parallel to the beam axis in the barrel and radial on the disks. The modules in the first two layers and rings, respectively, of TIB, TID, and TOB as well as rings 1, 2, and 5 of the TECs carry a second micro-strip detector module which is mounted back-to-back with a stereo angle of 100 mrad in order to provide a measurement of the second co-ordinate (z in the barrel and r on the disks). This tracker layout ensures at least 9 hits in the silicon strip tracker in the full range of $|\eta| < 2.4$ with at least 4 of them being two-dimensional measurements. The total

number of silicon sensors in the strip tracker is 24244, making up a total active area of 198 m², with about 9.3 million of strips.

3.2.2 Calorimetry

The calorimeter measures the energies and directions of all neutral and charged particles traversing the detector, with the exception of muons and neutrinos. It consists of two parts, the electromagnetic calorimeter (ECAL) [?] and the hadronic calorimeter (HCAL) [?].

The goal of ECAL is to measure precisely the energy of electrons and photons which generate electromagnetic showers inside it. It is a hermetic and homogeneous calorimeter with a large pseudorapidity coverage up to $|\eta| < 3$. As illustrated in Fig. ??, ECAL is divided into barrel and endcap detectors consisting of scintillation crystals made from lead tungstate (PbWO₄). The choice of this material is motivated by its high density (8.28 g/cm³), short radiation length ($X_0 = 0.89$ cm) and small Molière radius (2.2 cm), resulting in a high stopping power, fine granularity and therefore a compact calorimeter able to fit inside the solenoid. The ECAL comprises 61200 crystals in the barrel and 7324 crystals in each of the 2 endcaps, for a total volume of 8.14 m³ and 2.9 m³, respectively. The crystals have a tapered shape and are mounted in a quasi-projective geometry. The barrel extends radially between 1.29 and 1.75 cm covering the region $|z| < 3.05$ m and $|\eta| < 1.479$. The crystals have a front face cross-section of 22×22 mm² and a length of 2.3 cm (25.8 X_0). They are organised in 36 identical supermodules each covering 20° in ϕ . The crystals are contained in a thin-walled glass-fibre alveola structures (?submodules?) with 2(ϕ)×5(η) crystals per each resulting in a granularity 360-fold in ϕ and 2×85-fold in η . The endcaps are placed at a distance of 3.14 m from the interaction point and they extend radially between 3.16 and 17.11 cm, covering the region 1.479 < $|\eta| < 3.0$. The crystals have a front face cross section of 28.6×28.6 mm² and a length of 2.2 cm (24.7 X_0). A preshower detector with a thickness of 3 X_0 is placed in front of the endcaps (1.653 < $|\eta| < 2.6$) to guarantee a reliable discrimination of single photons and photons produced in pairs in neutral pion decays. The relatively low light yield of the crystals (30 γ /MeV) requires use of photodetectors with intrinsic gain that can operate in a magnetic field. Silicon avalanche photodiodes (APDs) are used as photodetectors in the barrel and vacuum phototriodes (VPTs) in the endcaps. The light output and the amplification have a strong temperature dependence. The response to an incident electron changes by (3.8±0.4)%/°C which in turn means that the temperature has to be closely monitored and kept stable to a precision of ±0.05°C. The nominal operating temperature of the ECAL is 18°C and is provided by a water cooling system.

The energy resolution of the electromagnetic calorimeter can be parametrized by the following expression:

$$\frac{\sigma_E}{E} = \frac{S}{\sqrt{E(\text{GeV})}} \oplus \frac{N}{E(\text{GeV})} \oplus C. \quad (3.4)$$

The first term is stochastic including contributions from the shower containment, the number of photoelectrons and the fluctuations in the gain process. The second contribution corresponds to the noise term, which includes noise in the readout electronics and fluctuations in pile-up. The third term is a constant and dominates the energy resolution for high-energy electron and photon showers, depends on non-uniformity of the longitudinal light collection, energy leakage from the back of the calorimeter, single-channel response uniformity and stability. The value of the three coefficients were determined by a electron test beam measurement in a matrix of 33 crystals to be S = 2.8%, N = 12% and C = 0.3% [?].

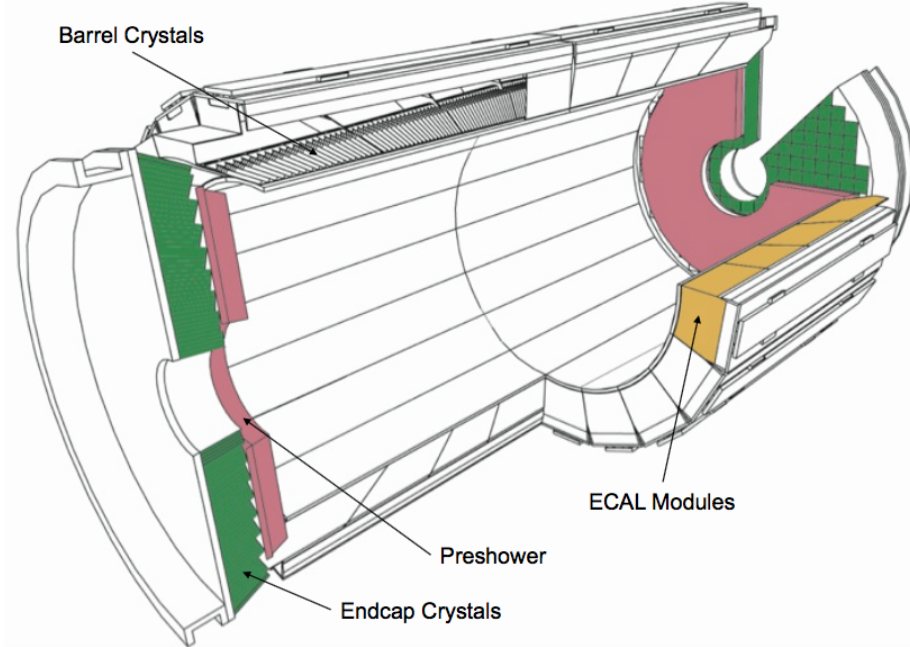


Figure 3.6: Schematic view of the CMS Electromagnetic Calorimeter [?].

The energy measurement of the ECAL is complemented by the measurement of the hadronic calorimeter. The HCAL is designed to be as near to hermetic around the interaction region as possible to allow events with missing energy to be identified. It is a sampling calorimeter composed of layers of brass absorber interlaced with tiles of plastic scintillators as active material to detect the showers generated by the hadrons in the brass. The energy released in the scintillator tiles causes them to emit blue-violet light, a fraction of which is absorbed and re-emitted by embedded wavelength-shifting fibres in the green region of the spectrum. The green light is then carried by special fibre-optic waveguides to the readout system. The photodetection readout is based on multi-channel hybrid photodiodes (HPDs), photodetectors configured especially for CMS that can provide gain and operate in a high magnetic field. Figure ?? shows a schematic cross section of the HCAL detectors. The hadron barrel (HB) and endcaps (HE) calorimeters sit behind the tracker and the electromagnetic calorimeter as seen from the interaction point. The HB is radially restricted between the outer extent of the electromagnetic calorimeter ($r = 1.77$ m) and the inner extent of the magnet coil ($r = 2.95$ m). This constrains the total amount of material which can be put in to absorb the hadronic shower. Therefore, an Outer Hadron (HO) calorimeter is placed outside the solenoid complementing the barrel calorimeter. The HO uses the solenoid as additional absorbing material and provides sufficient containment for hadronic showers with a thickness of 11.8 interaction lengths (λ_l). The first scintillators are placed in front of the first absorber plate in order to sample showers developing in the material between the ECAL and the HCAL, while the last scintillators are installed after the last absorber plate to correct for late developing showers leaking out. 70000 and 20916 scintillator tiles are installed in the HB and the HE, respectively. The HB and HE cover the region $|\eta| < 1.3$ and $1.3 < |\eta| < 3.0$, respectively. Beyond $|\eta| = 3$, the Hadron Forward (HF) calorimeter placed at 11.2 m from the interaction point extends the pseudorapidity coverage down to $|\eta| = 5.2$. The barrel depth goes from $5.46 \lambda_l$ at $\eta = 0$ to 10.8 at $\eta = 1.3$, while the endcaps coincide with an

average of $11 \lambda_l$. The calorimeter is segmented and arranged in towers as summarized in Table ???. The HF is positioned at a longitudinal distance of 11.2 m from the interaction point. It will experience unprecedented particle fluxes with an energy of 760 GeV deposited on average in a proton-proton interaction at $\text{ps} = 14 \text{ TeV}$. This energy has to be compared to the average of 100 GeV deposited in the rest of the detector. The situation is even more severe as the energy is not spread equally among the HF, but has a pronounced peak at the highest rapidity. The HF is a sampling calorimeter made from steel absorber plates composed of 5mm thick grooved plates with quartz fibers inserted as active medium. The signal is generated when charged shower particles above the threshold generate Cherenkov light in the quartz fibres, thereby rendering the calorimeter mostly sensitive to the electromagnetic component of showers.

The HCAL energy resolution is

$$\frac{\sigma_E}{E} = \frac{a}{\sqrt{E(\text{GeV})}} \oplus 5\% \quad (3.5)$$

where a is 65% in the barrel, 85% in the endcaps and 100% in the forward calorimeter.

Table 3.1: Tower segmentation in azimuthal and polar angle for the hadronic barrel, endcap and forward calorimeter.

	HB/HO	HE ($ \eta \leq 2.5$)	HE ($ \eta > 2.5$)	HF ($ \eta \leq 4.7$)	HF ($ \eta > 4.7$)
$\Delta\phi \times \Delta\eta$	0.087×0.087	0.087×0.087	0.175×0.175	0.175×0.175	0.175×0.35

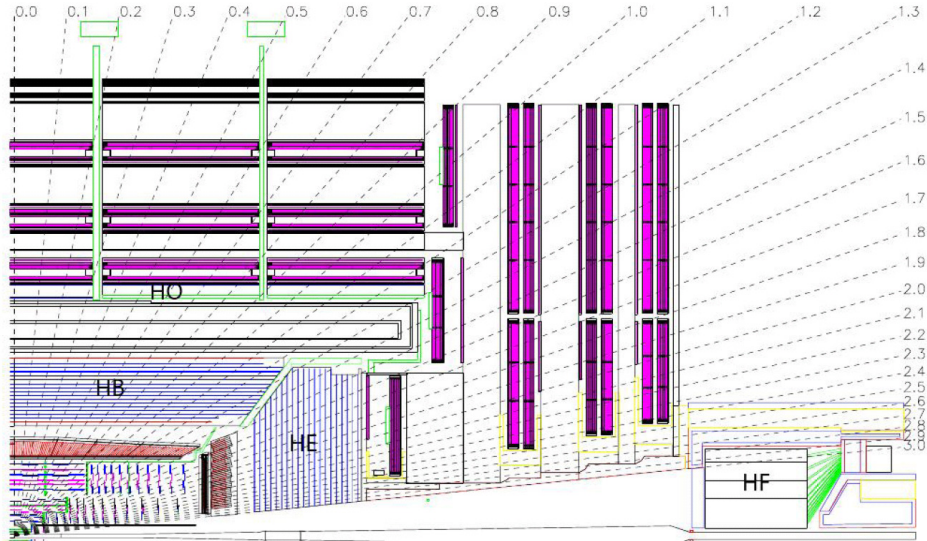


Figure 3.7: Longitudinal view of the CMS detector showing the locations of the hadron barrel (HB), endcap (HE), outer (HO) and forward (HF) calorimeters [?].

3.2.3 Muon detectors

The muon system is the outermost part of the CMS detector. It is located in the steel return yoke of the solenoid, covering the pseudorapidity region $|\eta| < 2.4$. This is possible because muons are hardly affected by this large material budget. The coil acts as a shield from electromagnetic and hadronic particles escaping the calorimeters and the yoke provides

a magnetic field between consecutive muon stations, allowing a momentum measurement independent from the inner tracker. The muon system is designed for three major functions: robust and fast identification of muons, good resolution of momentum measurement, and integration to a fast and reliable trigger system. The gaseous detectors has been chosen as muon detectors since they are robust and with a relative fast response. Furthermore, the area to be covered is extremely wide and a gaseous detector system allows to reduce the cost and the amount of readout channels. The muon system is thus composed of three types of gaseous detectors arranged in barrel and endcap sections, as shown in Fig. ??: Drift Tubes (DTs), Resistive Plate Chambers (RPCs) and Cathode Strip Chambers (CSCs). The choice of different detector topologies lies essentially in the different expected particle rates.

In the barrel region, where the neutron-induced background is small, the muon rate is low, and the 4-T magnetic field is uniform, DTs with standard rectangular drift cells are used covering the pseudorapidity region $|\eta| < 1.2$. A DT cell is a 4 cm wide gas tube with a positively charged stretched wire inside. The barrel DT chambers are organized in five separate wheels. Each wheel is divided into 12 sectors, each covering a 30° azimuthal angle. In each of the 12 sectors there are 4 chambers per wheel which are concentric around the beam line and separated by the iron return yoke. Each DT chamber, on average $2\text{ m} \times 2.5\text{ m}$ in size, consists of 12 layers of DT cells, arranged in three groups of four. For the first 3 stations in each wheel, the middle group measures the z coordinate while the two outside groups measure the $r\phi$ coordinate. The fourth and outermost station does not contain the z -measuring planes. Each one of the 250 DT chambers has a resolution of $\sim 100\text{ }\mu\text{m}$ in $r\phi$ and up to $150\text{ }\mu\text{m}$ in z , and can measure the particle direction with 1 mrad accuracy.

In the two endcap regions of CMS, where the muon rates and background levels are high and the magnetic field is large and non-uniform, CSCs are used with their fast response time, fine segmentation, and radiation resistance, covering the pseudorapidity region between 0.9 and 2.4. Each CSC is trapezoidal shaped multiwire proportional chambers which consists of 6 gas gaps, each gap having a plane of radial cathode strips and a plane of anode wires running almost perpendicularly to the strips. The gas ionization and subsequent electron avalanche caused by a charged particle traversing each plane of a chamber produces a charge on the anode wire and an image charge on a group of cathode strips. Thus, each CSC provides a two-dimensional position measurement, where the r and ϕ coordinates are determined by the cathode strips and the anode wires, respectively. 540 CSC are arranged in 4 disks per endcaps divided in concentric rings (3 rings in the innermost station, 2 in the others). Each chamber has a spatial resolution of about 200 mm in r , and $75 \times 150\text{ }\mu\text{m}$ in the $r\phi$ coordinate.

In addition, there is a total of 610 RPCs added in both the barrel and endcap regions to provide a fast, independent, and highly-segmented trigger over a large portion of the rapidity range ($|\eta| < 1.6$) of the muon system. They produce a fast response, with good time resolution ($\sim 2\text{ ns}$) but coarser position resolution than the DTs or CSCs. RPCs are made from two high resistive plastic plates with a voltage applied and separated by a gas volume. The signal generated by the muon when passing through the gas volume is detected by readout strips mounted on top of one of the plastic plates. Six layers of RPCs are installed in the barrel muon system, two layers in each of the first two stations and one layer in each of the last two stations. One layer of RPCs is built into each of the first three stations of the endcap.

3.2.4 The trigger system

The LHC provides proton-proton and heavy-ion collisions at unprecedented high luminosity and interaction rates. Given the high segmentation of the CMS detector, about 100 million readout channels are present and this corresponds to an enormous volume of data at the

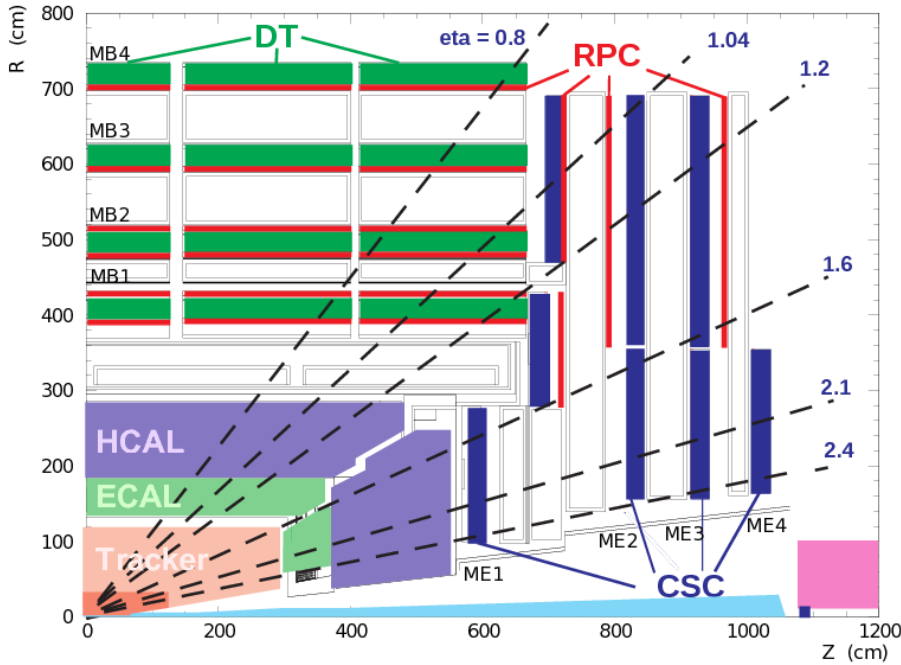


Figure 3.8: A longitudinal view of one quarter of the CMS experiment; the three muon detectors detector types are highlighted.

detector front-ends. At the design luminosity and collision frequency, each crossing produces approximately 1 MB of zero-suppressed data resulting in a raw data rate of about 40 TB per second. These figures are many orders of magnitude larger than the archival storage capability of ~ 1 kHz at data rates of $\mathcal{O}(10^2)$ MB/s. Technical difficulties in handling, storing and processing such extremely large amounts of data impose a reduction factor on the rate of events that can be written to permanent storage. This task is performed by the trigger system, which is the baseline of the physics event selection process. The key point of the trigger system is a fast time rejection of all the “non-interesting” events. This can be done by exploiting event topologies common to group of physics processes, such as the presence of one or more leptons in the event. The trigger system needs to be as inclusive as possible, in order to collect data for all the physics searches that can be performed looking at pp collision, but it has also to operate within the CMS time restriction and to not saturate the storage capability. The required rejection power of $\mathcal{O}(\times 10^5)$ is too large to be achieved in a single processing step, if a high efficiency is to be maintained for the physics phenomena CMS plans to study. For this reason, the full selection task is split into two steps. The first step (Level-1 Trigger) is designed to reduce the rate of events accepted for further processing to less than 100 kHz. The second step (High-Level Trigger or “HLT”) is designed to reduce this maximum L1 accept rate of 100 kHz to a final output rate of 1 kHz.

The L1 Trigger is built from custom designed, programmable electronics and is housed partly on the detectors, partly in the underground control room located at a distance of approximately 90 m from the experimental cavern. It is designed to take a fast accept/reject decision every bunch crossing, on the basis of a rough reconstruction of the event. The detector information used at L1 are coarsely segmented data from the calorimeters and the muon system only. Within a time budget of $3.2 \mu\text{s}$, it has to decide if an event is discarded or kept, and transfer this decision back to the sub-detectors, which in the meantime keep the high resolution data in the front-end electronics. Figure ?? shows the L1 Trigger architecture:

it has local, regional and global trigger components.

Trigger primitives are generated by calculating the transverse energy of a trigger tower and assigning it to the correct bunch crossing. A regional calorimeter trigger then determines regional electron, photon and jet candidates and information relevant for muon and tau identification. The global calorimeter trigger provides information about the jets, the total transverse energy and the missing energy in the event and identifies the highest-ranking trigger candidates.

In the muon system all three types of detectors take part in the trigger decision. The DT chambers provide track segments in the projection and hit pattern in η , while the CSC determine three-dimensional track segments. The track finders in the DT chambers and the CSCs calculate the transverse momentum of a track segment and its location and quality. The RPCs deliver an independent measurement derived from regional hit patterns. The global muon trigger receives up to four candidates from each subsystem (DT, barrel RPC, CSC and endcap RPC) together with the isolation information from the global calorimeter trigger. The aim is to improve the efficiency and to reduce the rate by making use of the complementarity and the redundancy of the subsystems. In the end, the global muon trigger selects a maximum of four muon trigger candidates and determines their momentum, charge, position and quality.

The trigger objects extracted by the global calorimeter trigger and the global muon trigger are sent to the global trigger where the decision to accept or reject an event is taken and distributed to the sub-detectors. The simplest triggers are in general those based on the presence of one object with an E_T or p_T above a predefined threshold (single-object triggers) and those based on the presence of two objects of the same type (di-object triggers) with either symmetric or asymmetric thresholds. Other requirements are those for multiple objects of the same or different types (“mixed” and multiple-object triggers). Up to 128 algorithms can be executed in parallel. The decision is also based on the readiness of the sub-detectors and the data acquisition system (DAQ), which is supervised by the Trigger Control System (TCS). The Level-1 Accept (L1A) decision is communicated to the sub-detectors through the Timing, Trigger and Control (TTC) system.

If an event is accepted by the L1 trigger, the full detector information (1 MB) is read out by the DAQ system and passed to the HLT system for further analysis. The HLT is a special part of the CMS software which runs on a farm of several thousand processors performing high-level object reconstruction and analysis. Each processor works on the reconstruction of one event at a time, to get to a trigger decision within on average 100 ms. Since the time budget for one event is much larger than at the L1 trigger, more complicated algorithms, including tracking, can be executed at the HLT. Once an event is accepted, it is stored on disk and fully reconstructed offline at a later time.

The full detector readout is available at HLT, but in order to meet the timing requirements given by the input rate from L1, events are discarded before being fully reconstructed, as soon there is enough reconstructed information to take the decision. Therefore the selection is organized in a sequence of logical steps. The Level-2 uses the full information from calorimeters and muon detectors to reconstruct the physical objects and to reduce the event rate by roughly one order of magnitude. The data from the silicon tracker represent almost 80% of the event size and require complex and time consuming algorithms for the reconstruction. For this reason this information is used only during the Level-3 selection.

The HLT consists of approximately 400 trigger paths. Each trigger path starts from the seed provided by the L1 trigger and it is built from reconstruction modules and filter modules. After some parts of the data are reconstructed, a filter module decides if the reconstructed objects pass the thresholds and the next step in reconstruction is started, or if the event is

not accepted by the path. In the later case, the execution of the path is stopped and the following reconstruction steps and filter steps are not performed to save computation time. If an event is not accepted by a path, it can still be accepted by a different path.

If, for some paths with low thresholds, the acceptance rate is too high, they can be prescaled to lower the rate. A prescale value of ten means, for example, that the path is executed only for every tenth event that was accepted by the L1 trigger, and, consequently, the trigger rate for that path is ten times smaller. The prescale value for one trigger path has several predefined levels, depending on the instantaneous luminosity of the LHC machine. During an LHC fill, the instantaneous luminosity decreases, and the prescale values can be changed during a CMS run to keep the global trigger rate at an optimal level.

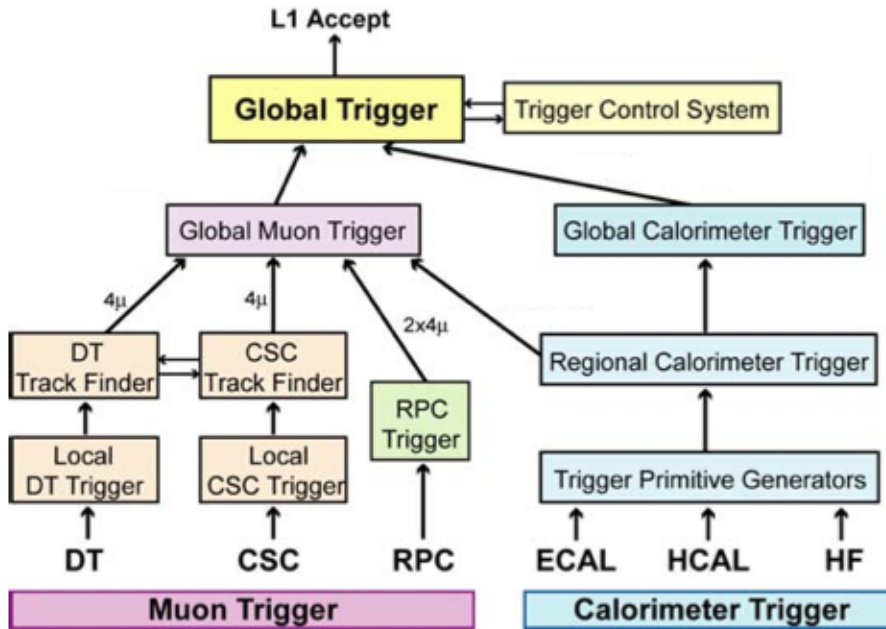


Figure 3.9: Architecture of the Level-1 Trigger [?].

Part I

Search for diboson resonances with CMS

CHAPTER 4

Diboson resonances as signature for new physics

Event simulation

5.1 Monte Carlo event generators

5.2 Simulation of physics processes

5.2.1 Simulation of signal processes

5.2.2 Simulation of background processes

Object and event reconstruction

6.1 Tracks and vertices

6.2 Electrons

6.3 Muons

6.4 Jets

6.4.1 Identification of b jets

6.5 Missing transverse energy

6.6 $W \rightarrow \ell\nu$ reconstruction

Boosted H \rightarrow b \bar{b} and W/Z \rightarrow q \bar{q} $(')$ identification with jet substructure

7.1 Jet substructure algorithms

7.1.1 Jet pruning

7.1.2 N-subjettiness

7.2 W/Z-tagging validation in top enriched sample

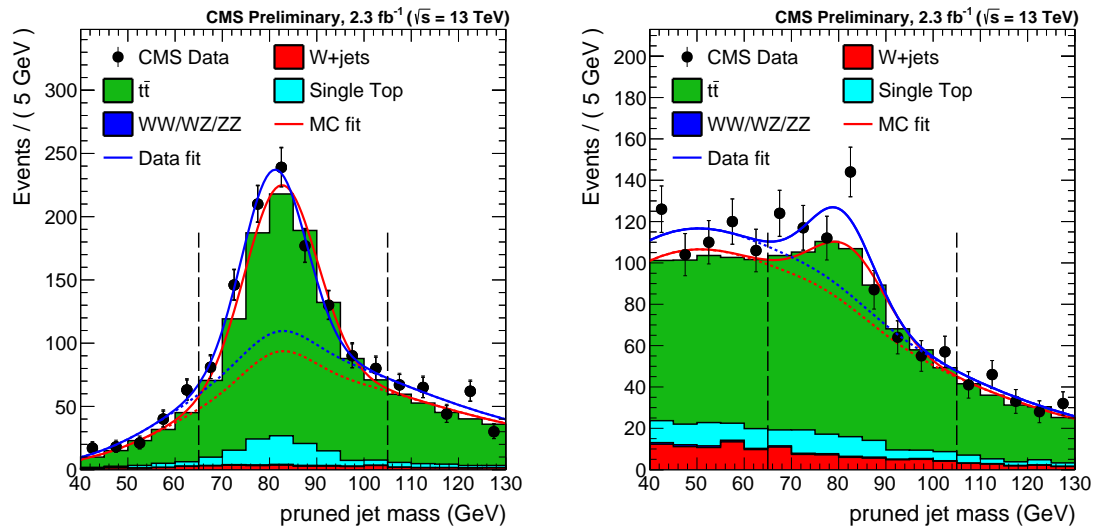


Figure 7.1: W-tagging at 13 TeV. **FIXME:** cite PAS when public

7.3 H-tagging algorithm

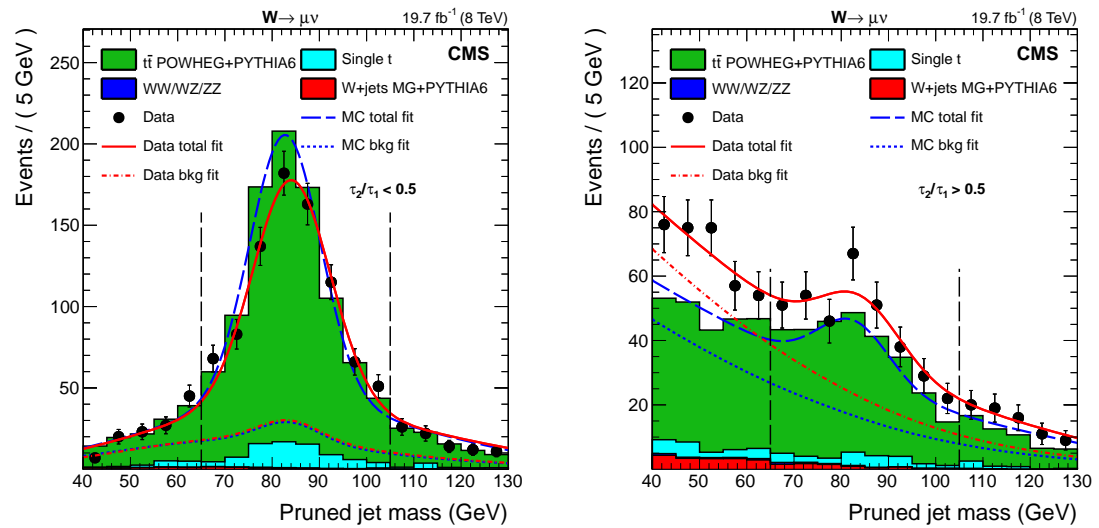


Figure 7.2: W-tagging at 8 TeV (mu) [?].

Final event selection and categorization

- 8.1 Search for a WH resonance in the $\ell\nu b\bar{b}$ final state at $\sqrt{s} = 8$ TeV
 - 8.1.1 $t\bar{t}$ background rejection
 - 8.1.2 Final selection and control plots
- 8.2 Search for WW/WZ resonances in the $\ell\nu q\bar{q}^{(\prime)}$ final state at $\sqrt{s} = 13$ TeV
 - 8.2.1 W/Z-jet mass categories
 - 8.2.2 Final selection and control plots

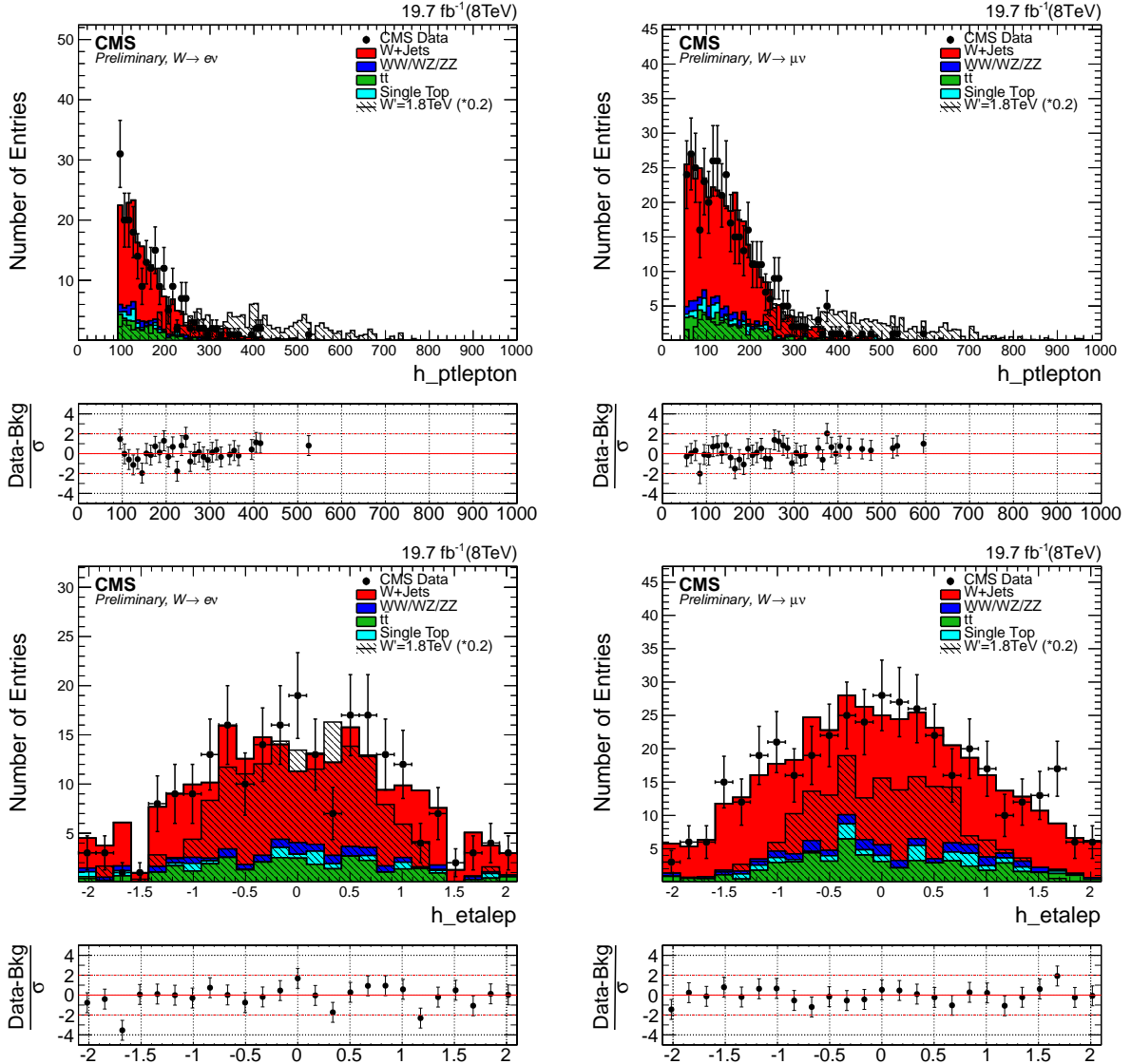


Figure 8.1: Lepton p_T and η for electron channel (left) and muon channel (right) for events with $40 < m_{jet}^{pruned} < 110$ GeV. The signal is normalized to 0.1 times of the selected events for the model considered (W' , $M = 1$ TeV).

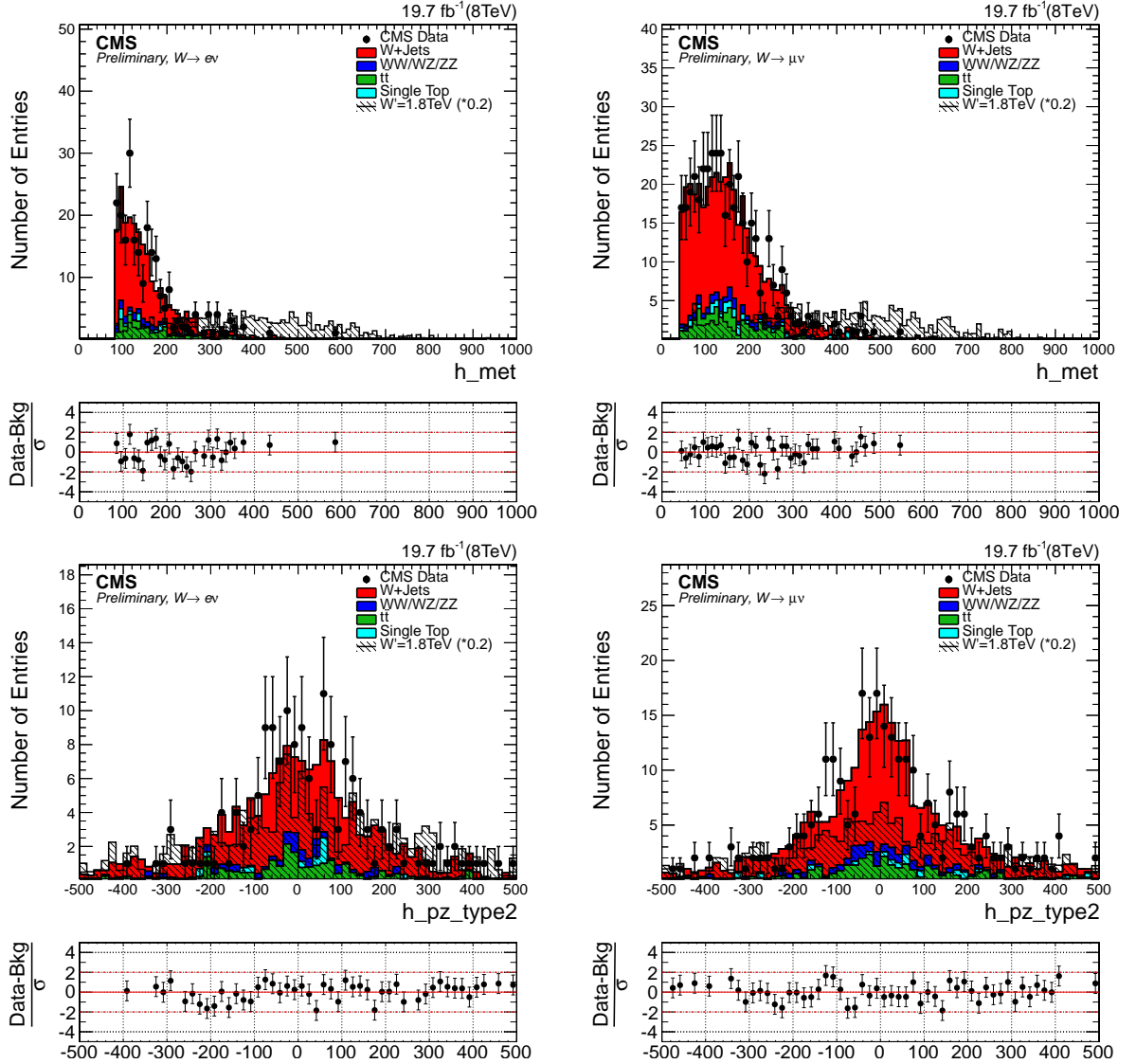


Figure 8.2: E_T^{miss} and $p_{z\nu}$ (defined in Section) for electron channel (left) and muon channel (right) for events with $40 < m_{jet}^{\text{pruned}} < 110$ GeV. The signal is normalized to 0.1 times of the selected events for the model considered (W' , $M = 1$ TeV).

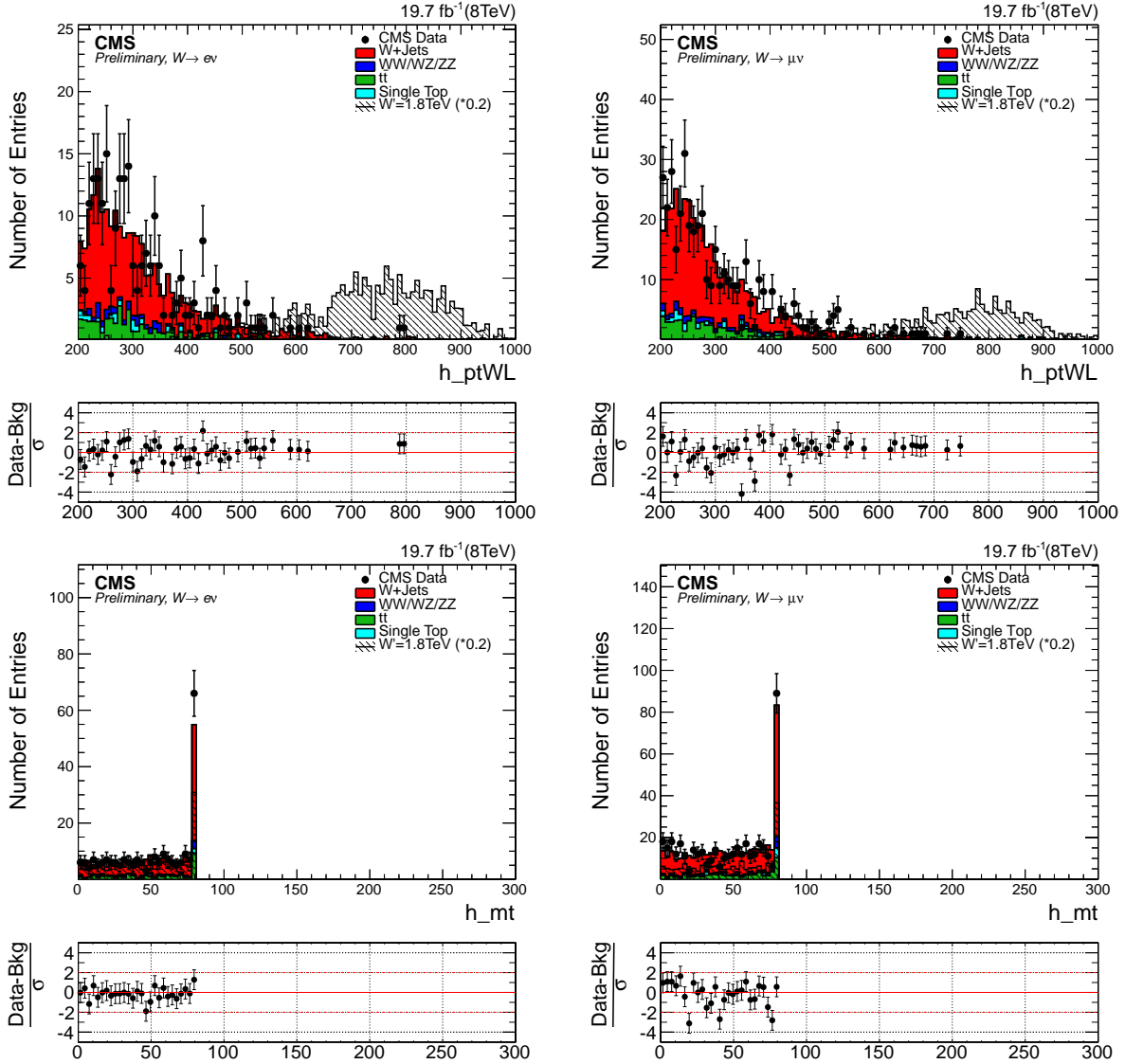


Figure 8.3: Leptonic W p_T and M_T for electron channel (left) and muon channel (right) for events with $40 < m_{\text{jet}}^{\text{pruned}} < 110$ GeV. The signal is normalized to 0.1 times of the selected events for the model considered (W' , $M = 1$ TeV).

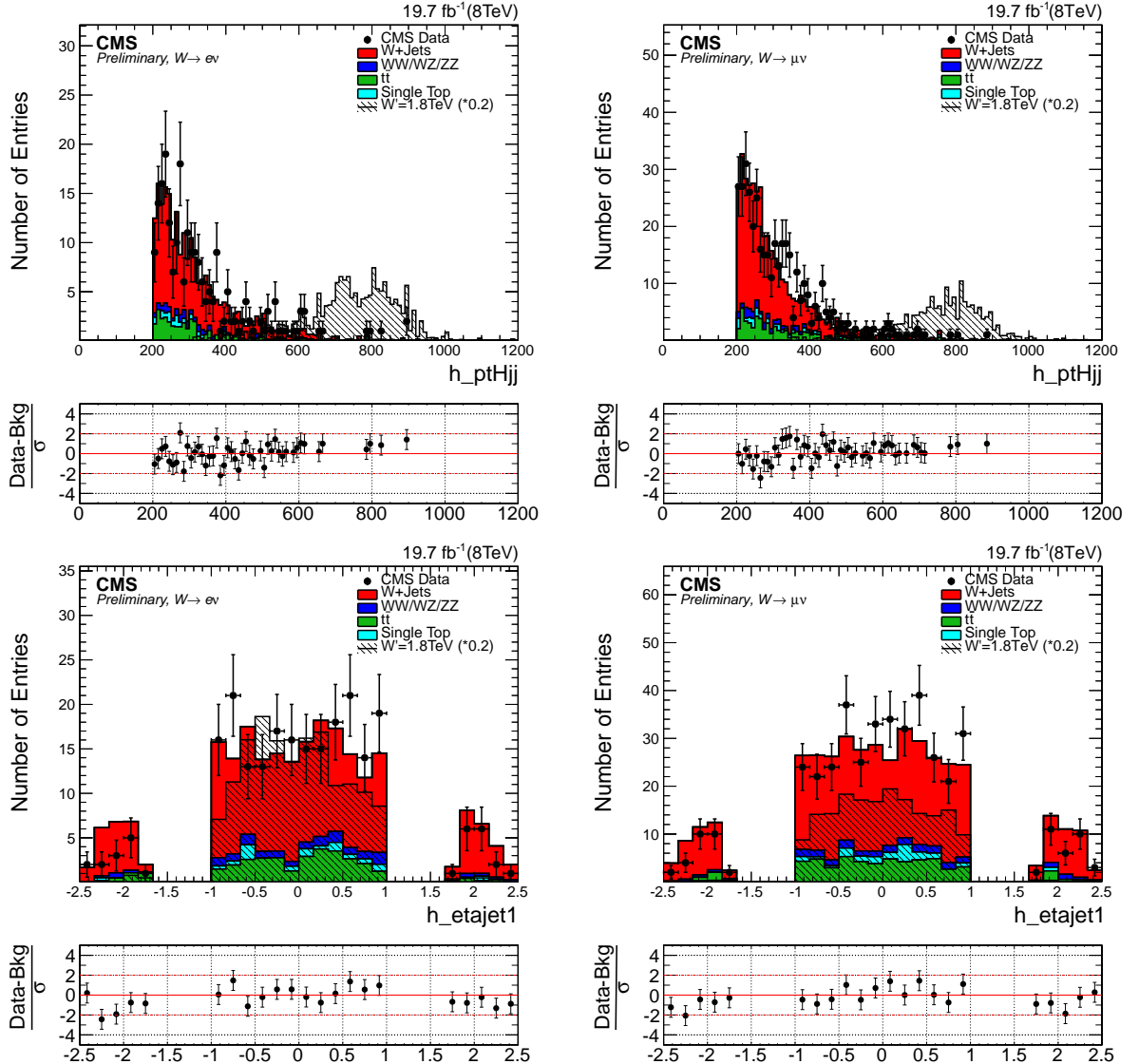


Figure 8.4: Hadronic W p_T and η for electron channel (left) and muon channel (right) for events with $40 < m_{jet}^{pruned} < 110$ GeV. The signal is normalized to 0.1 times of the selected events for the model considered (W' , $M = 1$ TeV).

Table 8.1: Summary of final selection.

Selection	Value	Comments
Tight Lepton selection		
Electron p_T	$p_T > 90 \text{ GeV}$	
Muon p_T	$p_T > 50 \text{ GeV}$	
Electron η	$ \eta _{\text{SC}} < 2.5$ except $[1.4442, 1.566]$ range	Avoid the ECAL gap.
Muon η	$ \eta < 2.1$	
Loose Lepton selection		
Electron p_T	$p_T > 35 \text{ GeV}$	
Muon p_T	$p_T > 20 \text{ GeV}$	
Electron η	$ \eta _{\text{SC}} < 2.5$ except $[1.4442, 1.566]$ range	Avoid the ECAL gap.
Muon η	$ \eta < 2.4$	
CA8 jet selections		
Jet p_T	$p_T > 80 \text{ GeV}$	Used for hadronic H reconstruction
Jet η	$ \eta < 2.4$ except $[1, 1.5]$ range	
AK5 jet selections		
Jet p_T	$p_T > 30 \text{ GeV}$	Used for b-veto jet selection
Jet η	$ \eta < 2.4$	
E_T^{miss} selections		
E_T^{miss} (electron ch.)	$E_T^{\text{miss}} > 80 \text{ GeV}$	
E_T^{miss} (muon ch.)	$E_T^{\text{miss}} > 40 \text{ GeV}$	
Boson selections		
Pruned jet mass (signal)	$110 < m_{\text{jet}}^{\text{pruned}} < 135 \text{ GeV}$	
Pruned jet mass (low-mass sideband)	$40 < m_{\text{jet}}^{\text{pruned}} < 110 \text{ GeV}$	
Pruned jet mass (high-mass sideband)	$135 < m_{\text{jet}}^{\text{pruned}} < 150 \text{ GeV}$	
Leptonic W p_T	$p_T > 200 \text{ GeV}$	
Hadronic H p_T	$p_T > 200 \text{ GeV}$	
Back-to-back topology	$\Delta R(\ell, H_{\text{had}}) > \pi/2$, $\Delta\phi(H_{\text{had}}, E_T^{\text{miss}}) > 2$ $\Delta\phi(H_{\text{had}}, W_{\text{lep}}) > 2$	
B-tag veto	no CSV Medium AK5 jet within $\Delta R(\text{ca8}, \text{ak5}) = 0.8$	
Combined b-tagging cut	$>= 2$ CSVL subjets if $\Delta R > 0.3$ of subjets $>= 1$ CSVL CA8 jet if $\Delta R < 0.3$ of subjets	
Top mass veto	$m_{\text{top}}^{\text{leptonic}} < 120 \parallel m_{\text{top}}^{\text{leptonic}} > 240$ $m_{\text{top}}^{\text{hadronic}} < 160 \parallel m_{\text{top}}^{\text{hadronic}} > 280$	
Veto		
Number of loose electrons	0	in addition to tight lepton
Number of loose muons	0	in addition to tight lepton

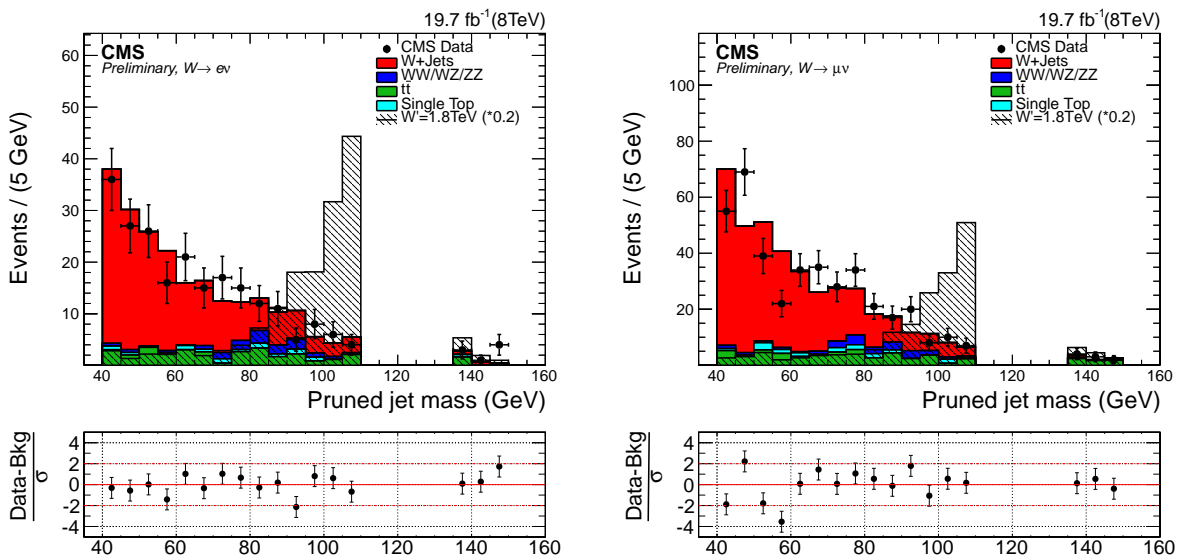


Figure 8.5: m_{jet}^{pruned} for electron channel (left) and muon channel (right) for events with $40 < m_{jet}^{pruned} < 110$ GeV. The signal is normalized to 0.1 times of the selected events for the model considered (W' , $M = 1$ TeV).

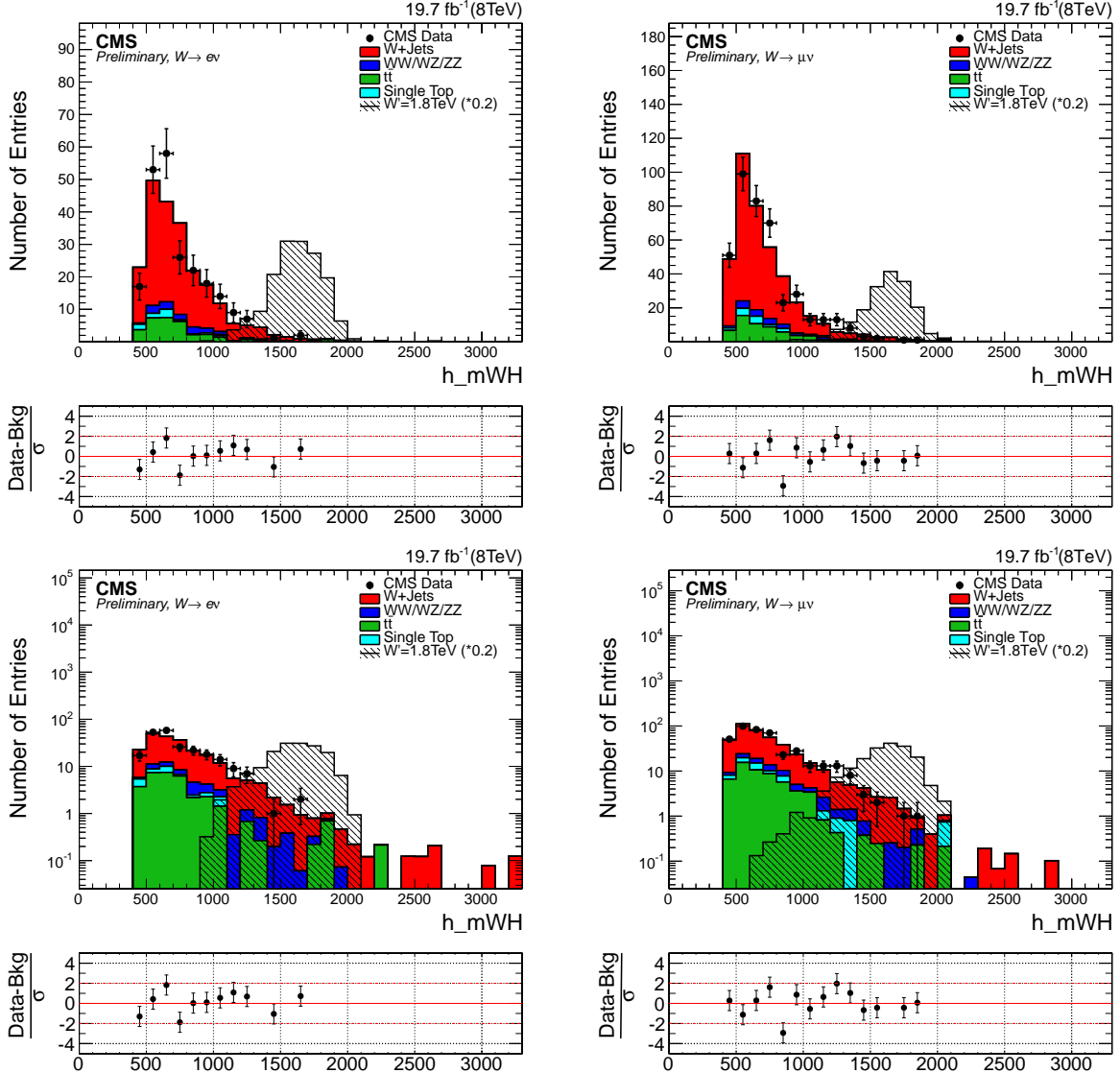


Figure 8.6: m_{WH} (using the $p_{z\nu}$ defined in Section) in linear and log scale for electron channel (left) and muon channel (right) for events with $40 < m_{jet}^{pruned} < 110$ GeV (sideband region). The signal is normalized to 0.1 times of the selected events for the model considered (W' , $M = 1$ TeV).

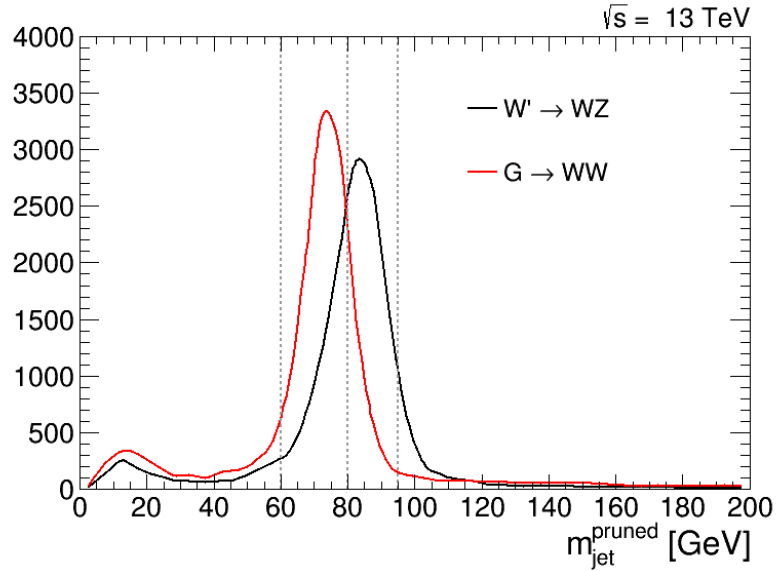


Figure 8.7: Pruned jet mass distributions of merged W-jets and merged Z-jets expected in $G \rightarrow WW \rightarrow l\nu qq$ and $W' \rightarrow WZ \rightarrow l\nu qq$ signals, respectively. The optimal separation point between the two distributions is shown together with the signal region boundaries.

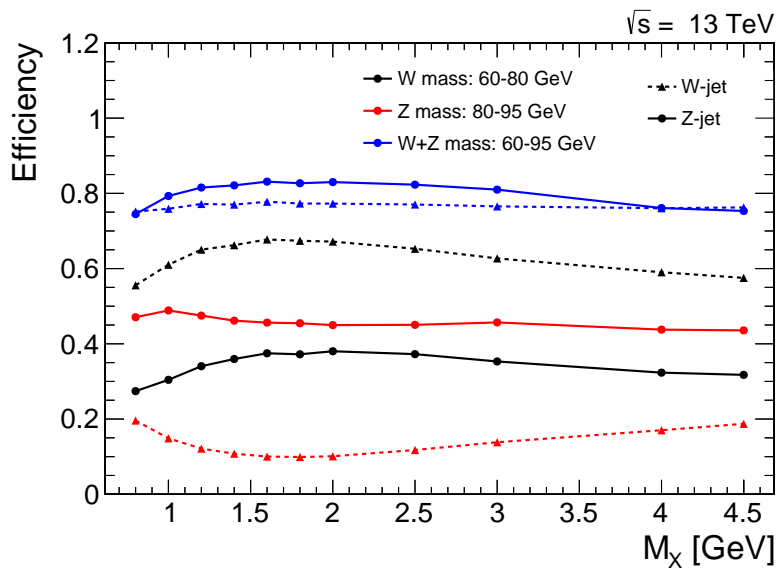


Figure 8.8: Efficiencies of a W-jet signal ($G \rightarrow WW$) (dashed lines) and of a Z-jet signal ($W' \rightarrow WZ$) (solid lines) as a function of the resonance mass for different pruned jet mass windows: W-mass category (black), Z-mass category (red) and default single mass category (blue).

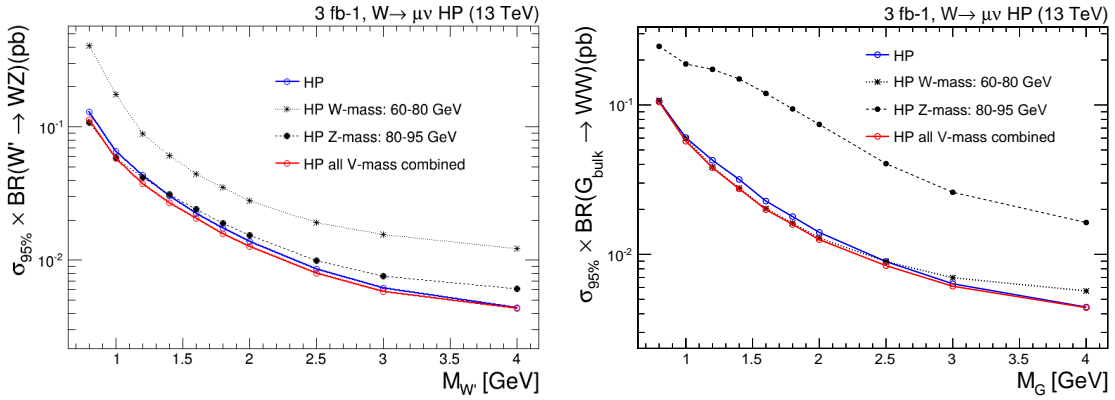


Figure 8.9: Expected 95% CL upper limits on the production cross section of a W' signal multiplied by the branching fraction of $W' \rightarrow WZ$ as function of the resonance mass for the different mass categories for events passing the high-purity τ_{21} selections. Expected 95% CL upper limits on the production cross section of a Graviton signal multiplied by the branching fraction of $G \rightarrow WW$ as function of the resonance mass for the different mass categories for events passing the high-purity τ_{21} selections.

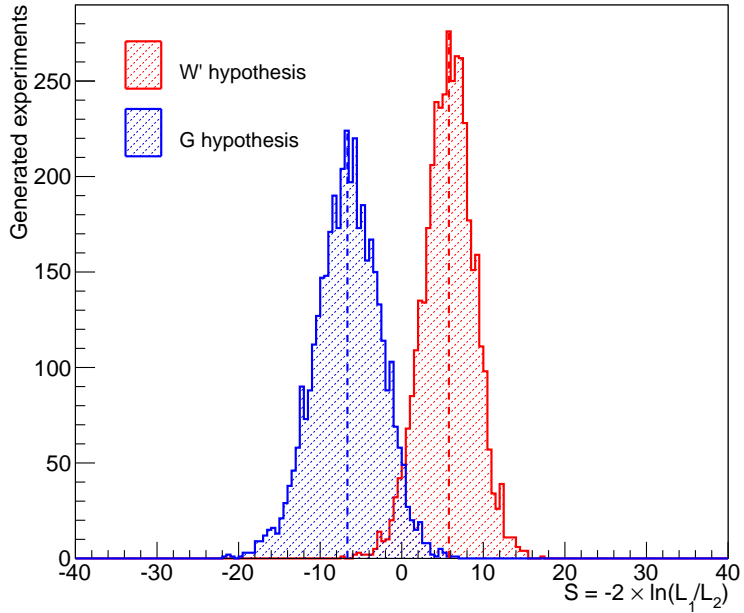


Figure 8.10: Distribution of the test statistic $q = -2 \ln(L_G/L_{W'})$ of the Graviton signal hypothesis (blue) tested against the W' signal hypothesis (red).

Table 8.2: Summary of the VW channel final selection.

Selection	Value	Comments
Tight Lepton selection		
Electron p_T	$p_T > 120$ GeV	
Muon p_T	$p_T > 53$ GeV	
Electron η	$ \eta _{SC} < 2.5$ except [1.4442, 1.566] range	Avoid the ECAL gap.
Muon η	$ \eta < 2.1$	
Loose Lepton selection		
Electron p_T	$p_T > 35$ GeV	
Muon p_T	$p_T > 20$ GeV	
Electron η	$ \eta _{SC} < 2.5$ except [1.4442, 1.566] range	Avoid the ECAL gap.
Muon η	$ \eta < 2.4$	
AK8 jet selections		
Jet p_T	$p_T > 200$ GeV	Used for hadronic W reconstruction
Jet η	$ \eta < 2.4$	
AK4 jet selections		
Jet p_T	$p_T > 30$ GeV	Used for b-tag jet selection
Jet η	$ \eta < 2.4$	
E_T^{miss} selections		
E_T^{miss} (electron ch.)	$E_T^{\text{miss}} > 80$ GeV	
E_T^{miss} (muon ch.)	$E_T^{\text{miss}} > 40$ GeV	
Boson selections		
Pruned jet mass (signal)	$65 < m_{jet}^{\text{pruned}} < 105$ GeV	
Pruned jet mass (low-mass sideband)	$40 < m_{jet}^{\text{pruned}} < 65$ GeV	
Pruned jet mass (high-mass sideband)	$105 < m_{jet}^{\text{pruned}} < 135$ GeV	
Leptonic W p_T	$p_T > 200$ GeV	
Hadronic W p_T	$p_T > 200$ GeV	
Back-to-back topology	$\Delta R(\ell, W_{had}) > \pi/2$, $\Delta\phi(W_{had}, E_T^{\text{miss}}) > 2$ $\Delta\phi(W_{had}, W_{lep}) > 2$	
Veto		
Number of loose electrons	0	in addition to tight lepton
Number of loose muons	0	in addition to tight lepton
Number of b-tagged jets	0	PF iCSV medium working point
Diboson selections		
2- to 1-subjettiness ratio (high purity)	$\tau_{21} < 0.60$	
2- to 1-subjettiness ratio (low purity)	$0.60 \leq \tau_{21} < 0.75$	

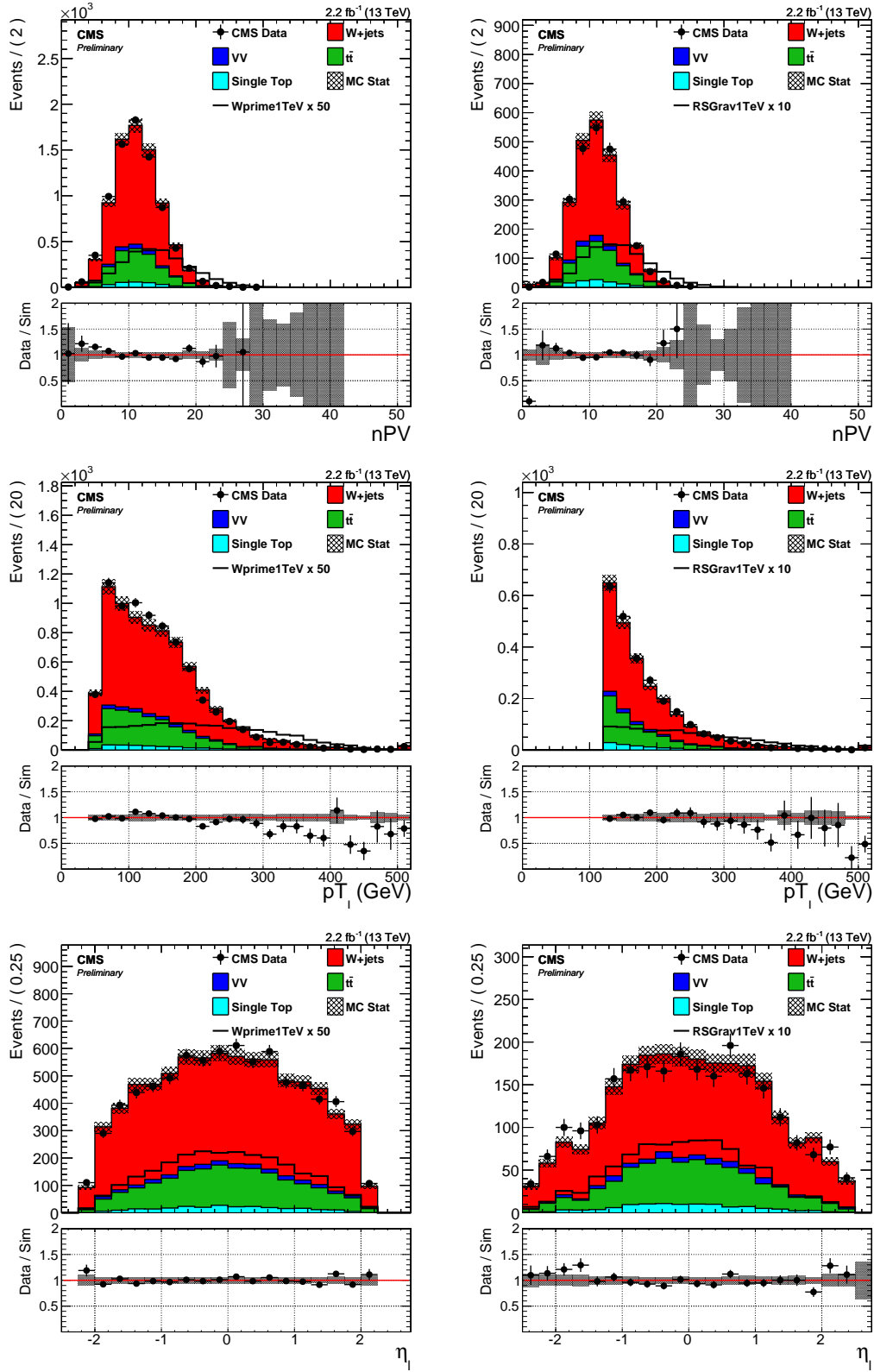


Figure 8.11: Comparison plots between data and MC for different observables, in the jet mass sideband. From top to bottom: number of primary vertices, lepton p_T , lepton η . Left: muon channel, right: electron channel.

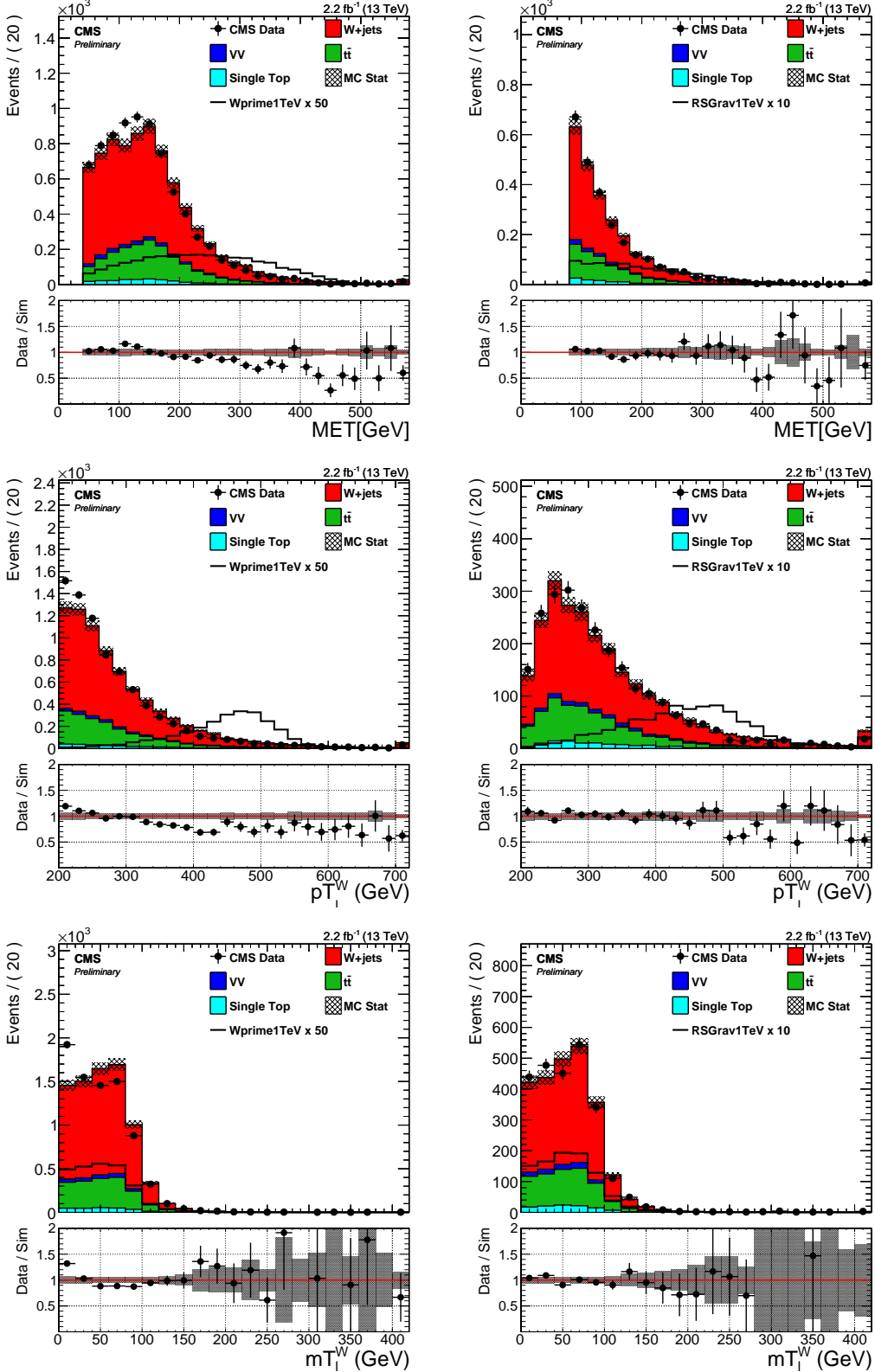


Figure 8.12: Comparison plots between data and MC for different observables, in the jet mass sideband. From top to bottom: E_T^{miss} , leptonic W p_T , transverse mass of the leptonic W. Left: muon channel, right: electron channel.

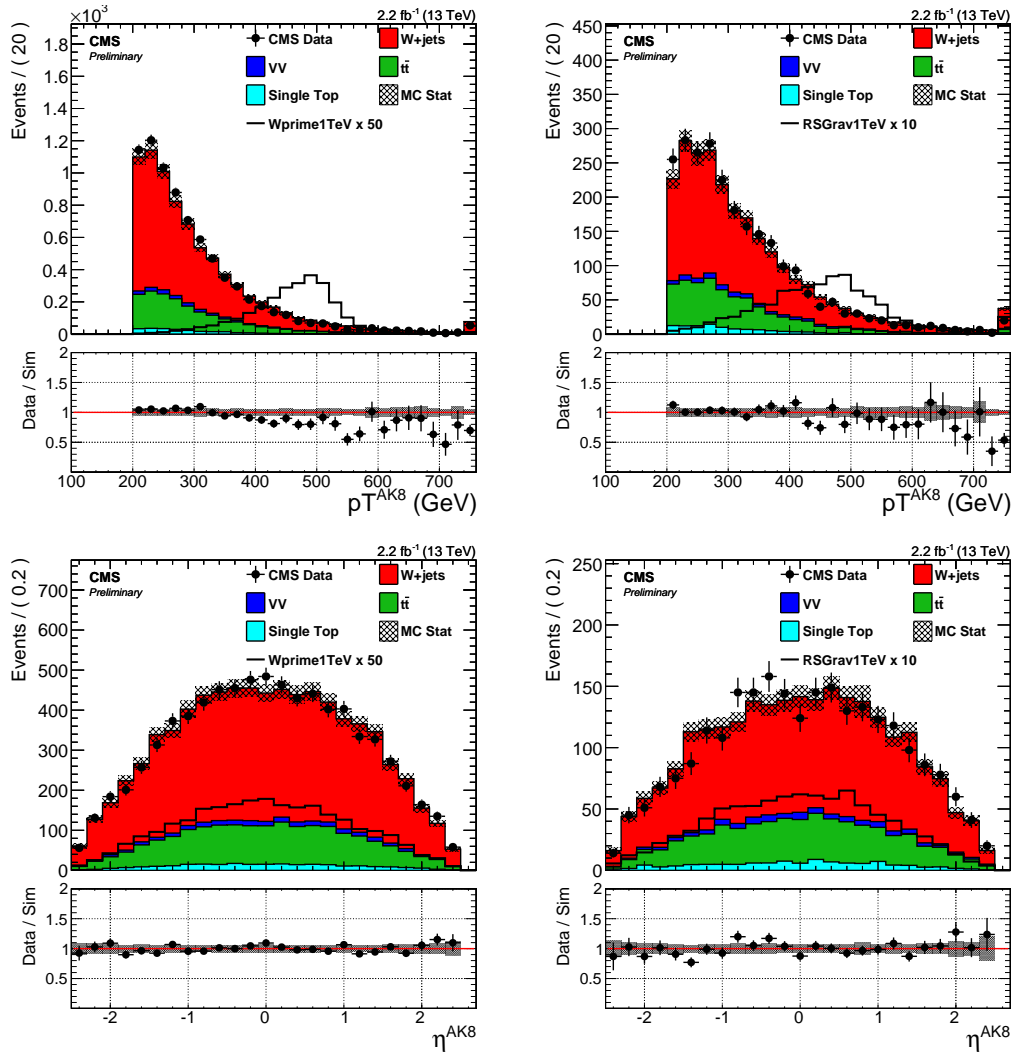


Figure 8.13: Comparison plots between data and MC for different observables, in the jet mass sideband. Top: p_T of the leading AK8 jet. Bottom: η of the leading AK8 jet. Left: muon channel, right: electron channel.

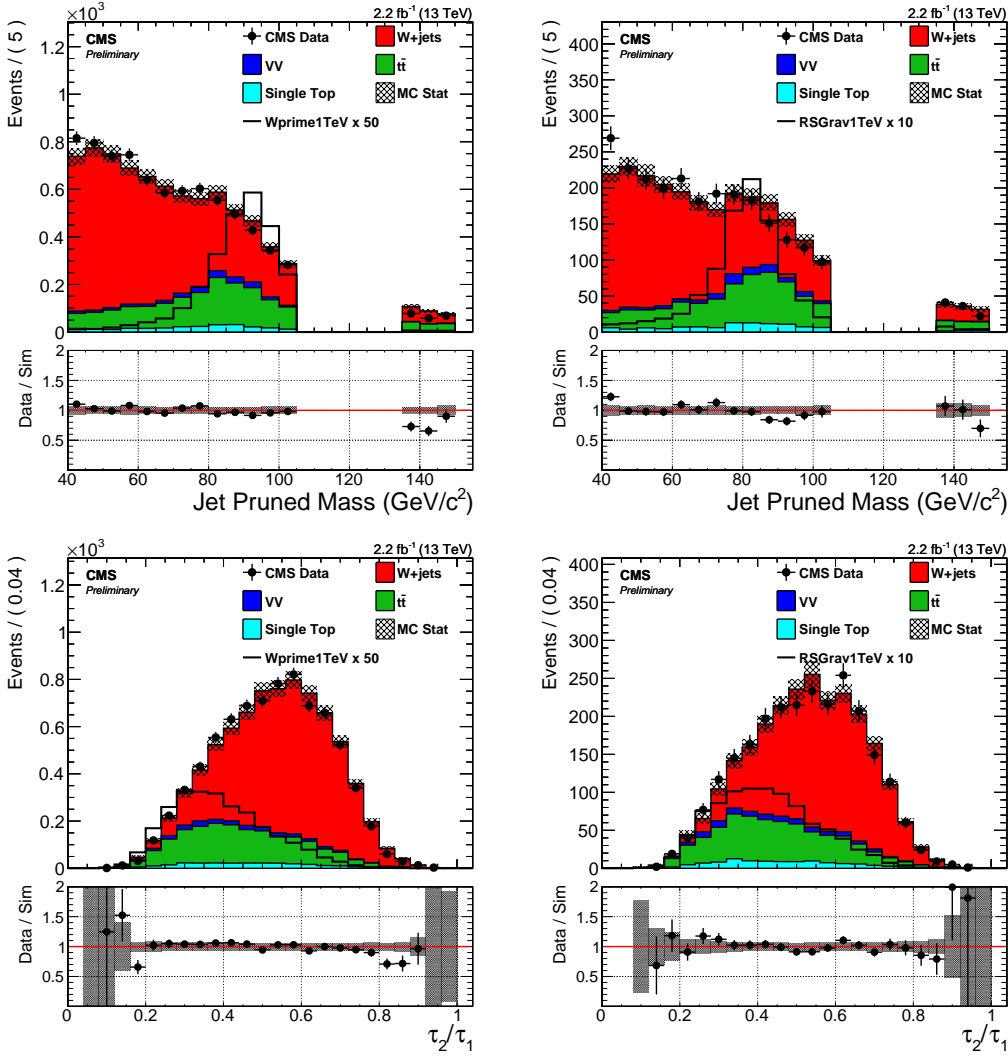


Figure 8.14: Comparison plots between data and MC for different observables, in the jet mass sideband. Top: pruned jet mass. Bottom: N-subjettiness. Left: muon channel, right: electron channel.

Background modeling

9.1 W+jets background estimate with alpha method

9.1.1 Description

9.1.2 Extraction of the W+jets normalization

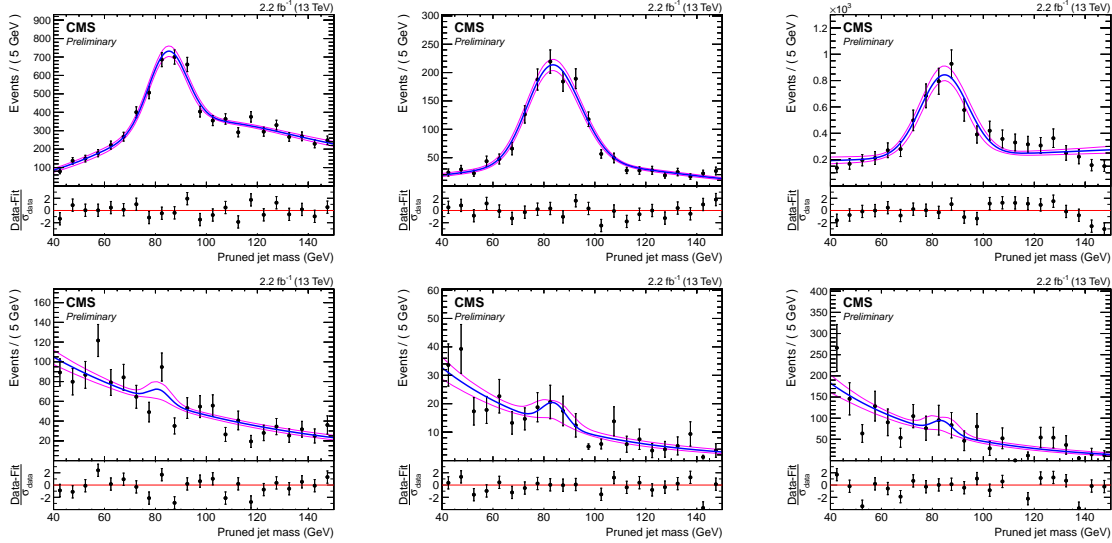


Figure 9.1: MC fits of non-dominant background m_{jet} spectra: on top (bottom) high purity (low purity) categories for the muon channel. Left to right are the $t\bar{t}$, diboson (WW/WZ/ZZ) and Single Top processes.

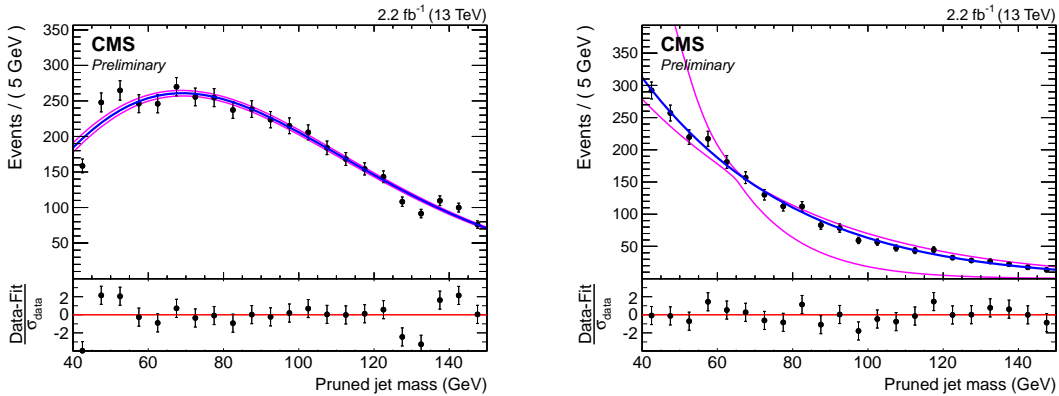


Figure 9.2: MC fits of dominant W+jets background m_{jet} spectra: high purity (left) and low purity (right) category for the muon channel.

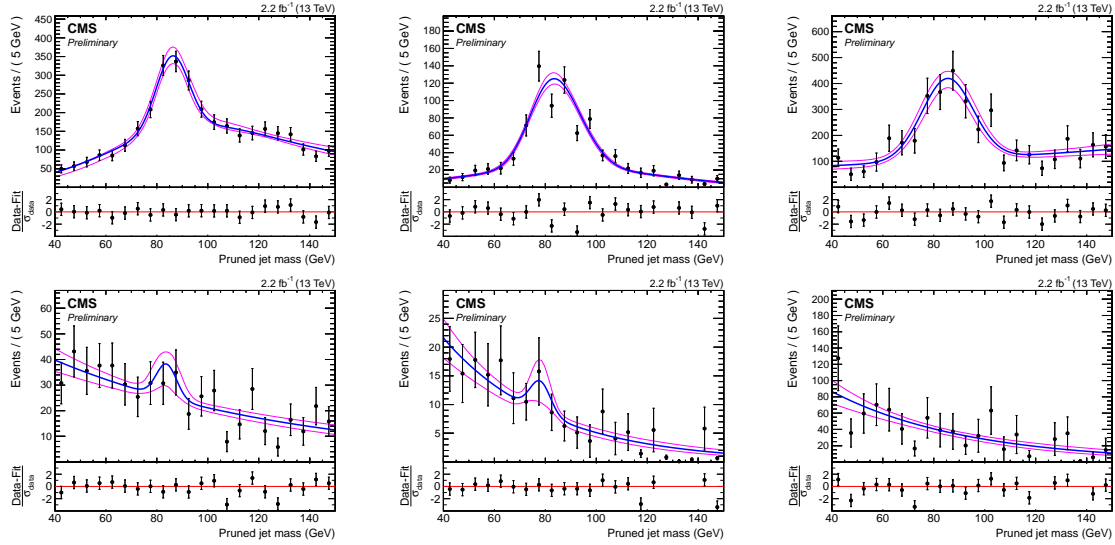


Figure 9.3: MC fits of non-dominant background m_{jet} spectra: on top (bottom) high purity (low purity) categories for the electron channel. Left to right are the $t\bar{t}$, diboson (WW/WZ/ZZ) and Single Top processes.

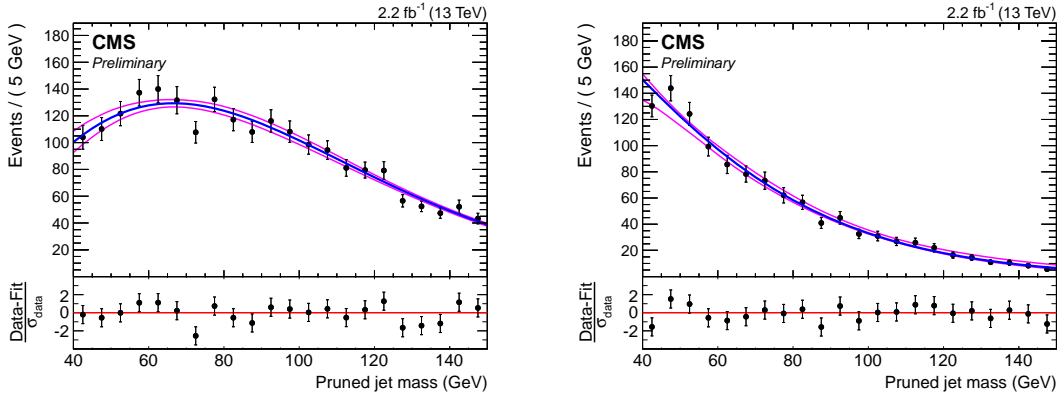


Figure 9.4: MC fits of dominant W+jets background m_{jet} spectra: high purity (left) and low purity (right) category for the electron channel.

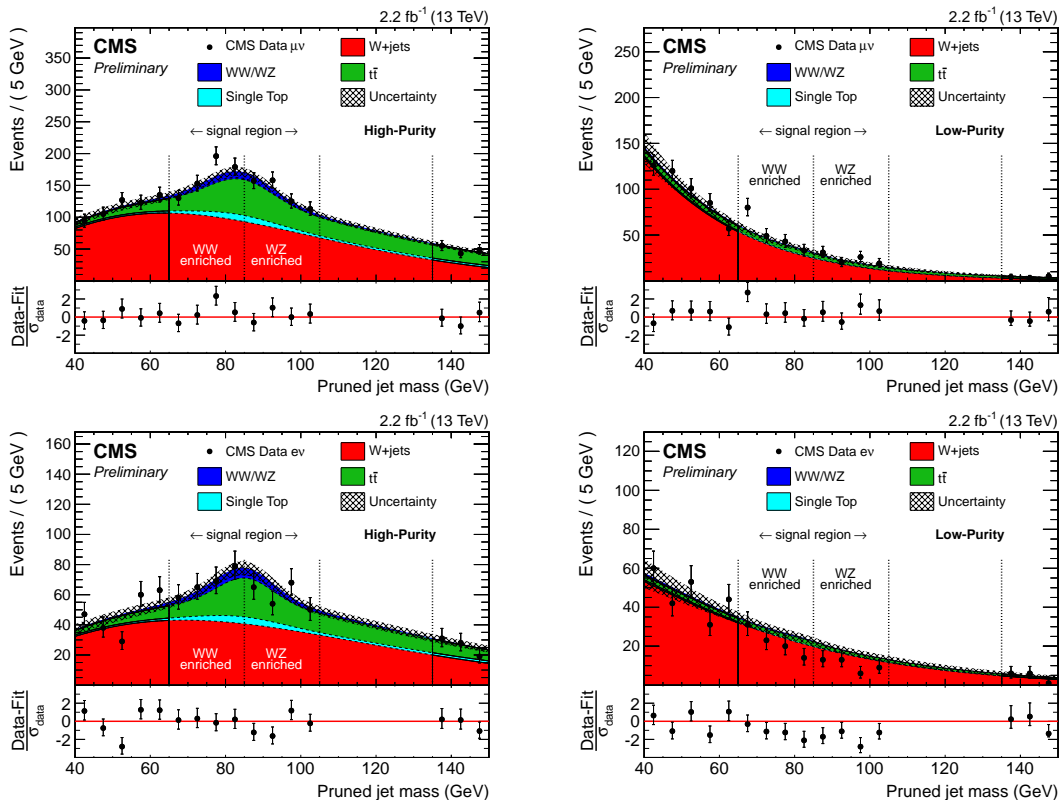


Figure 9.5: Fits to extract the relative shape and normalization of the W+jets contribution from the data in the jet mass distribution. Top line fits for the muon channel: high purity (left) and low purity (right) category. Bottom line fits for the electron channel: high purity (left) and low purity (right) category. The hashed area denotes the fit uncertainty, the shaded area the blinded W/Z/H signal region, and the vertical dashed lines separate the W, Z and H window from left to right.

9.1.3 Extraction of the W+jets shape

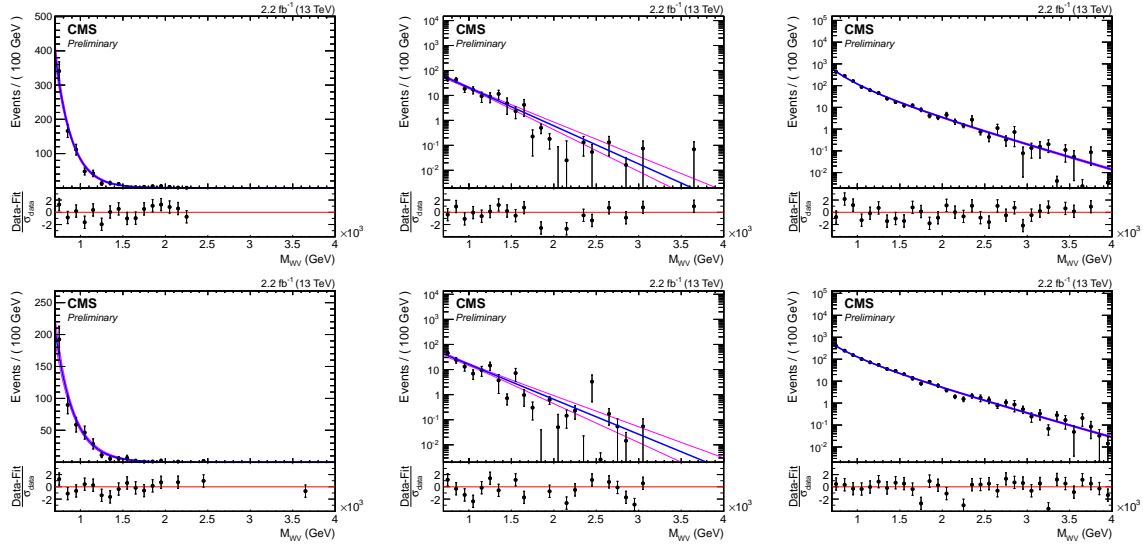


Figure 9.6: MC fits of non-dominant background $m_{\ell\nu j}$ spectra in the $m_{\text{jet}}^{\text{sideband}}$: on top (bottom) high purity (low purity) categories for the muon channel. Left to right are the $t\bar{t}$, diboson (WW/WZ/ZZ) and Single Top processes.

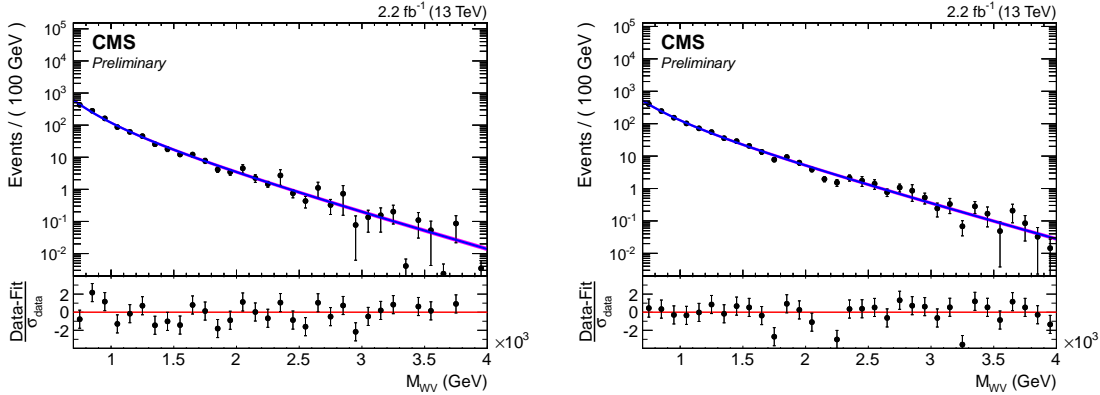


Figure 9.7: MC fits of dominant W+jets background $m_{\ell\nu j}$ spectra in the $m_{\text{jet}}^{\text{sideband}}$: high purity (left) and low purity (right) category for the muon channel.

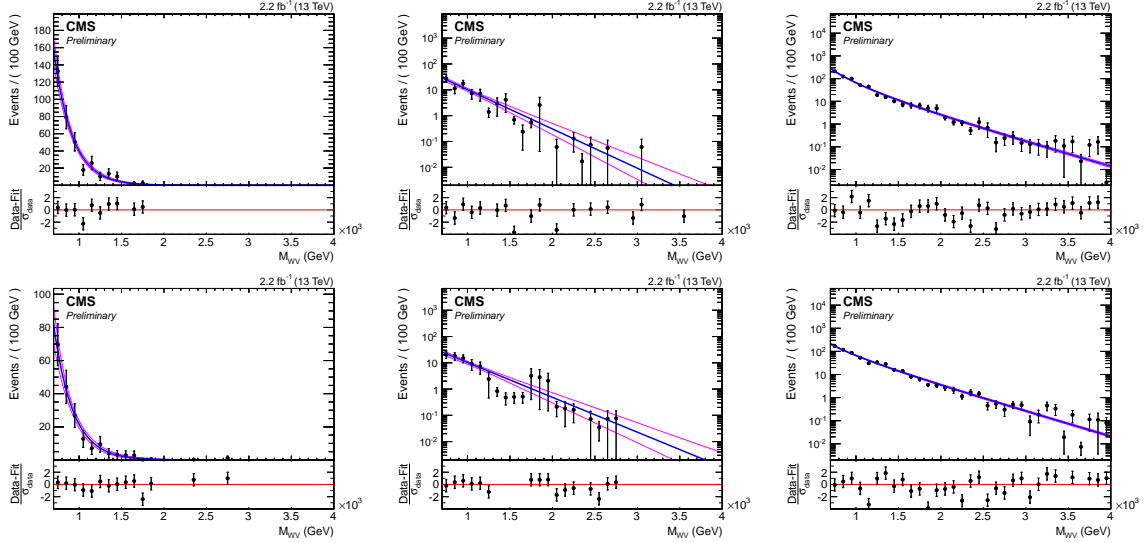


Figure 9.8: MC fits of non-dominant background $m_{\ell\nu j}$ spectra in the m_{jet} sideband: on top (bottom) high purity (low purity) categories for the electron channel. Left to right are the $t\bar{t}$, diboson (WW/WZ/ZZ) and Single Top processes.

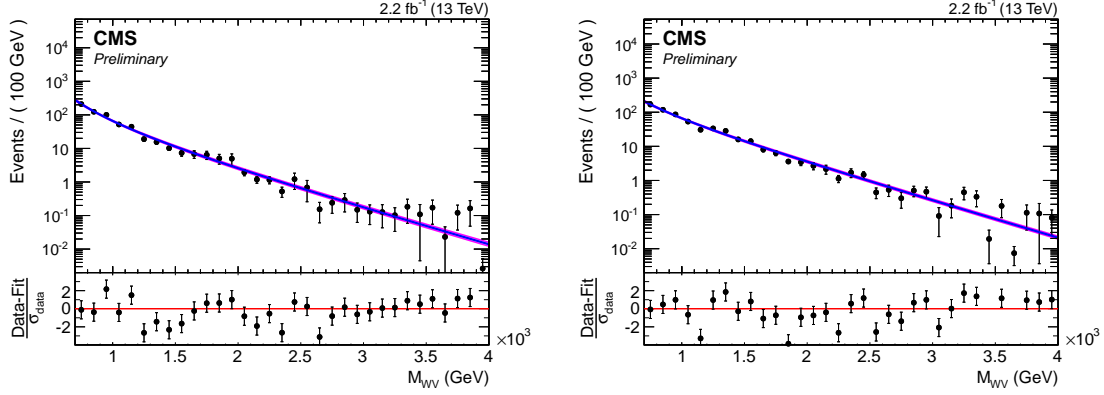


Figure 9.9: MC fits of dominant $W+jets$ background $m_{\ell\nu j}$ spectra in the m_{jet} sideband: high purity (left) and low purity (right) category for the electron channel.

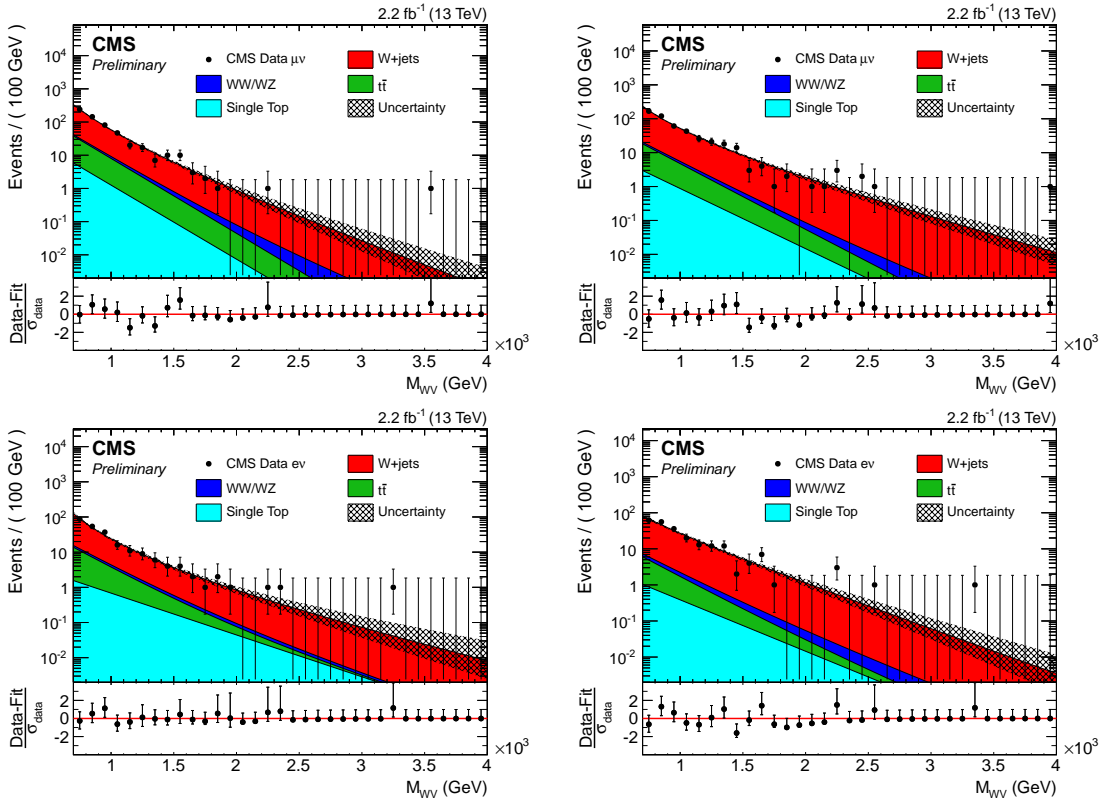


Figure 9.10: The fits for $F_{data,LSB}(m_{\ell\nu j})$ for both electron (bottom) and muon (top) channels, high purity (left) and low purity (right) categories.

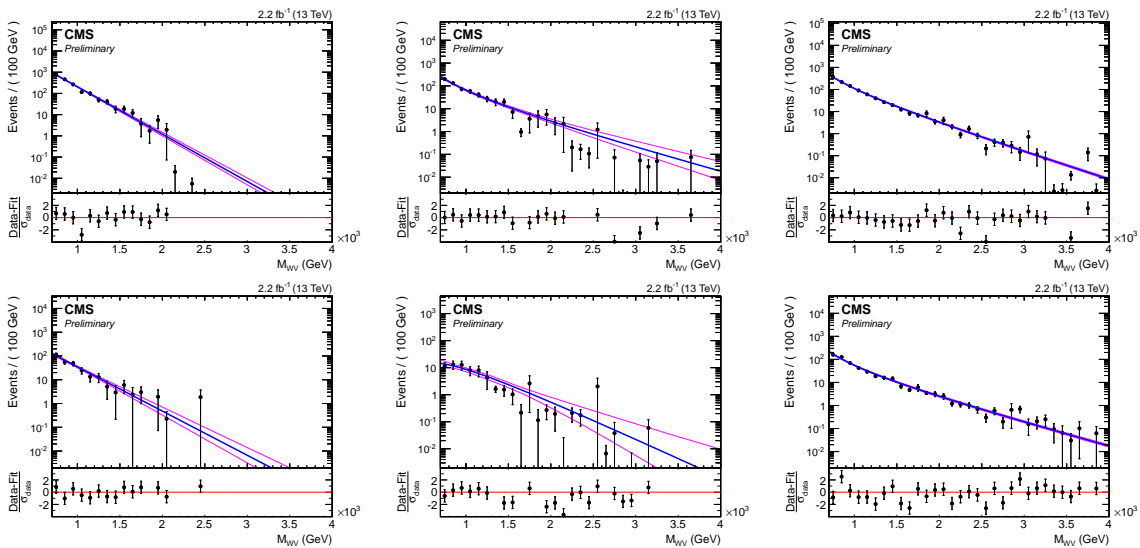


Figure 9.11: MC fits of non-dominant background $m_{\ell\nu j}$ spectra in the m_{jet} signal region for events in the WW category: on top (bottom) high purity (low purity) categories for the muon channel. Left to right are the $t\bar{t}$, diboson (WW/WZ/ZZ) and Single Top processes.

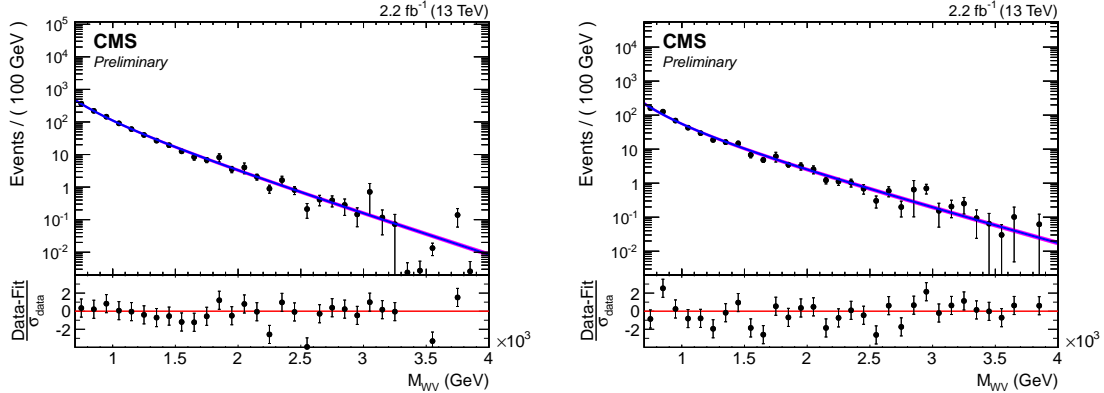


Figure 9.12: MC fits of dominant $W+jets$ background $m_{\ell\nu j}$ spectra in the m_{jet} signal region for events in the WW category: high purity (left) and low purity (right) category for the muon channel.

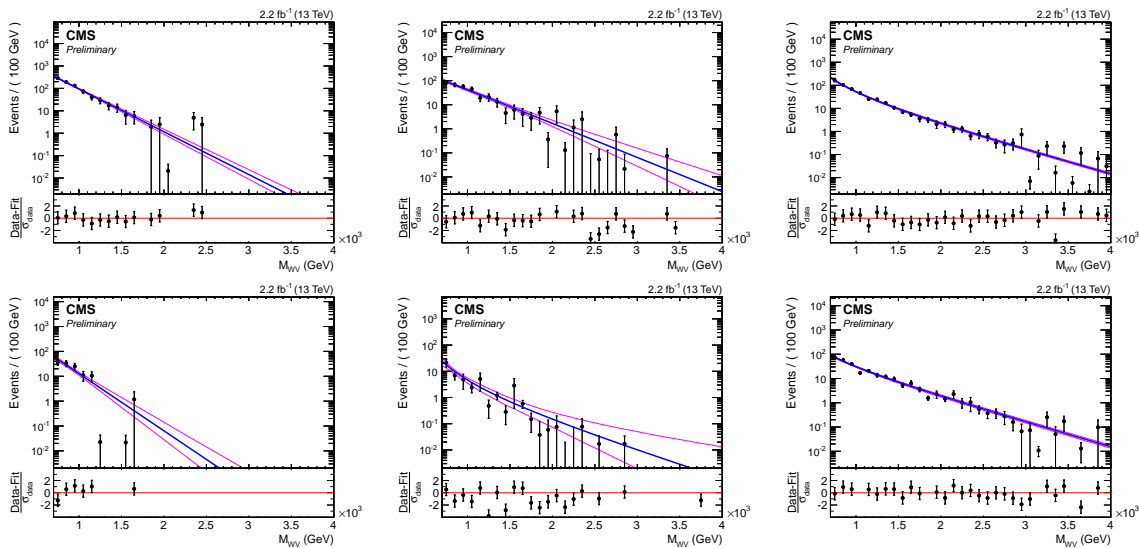


Figure 9.13: MC fits of non-dominant background $m_{\ell\nu j}$ spectra in the m_{jet} signal region for events in the WW category: on top (bottom) high purity (low purity) categories for the electron channel. Left to right are the $t\bar{t}$, diboson (WW/WZ/ZZ) and Single Top processes.

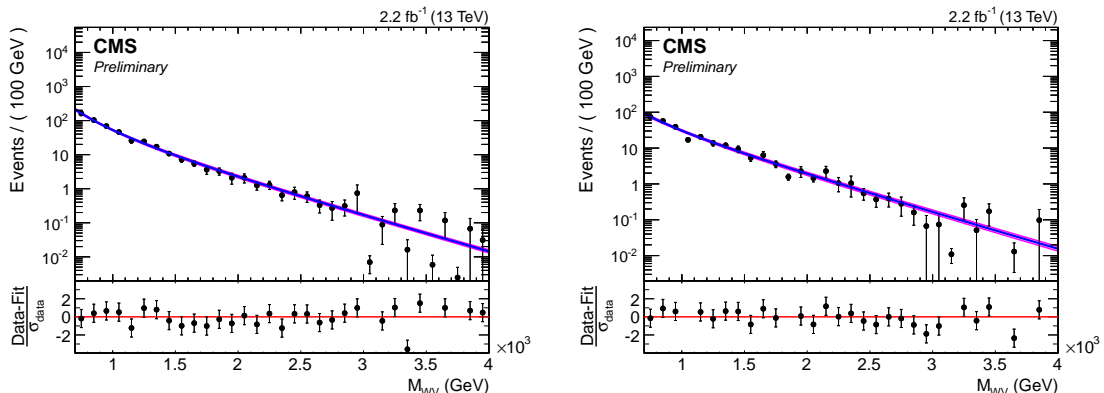


Figure 9.14: MC fits of dominant $W+jets$ background $m_{\ell\nu j}$ spectra in the m_{jet} signal region for events in the WW category: high purity (left) and low purity (right) category for the electron channel.

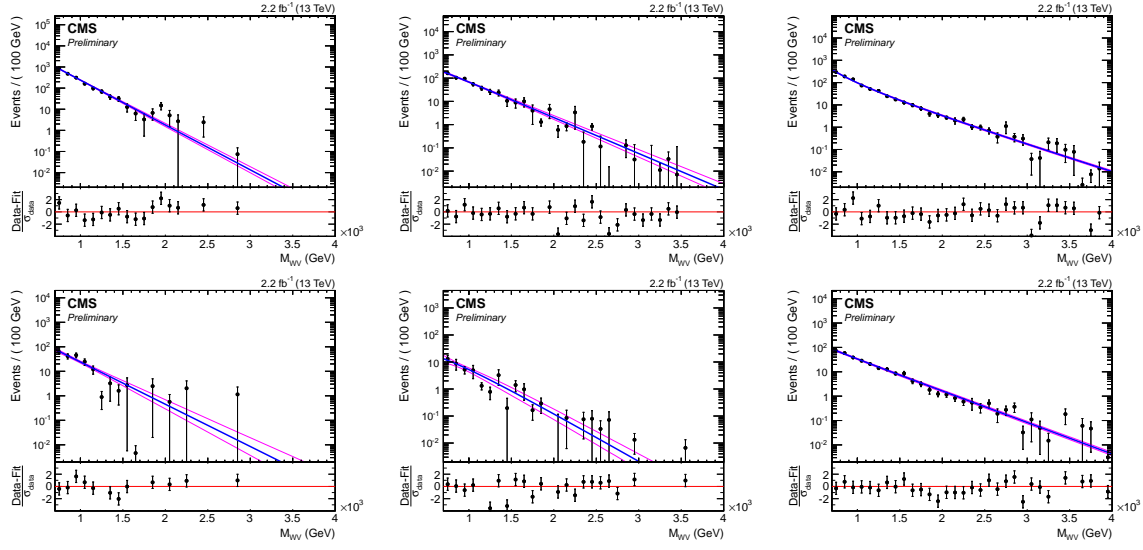


Figure 9.15: MC fits of non-dominant background $m_{\ell\nu j}$ spectra in the m_{jet} signal region for events in the WZ category: on top (bottom) high purity (low purity) categories for the muon channel. Left to right are the $t\bar{t}$, diboson (WW/WZ/ZZ) and Single Top processes.

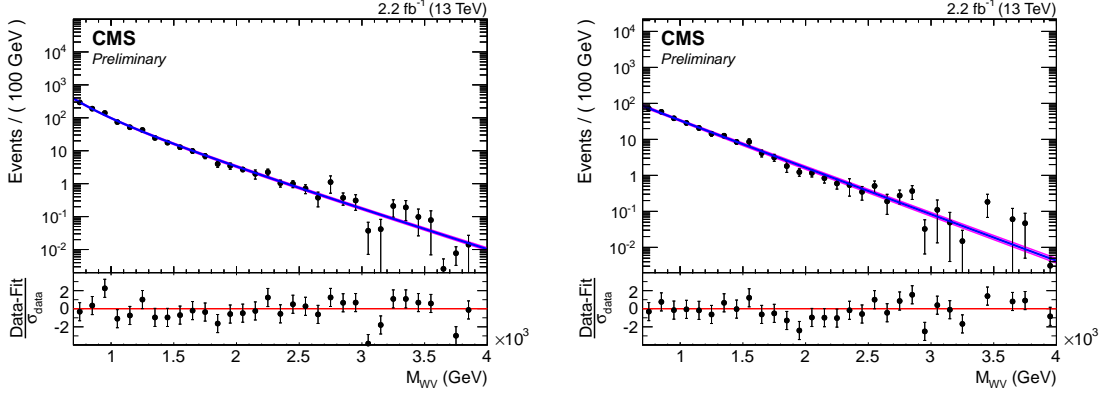


Figure 9.16: MC fits of dominant W+jets background $m_{\ell\nu j}$ spectra in the m_{jet} signal region for events in the WZ category: high purity (left) and low purity (right) category for the muon channel.

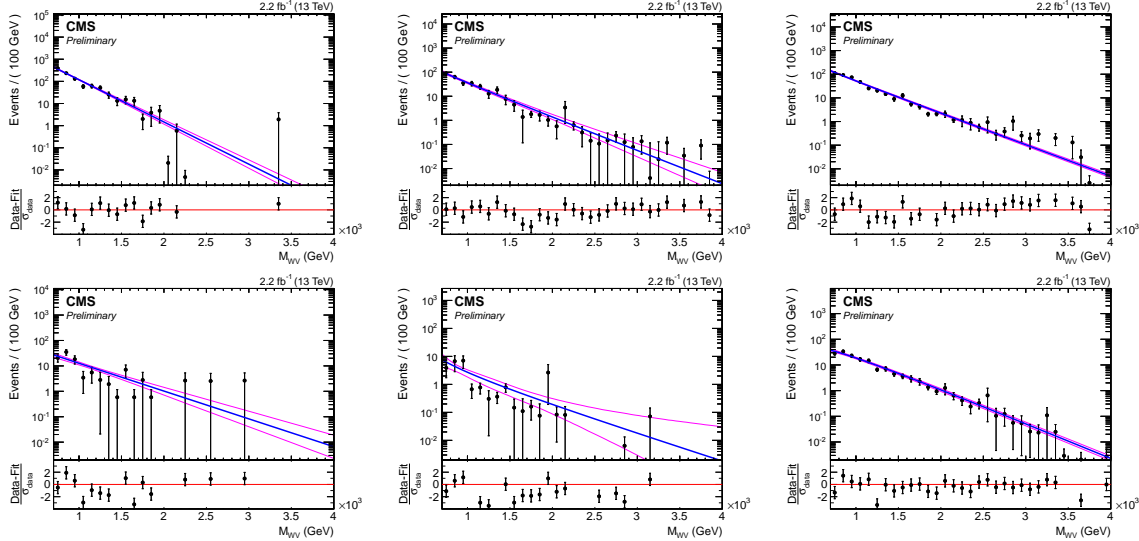


Figure 9.17: MC fits of non-dominant background $m_{\ell\nu j}$ spectra in the m_{jet} signal region for events in the WZ category: on top (bottom) high purity (low purity) categories for the electron channel. Left to right are the $t\bar{t}$, diboson (WW/WZ/ZZ) and Single Top processes.

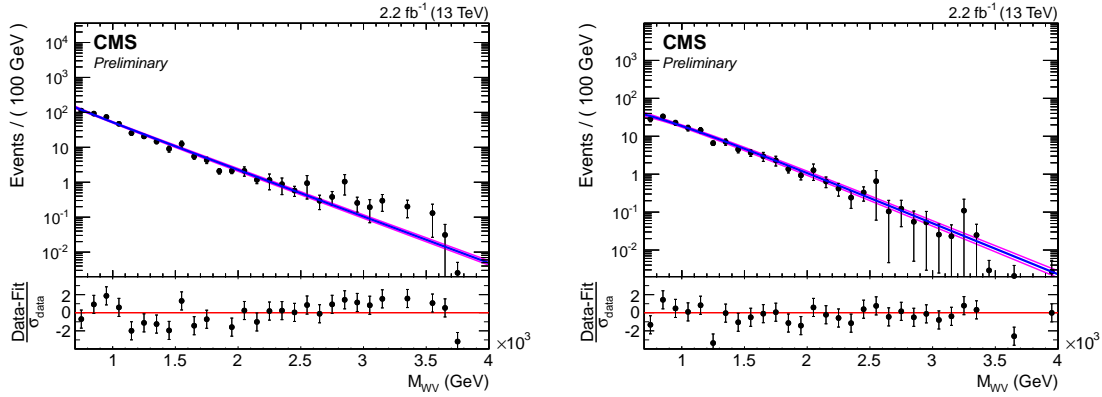


Figure 9.18: MC fits of dominant W+jets background $m_{\ell\nu j}$ spectra in the m_{jet} signal region for events in the WZ category: high purity (left) and low purity (right) category for the electron channel.

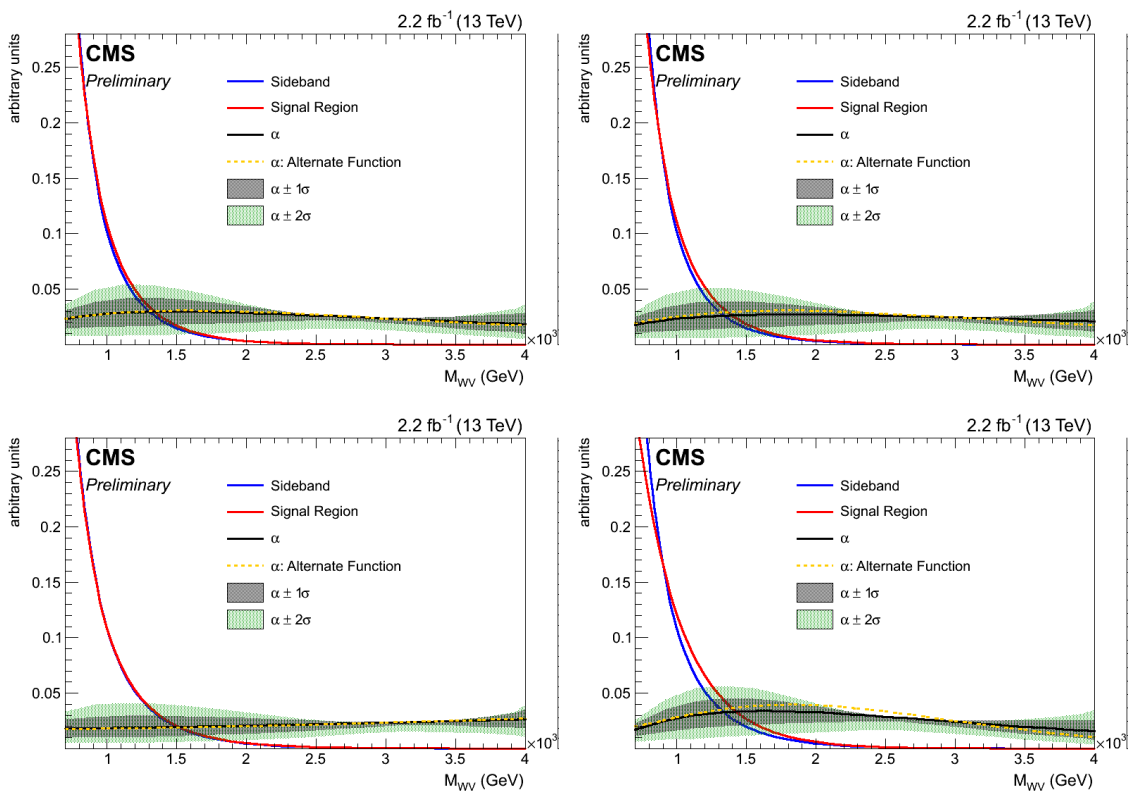


Figure 9.19: The functions $\alpha_{MC}(m_{\ell\nu_j})$ for the muon high purity category (top), low purity (bottom) categories used for extrapolate W+jets $m_{\ell\nu_j}$ shape in the WW (left) and WZ (right) signal regions.

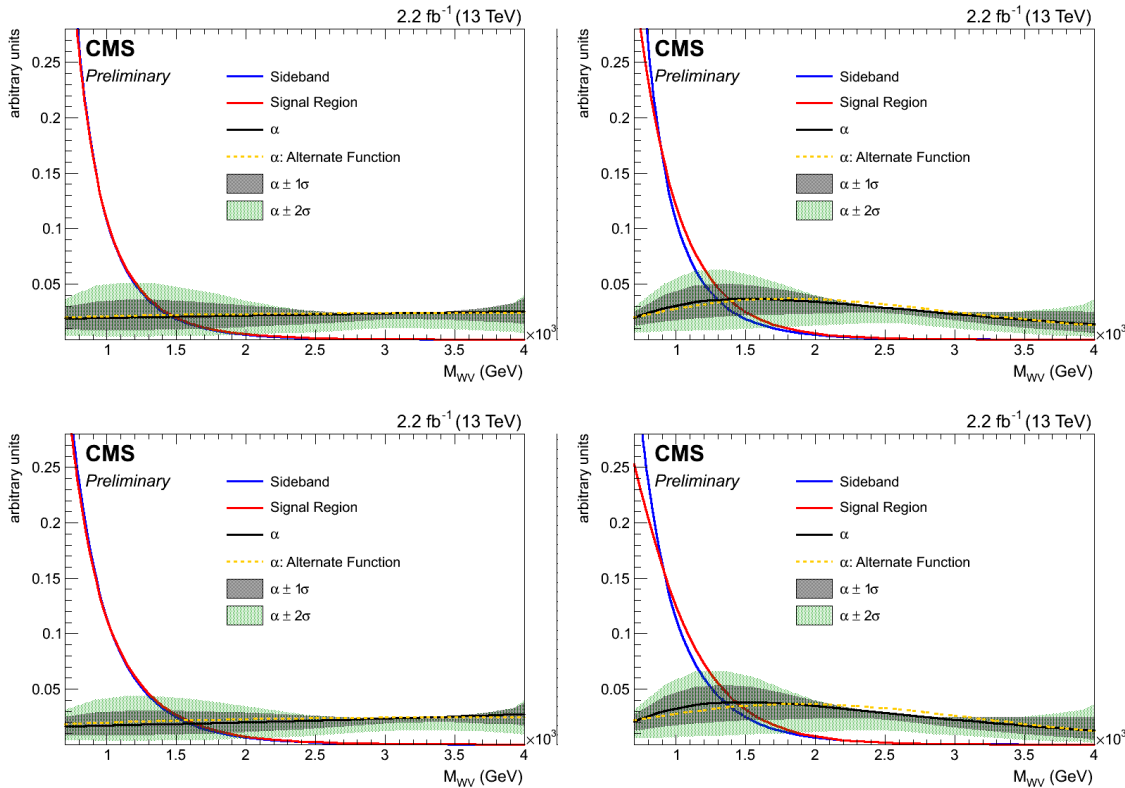


Figure 9.20: The functions $\alpha_{MC}(m_{\ell\nu j})$ for the electron high purity category (top), low purity (bottom) categories used for extrapolate $W+jets$ $m_{\ell\nu j}$ shape in the WW (left) and WZ (right) signal regions.

9.2 Top quark production

8 TeV analysis

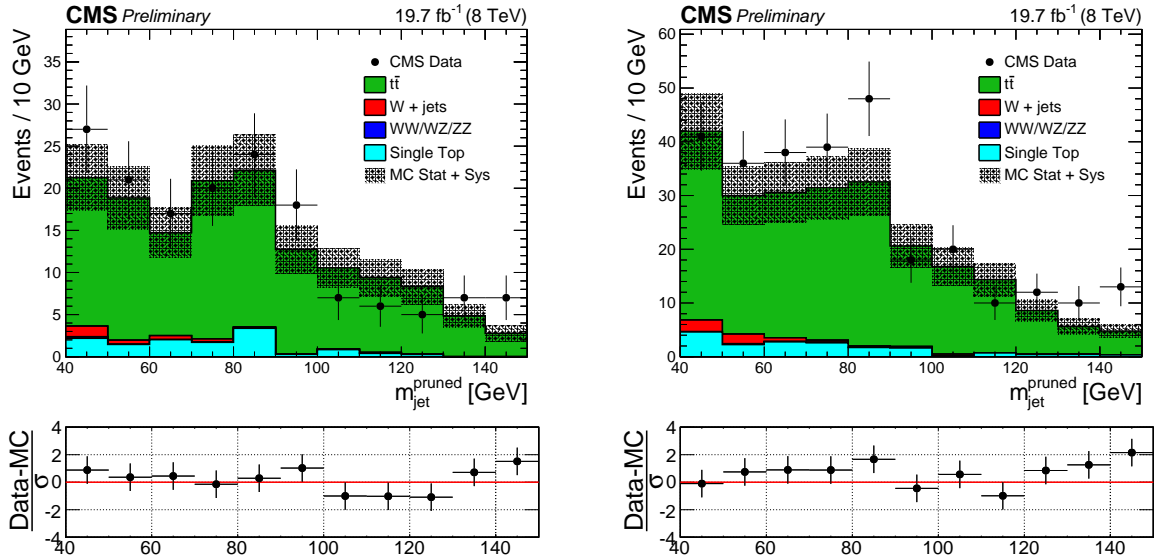


Figure 9.21: Pruned jet mass for electron channel (left) and muon channel (right) for events with $40 < m_{\text{jet}}^{\text{pruned}} < 150$ GeV in the $t\bar{t}$ control sample.

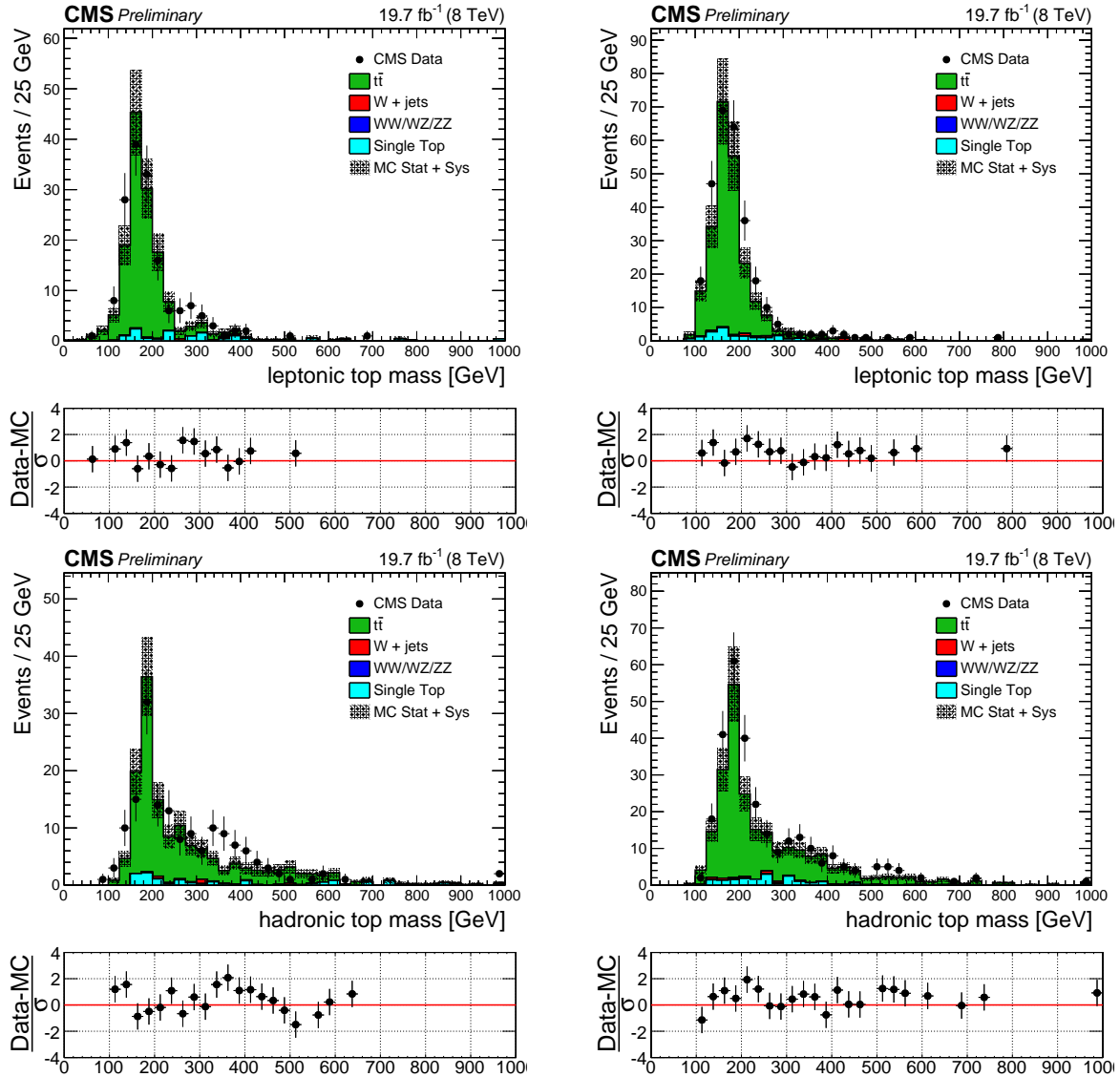


Figure 9.22: $m_{top}^{leptonic}$ (top) and $m_{top}^{hadronic}$ (bottom) for electron channel (left) and muon channel (right) for events with $40 < m_{jet}^{pruned} < 150$ GeV in the $t\bar{t}$ control sample.

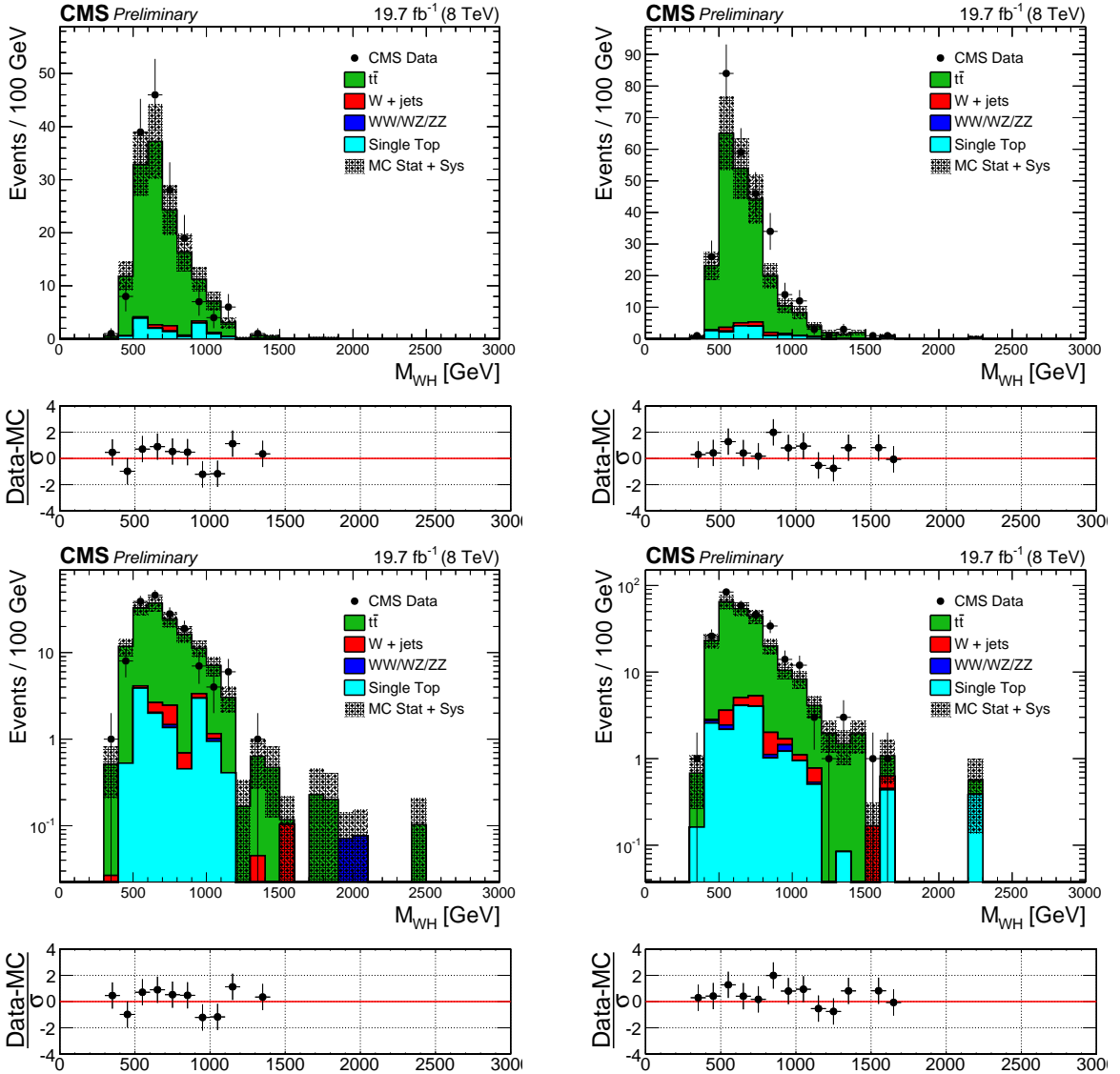


Figure 9.23: m_{WH} in linear (top) and log (bottom) scale for electron channel (left) and muon channel (right) for events with $40 < m_{jet}^{pruned} < 150$ GeV in the $t\bar{t}$ control sample.

13 TeV analysis

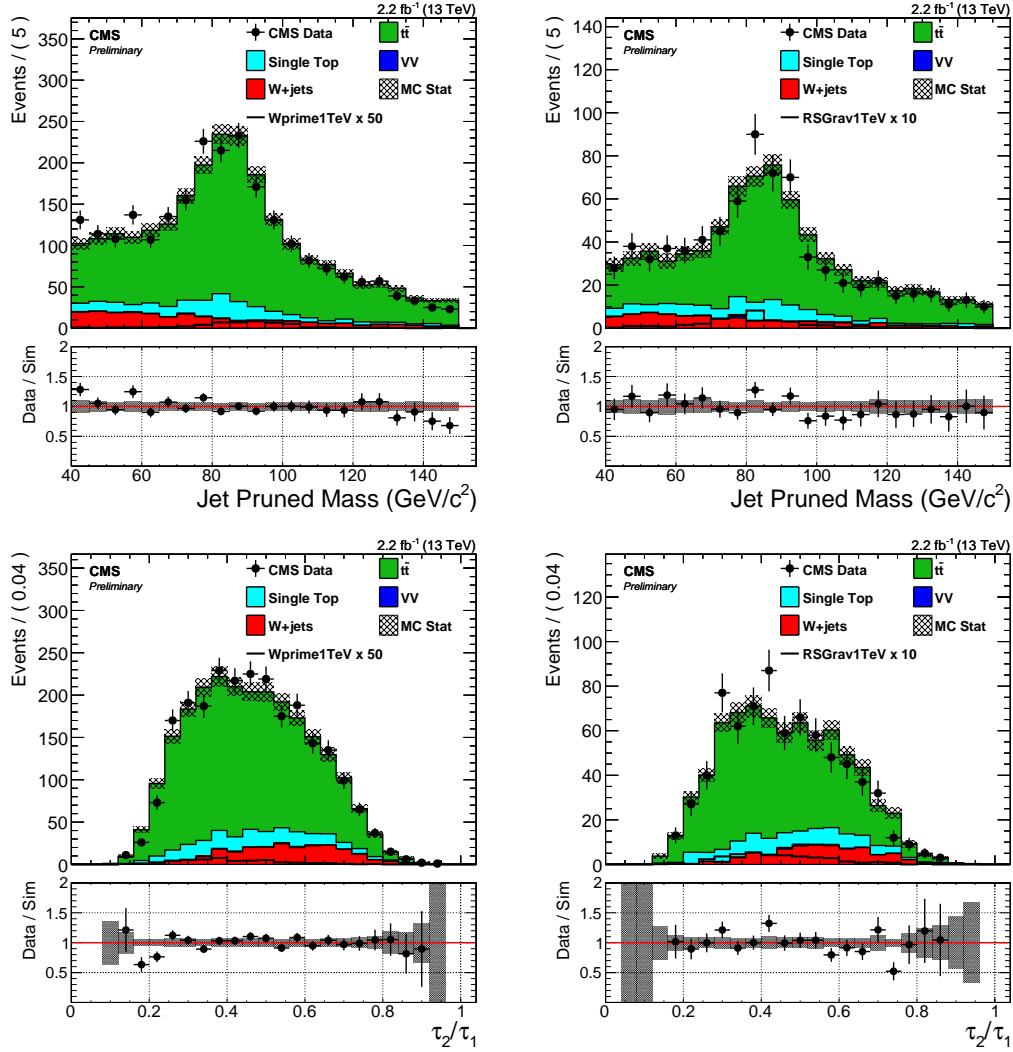


Figure 9.24: Comparison plots between data and MC for different observables, in the $t\bar{t}$ control region. Top: pruned jet mass. Bottom: N-subjettiness. Left: muon channel, right: electron channel.

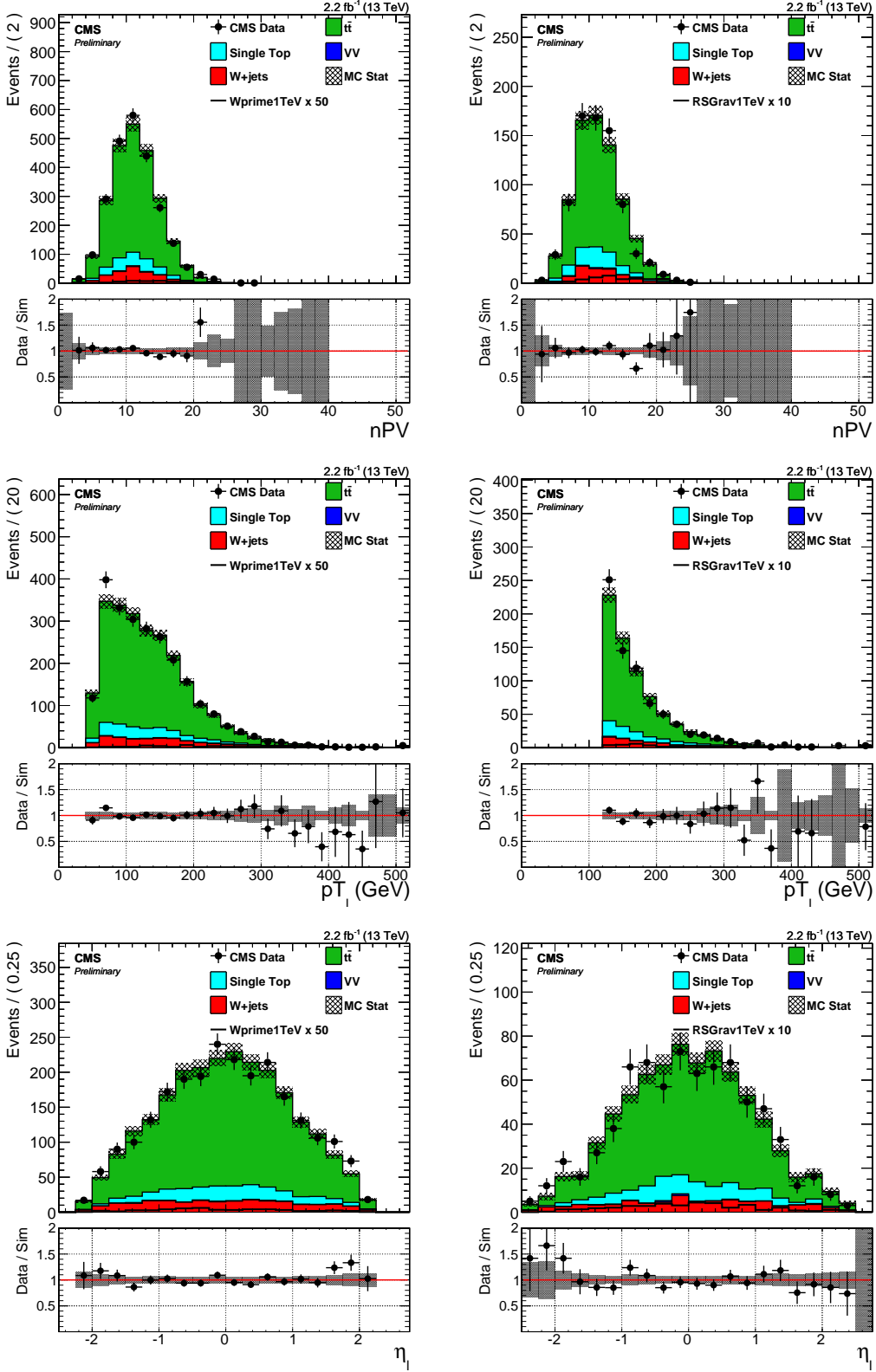


Figure 9.25: Comparison plots between data and MC for different observables, in the $t\bar{t}$ control region. From top to bottom: number of primary vertices, lepton p_T , lepton η . Left: muon channel, right: electron channel.

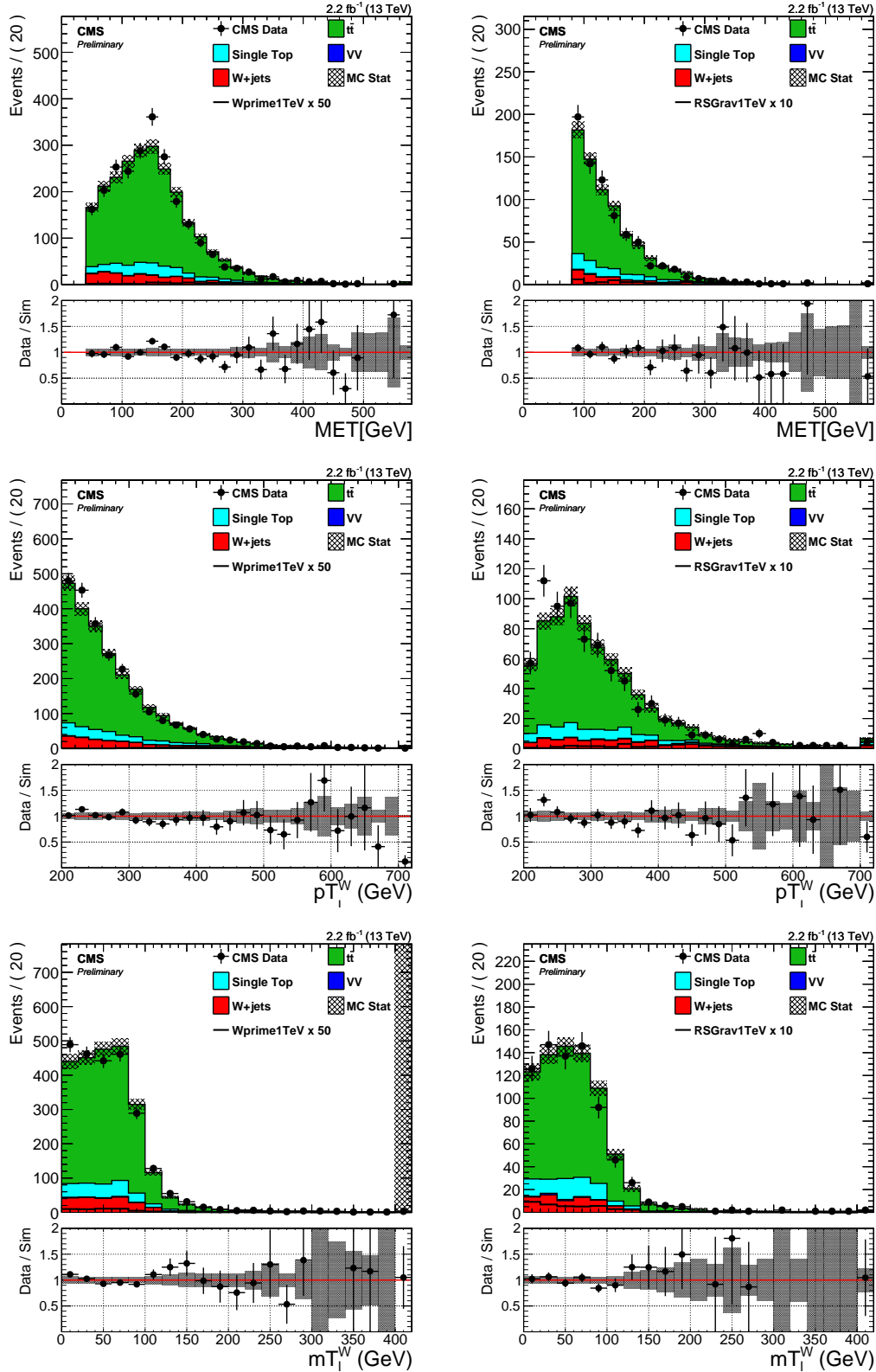


Figure 9.26: Comparison plots between data and MC for different observables, in the $t\bar{t}$ control region. From top to bottom: E_T^{miss} , leptonic W p_T , transverse mass of the leptonic W . Left: muon channel, right: electron channel.

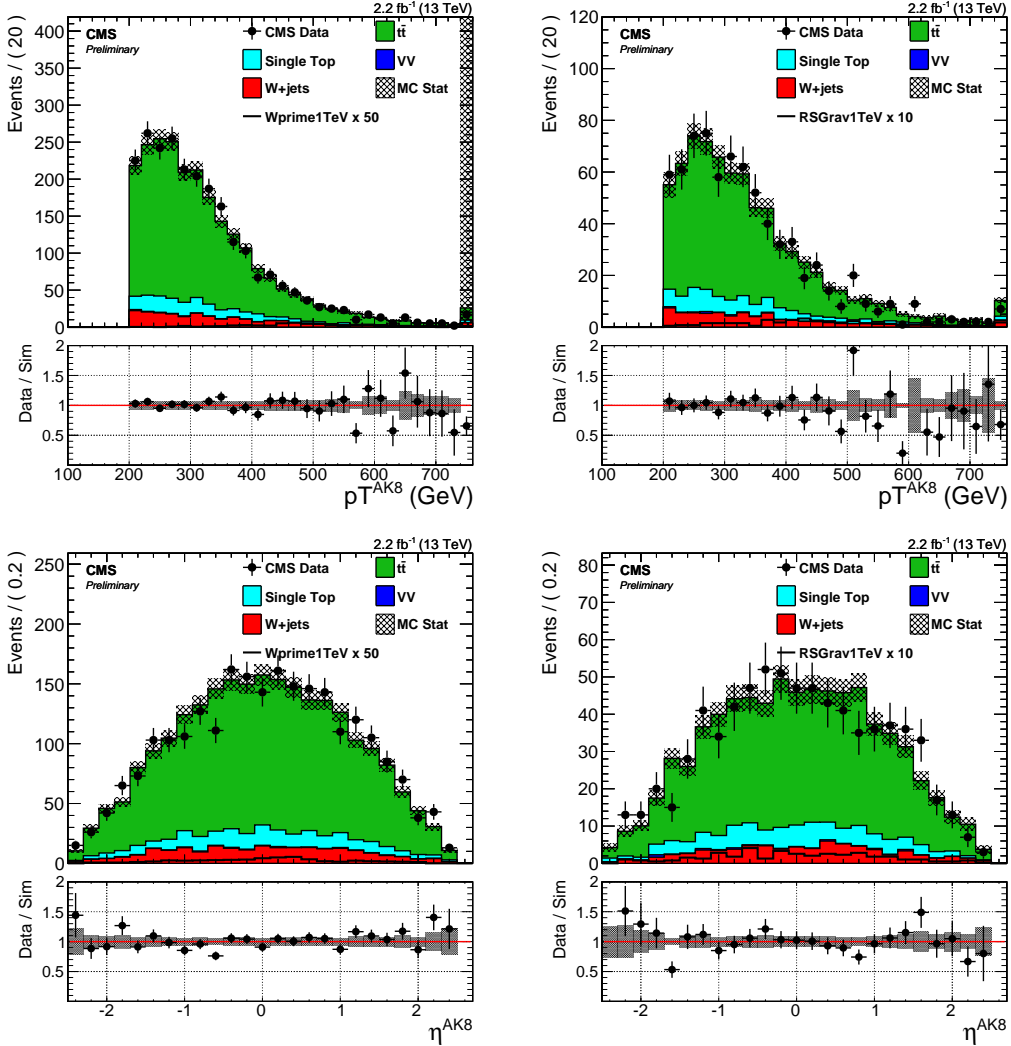


Figure 9.27: Comparison plots between data and MC for different observables, in the $t\bar{t}$ control region. Top: p_T of the leading AK8 jet. Bottom: η of the leading AK8 jet. Left: muon channel, right: electron channel.

9.3 Systematic uncertainties in the background estimation

Signal modeling and statistical treatment

10.1 Signal modeling

10.1.1 Parametrization of the resonance mass

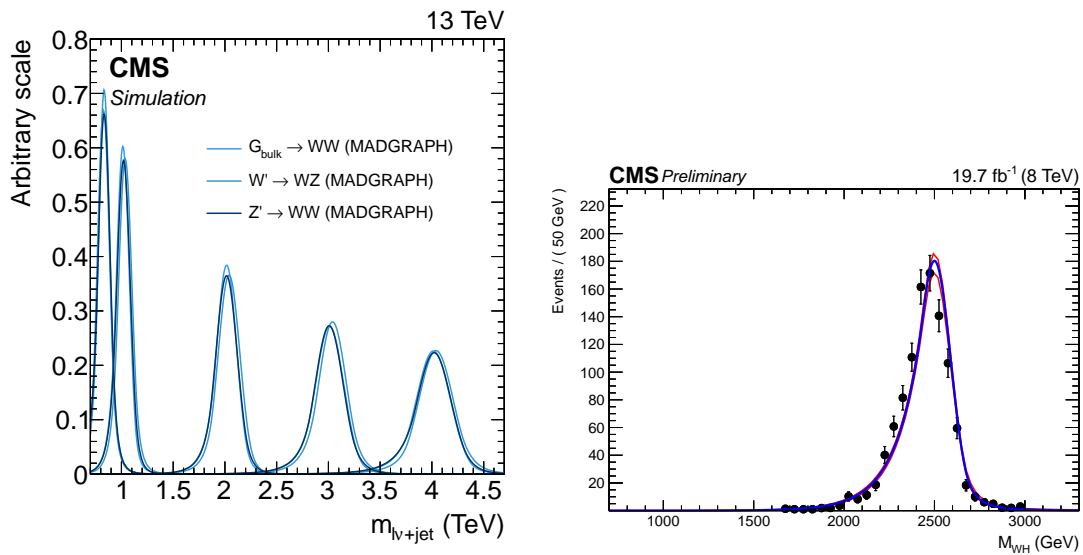


Figure 10.1: $ml?+jet$ (right) distribution for different signal mass hypotheses used to extract the signal shape.

10.1.2 Signal efficiency

10.2 Systematic uncertainties in the signal prediction

10.3 Testing new resonance hypothesis

10.3.1 Profile likelihood procedure

10.3.2 The CL_s method

10.3.3 Treatment of uncertainties

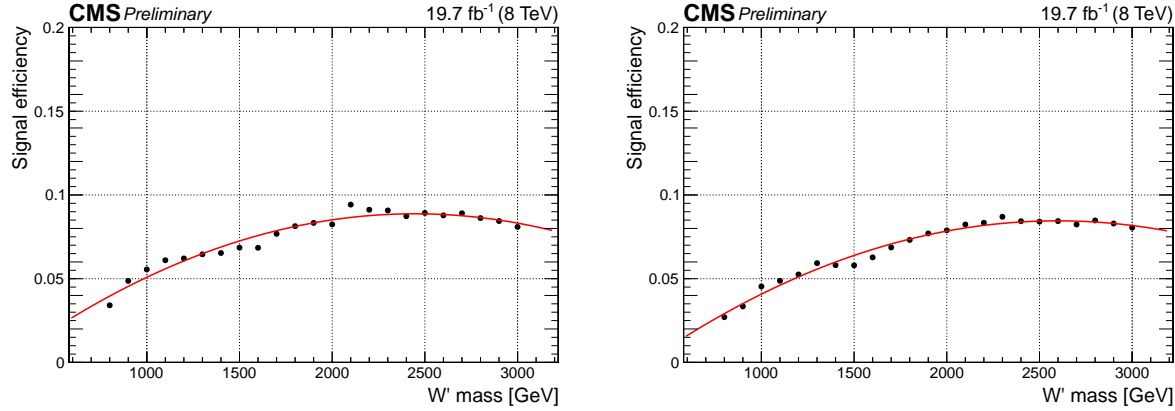


Figure 10.2: Signal efficiency for the final selection criteria as a function of the W' mass hypothesis in the muon (left) and electron (right) channel.

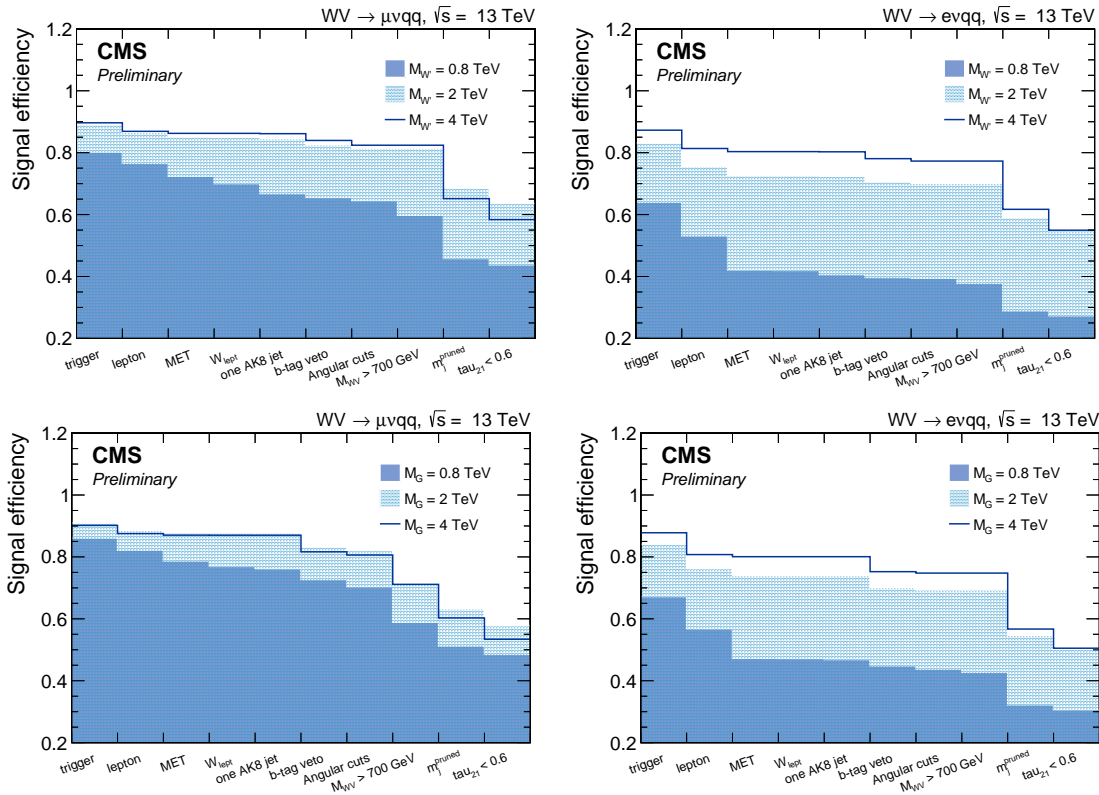


Figure 10.3: Expected signal efficiency of each selection in the muon (left) and electron (right) channels for 3 mass points, for W' (top) and BulkG (bottom) signal models.

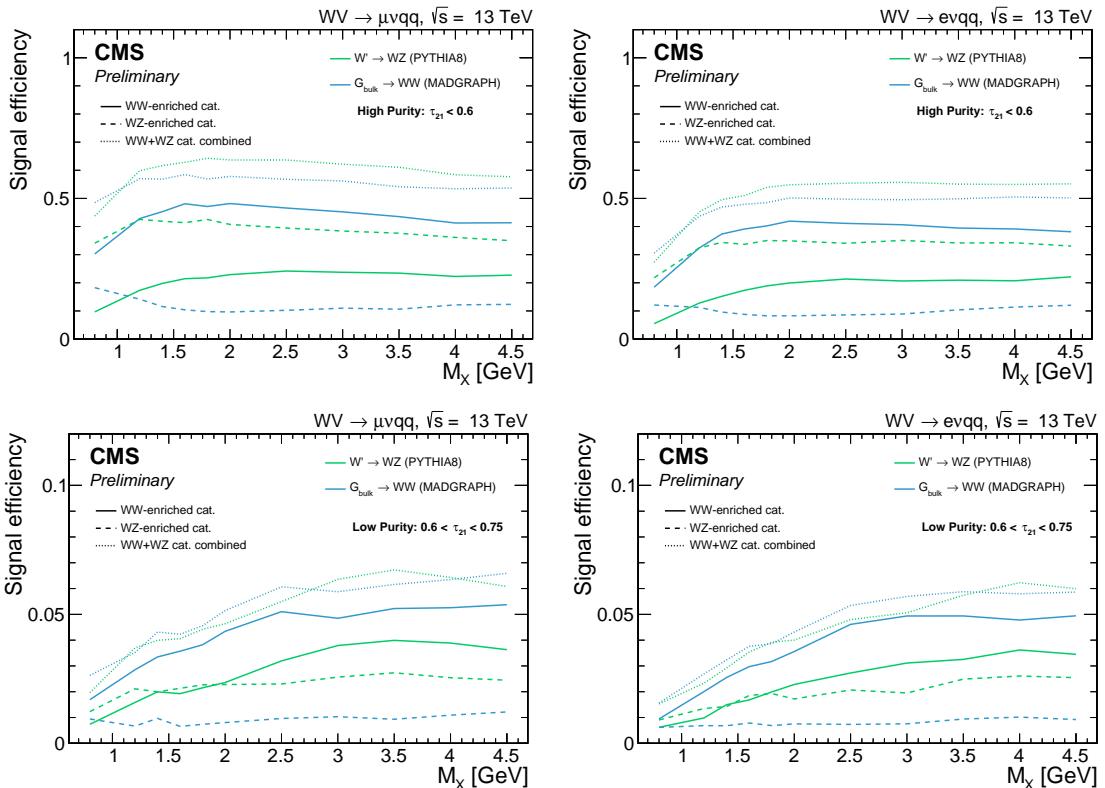


Figure 10.4: Expected signal efficiency for high-purity (top) and low-purity (bottom) categories, in electron (left) and muon (right) channel separately, for several resonance mass hypothesis. The efficiencies for the W-mass cut, the Z-mass cut and for the mass categories combined are also shown.

Results with 8 TeV data

11.1 Final m_{WH} distribution

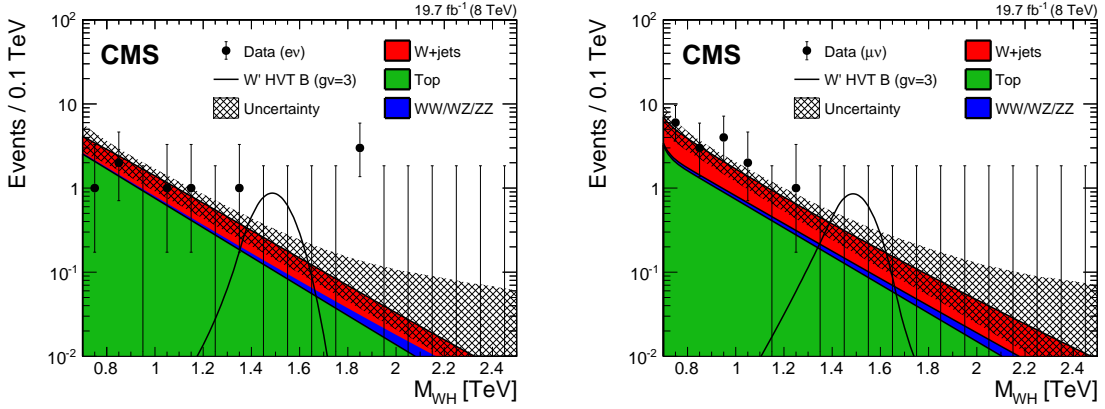


Figure 11.1: Final distributions in m_{WH} for data and expected backgrounds for electron (left) and muon (right) categories. The 68% error bars for Poisson event counts are obtained from the Neyman construction [?]. The hatched region indicates the statistical uncertainty of the fit combined with the systematical uncertainty in the shape. This figure also shows a hypothetical W' signal with mass of 1.5 TeV, normalized to the cross section predicted by the HVT model B with parameter $g_V = 3$ as described in Section.

11.2 Studies on the excess

11.3 Significance of the data

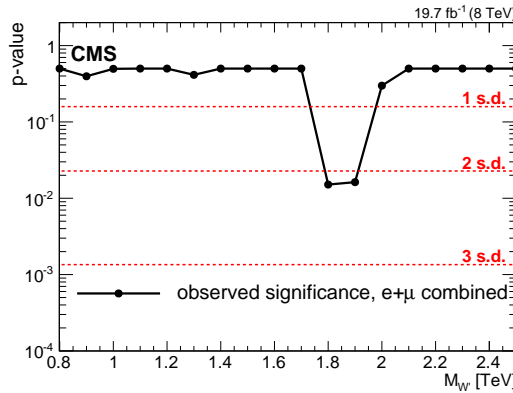


Figure 11.2: Local p-value of the combined electron and muon data as a function of the W' boson mass, probing a narrow WH resonance.

11.4 Cross section limits

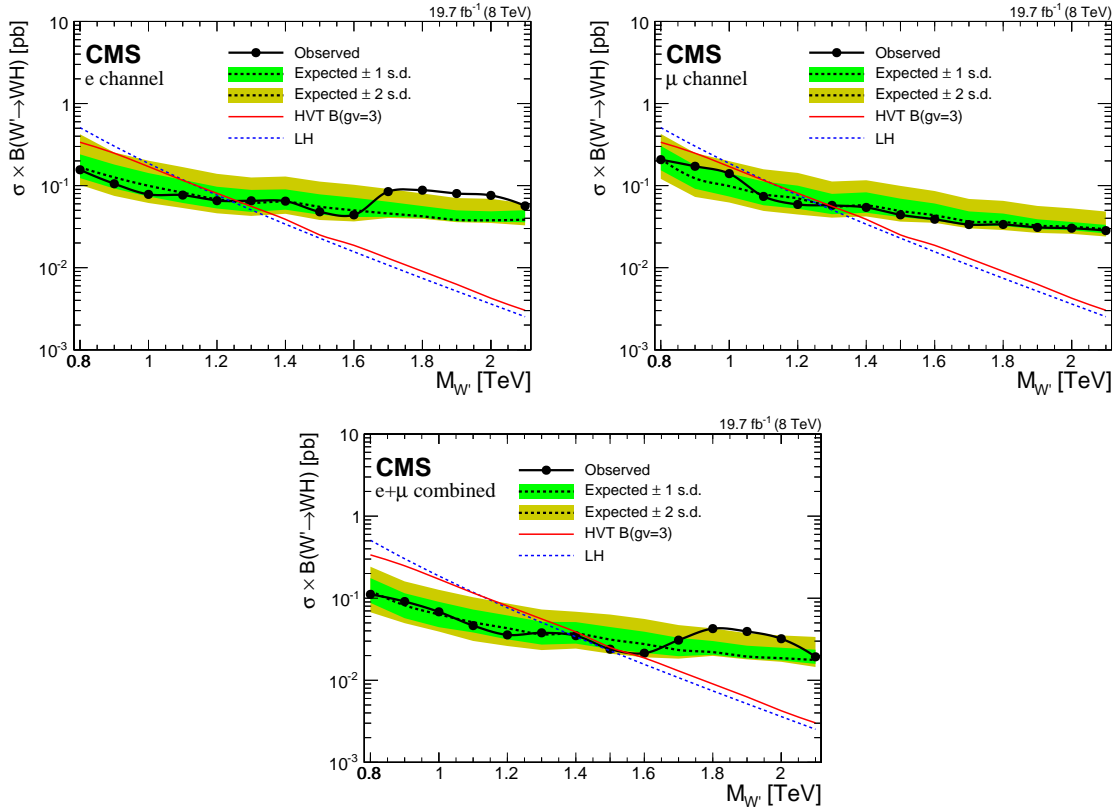


Figure 11.3: Observed (solid) and expected (dashed) upper limits at 95% CL on the product of the W' production cross section and the branching fraction of $W' \rightarrow WH$ for electron (left) and muon (right) channels, and the combination of the two channels (lower plot). The products of cross sections and branching fractions for W' production in the LH and HVT models are overlaid.

Results with 13 TeV data

12.1 Final m_{WV} distribution

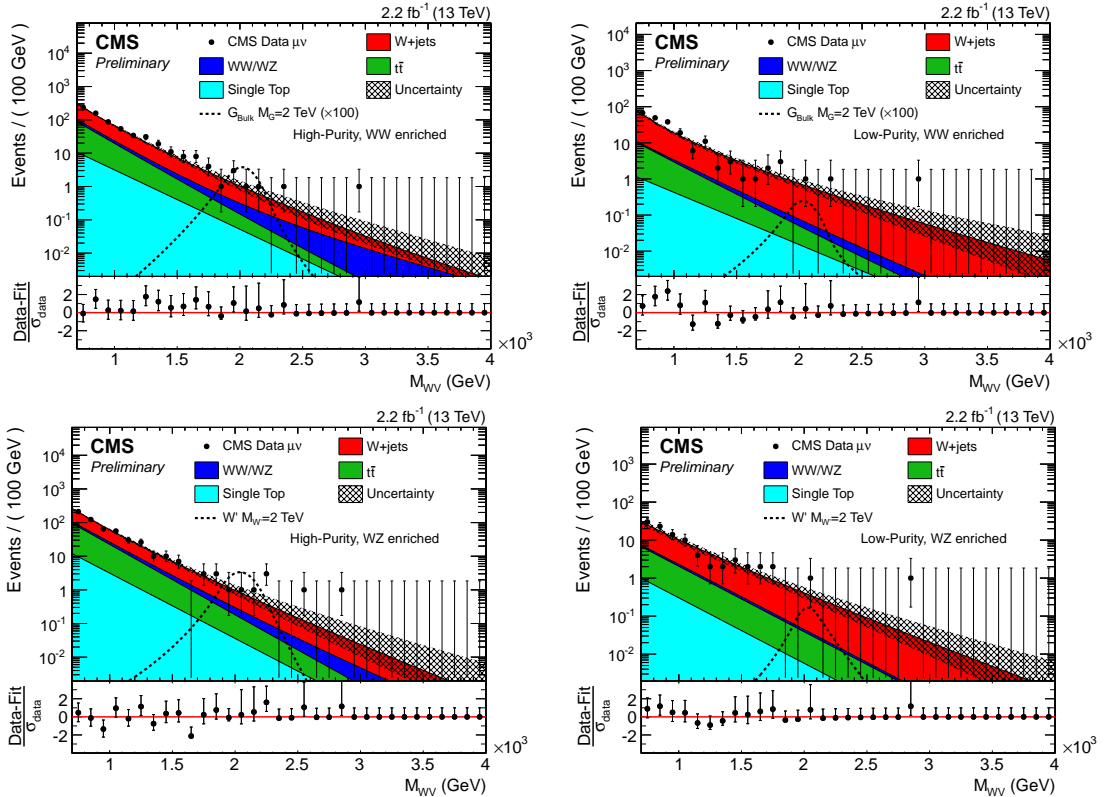


Figure 12.1: Examples of m_J extrapolation of the $m_{\ell\nu j}$ shape into the Signal Region for the muon channel for the HP (left) and LP (right) categories in the WW (top) and WZ (bottom) signal regions. The expected shape for a Bulk Graviton and for a W' with a mass of 2 TeV is also shown in the WW-enriched and WZ-enriched category, respectively.

12.2 Cross section limits

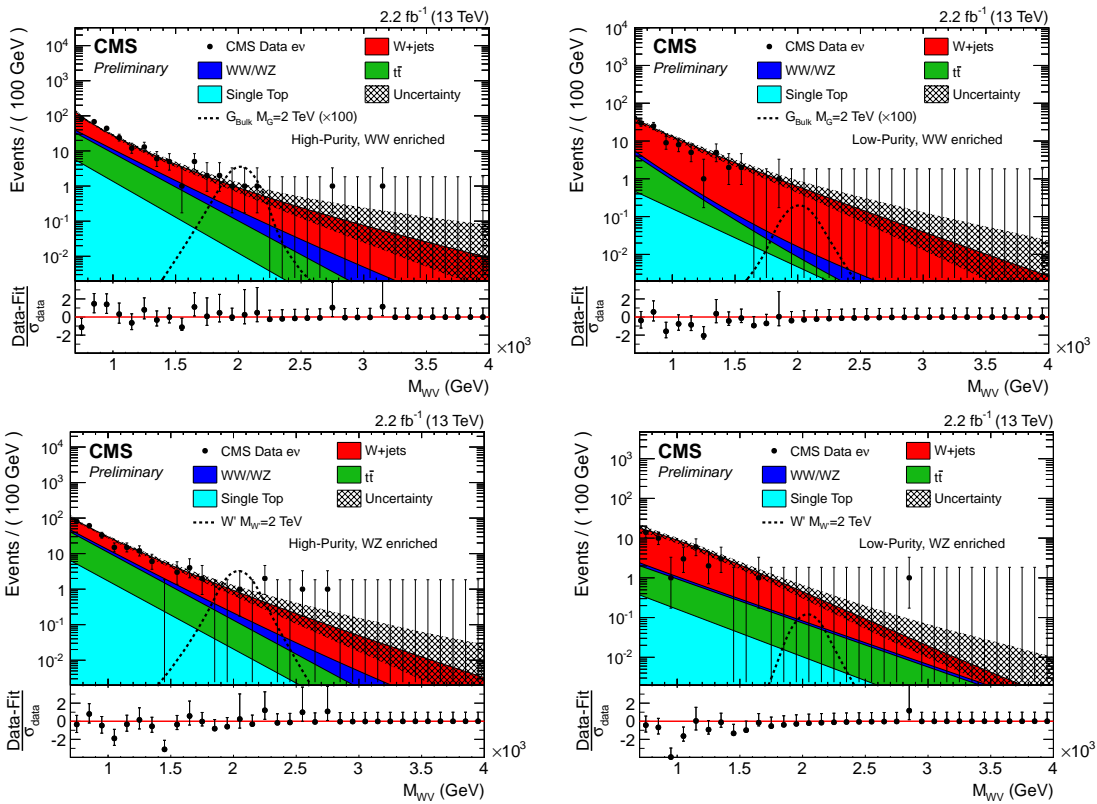


Figure 12.2: Examples of m_J extrapolation of the $m_{\ell\nu j}$ shape into the Signal Region for the electron channel for the HP (left) and LP (right) categories in the WW (top) and WZ (bottom) signal regions. The expected shape for a Bulk Graviton and for a W' with a mass of 2 TeV is also shown in the WW-enriched and WZ-enriched category, respectively.

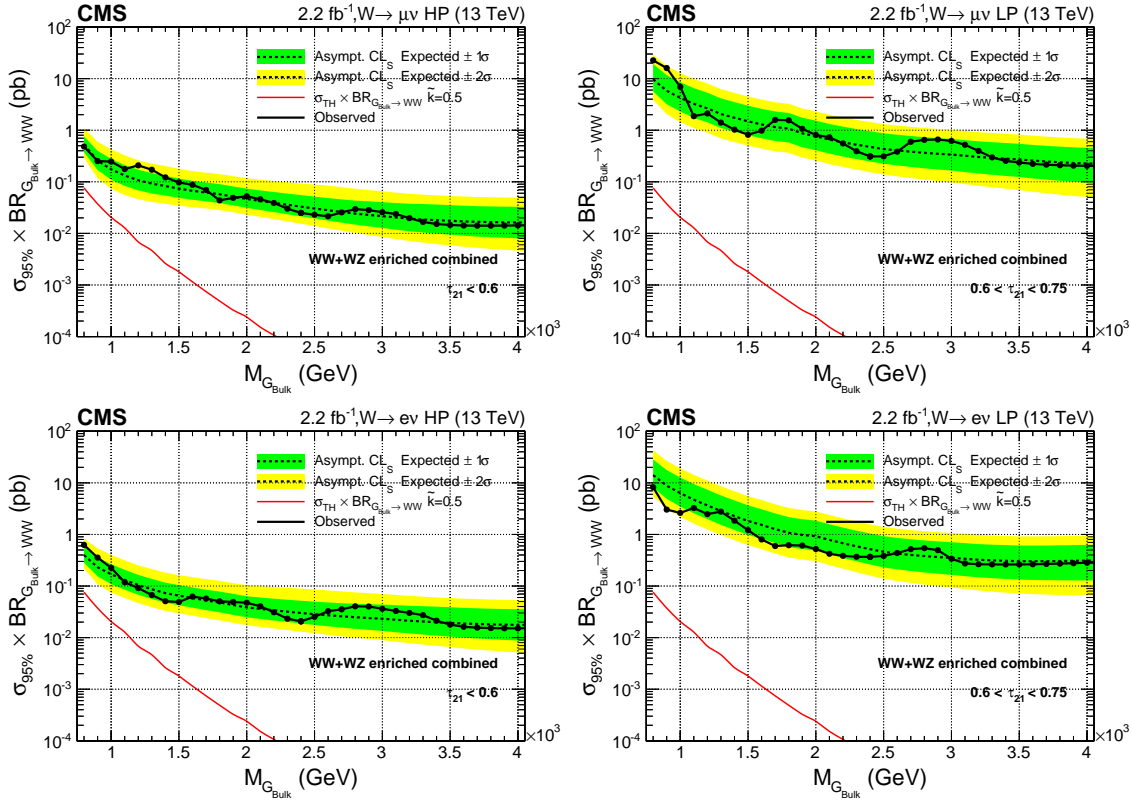


Figure 12.3: Expected 95% CL upper limit on graviton production cross section times the branching fraction of $G_{bulk} \rightarrow WW$ assuming 2.1 fb^{-1} of data. The limit is obtained with the Asymptotic CLs technique. The 68% and 95% ranges of expectation are also shown with green and yellow bands. The expected product between the Bulk graviton production cross section and the branching fraction is shown as a red solid curve for $\tilde{k} = 0.5$. Top panel: results for muon channel, HP category on the left, LP on the right. Bottom panel: results for electron channel, HP category on the left, LP on the right.

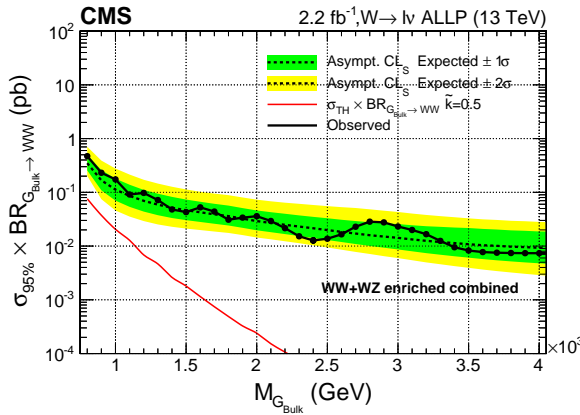


Figure 12.4: Expected 95% CL upper limit on the graviton production cross section times the branching fraction of $G_{bulk} \rightarrow WW$ assuming 2.1 fb^{-1} of data. The limit is obtained with the Asymptotic CLs technique. The 68% and 95% ranges of expectation are also shown with green and yellow bands. The expected product between the Bulk graviton production cross section and the branching fraction is shown as a red solid curve for $\tilde{k} = 0.1$.

Combination of searches for diboson resonances at $\sqrt{s} = 8$ and 13 TeV

13.1 Inputs to the combination

- 13.1.1 8 TeV VV searches
- 13.1.2 13 TeV VV searches
- 13.1.3 8 TeV VH searches
- 13.1.4 13 TeV VH searches

13.2 Combination procedure

13.3 Results

- 13.3.1 Limits on W'
- 13.3.2 Limits on Z'
- 13.3.3 Limits on heavy vector triplet ($W' + Z'$)
- 13.3.4 Limits on Bulk Graviton
- 13.3.5 Significance at 2 TeV

Table 13.1: Statistical significance of excesses observed at 1.8 TeV in the various searches, expressed in standard deviations.

Combination	W'	Z'	HVT ($W' + Z'$)	G_{bulk}
VV 13 TeV	0.00	0.10	0.00	0.00
VV+VH 13 TeV	0.00	0.00	0.00	-
VV 8 TeV	1.22	0.56	1.03	1.61
VV 8+13 TeV	0.20	0.46	0.33	0.35
VH 8 TeV	2.05	0.56	1.79	-
VV+VH 8 TeV	2.22	0.77	1.95	-
VV+VH 8+13 TeV	0.86	0.00	0.83	-

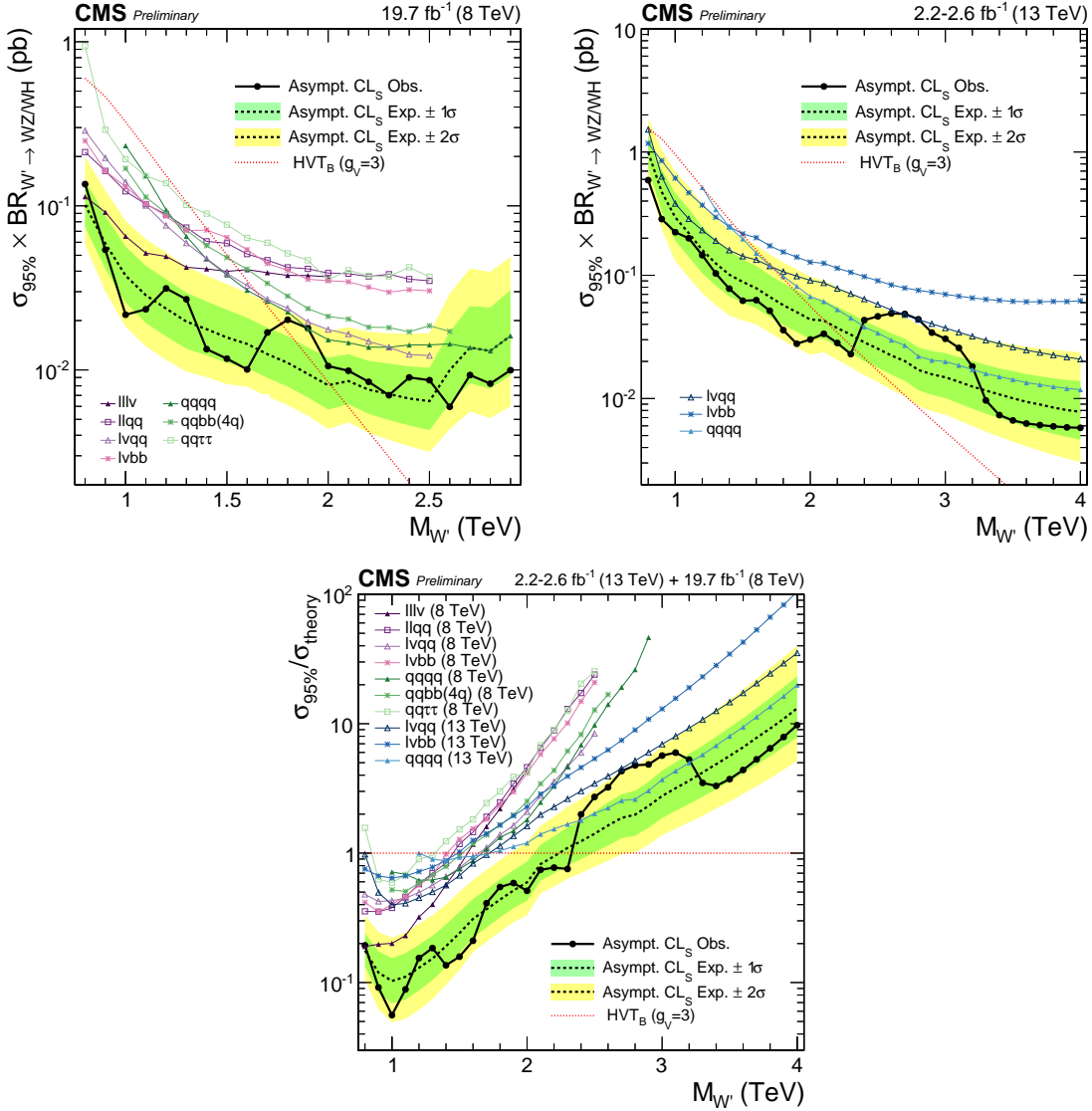


Figure 13.1: (top left) Observed (black solid) and expected (black dashed) exclusion limits at 95% CL on $\sigma(pp \rightarrow W' \rightarrow WZ/WH)$ as a function of the resonance mass obtained by combining the 8 TeV diboson searches. The curve corresponding to the cross sections predicted by the HVT model B is overlaid. (top right) Observed (black solid) and expected (black dashed) exclusion limits at 95% CL on $\sigma(pp \rightarrow W' \rightarrow WZ/WH)$ as a function of the resonance mass obtained by combining the 13 TeV diboson searches. The curve corresponding to the cross sections predicted by the HVT model B is overlaid. (bottom) Exclusion limits at 95% CL on the signal strength as a function of the resonance mass obtained by combining the 8 and 13 TeV diboson searches. In each of the three plots the different colored lines correspond to the searches entering the combination.

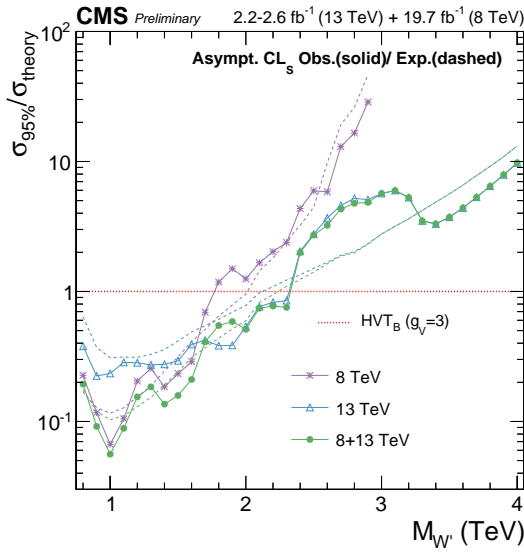


Figure 13.2: Comparison of the observed (solid) and expected (dashed) exclusion limits at 95% CL obtained by combining only 8 TeV or only 13 TeV searches to the results from the combination of all the 8 and 13 TeV results.

Table 13.2: Statistical significance of excesses observed at 1.9 TeV in the various searches, expressed in standard deviations.

Combination	W'	Z'	HVT (W' + Z')	G _{bulk}
VV 13 TeV	0.00	0.05	0.00	0.00
VV+VH 13 TeV	0.00	0.00	0.00	-
VV 8 TeV	1.20	0.46	0.91	1.05
VV 8+13 TeV	0.00	0.30	0.00	0.00
VH 8 TeV	2.17	1.41	1.78	-
VV+VH 8 TeV	2.32	1.02	1.89	-
VV+VH 8+13 TeV	0.33	0.00	0.20	-

Table 13.3: Statistical significance of excesses observed at 2 TeV in the various searches, expressed in standard deviations.

Combination	W'	Z'	HVT (W' + Z')	G _{bulk}
VV 13 TeV	0.00	0.07	0.00	0.00
VV+VH 13 TeV	0.00	0.00	0.00	-
VV 8 TeV	0.77	0.75	0.76	0.44
VV 8+13 TeV	0.23	0.45	0.29	0.06
VH 8 TeV	0.00	0.00	0.00	-
VV+VH 8 TeV	0.58	0.60	0.48	-
VV+VH 8+13 TeV	0.00	0.00	0.00	-

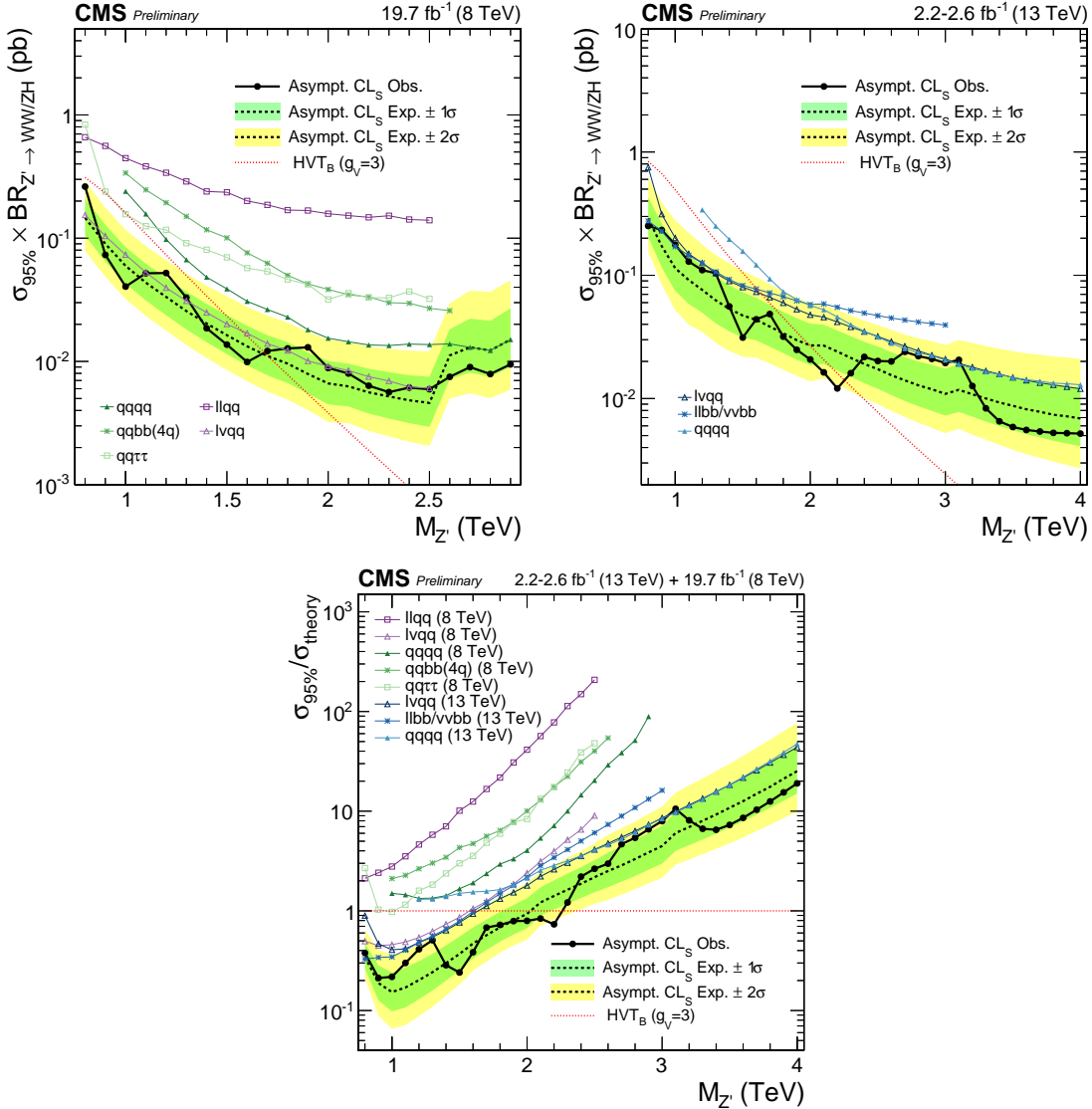


Figure 13.3: (top left) Observed (black solid) and expected (black dashed) exclusion limits at 95% CL on $\sigma(pp \rightarrow Z' \rightarrow WW/ZH)$ as a function of the resonance mass obtained by combining the 8 TeV diboson searches. The curve corresponding to the cross sections predicted by the HVT model B is overlaid. (top right) Observed (black solid) and expected (black dashed) exclusion limits at 95% CL on $\sigma(pp \rightarrow Z' \rightarrow WW/ZH)$ as a function of the resonance mass obtained by combining the 13 TeV diboson searches. The curve corresponding to the cross sections predicted by the HVT model B is overlaid. (bottom) Exclusion limits at 95% CL on the signal strength as a function of the resonance mass obtained by combining the 8 and 13 TeV diboson searches. In each of the three plots the different colored lines correspond to the searches entering the combination.

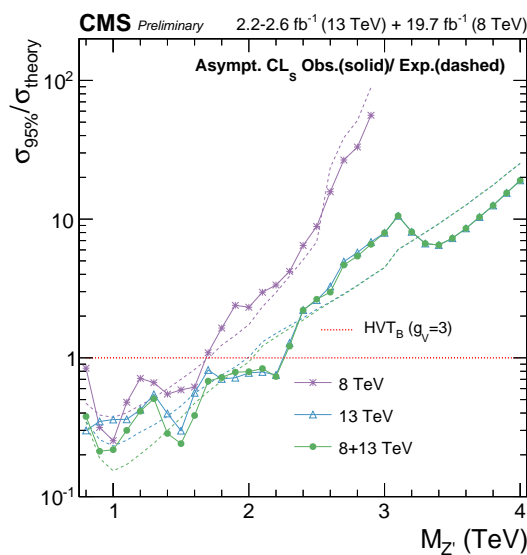


Figure 13.4: Comparison of the observed (solid) and expected (dashed) exclusion limits at 95% CL obtained by combining only 8 TeV or only 13 TeV searches to the results from the combination of all the 8 and 13 TeV results.

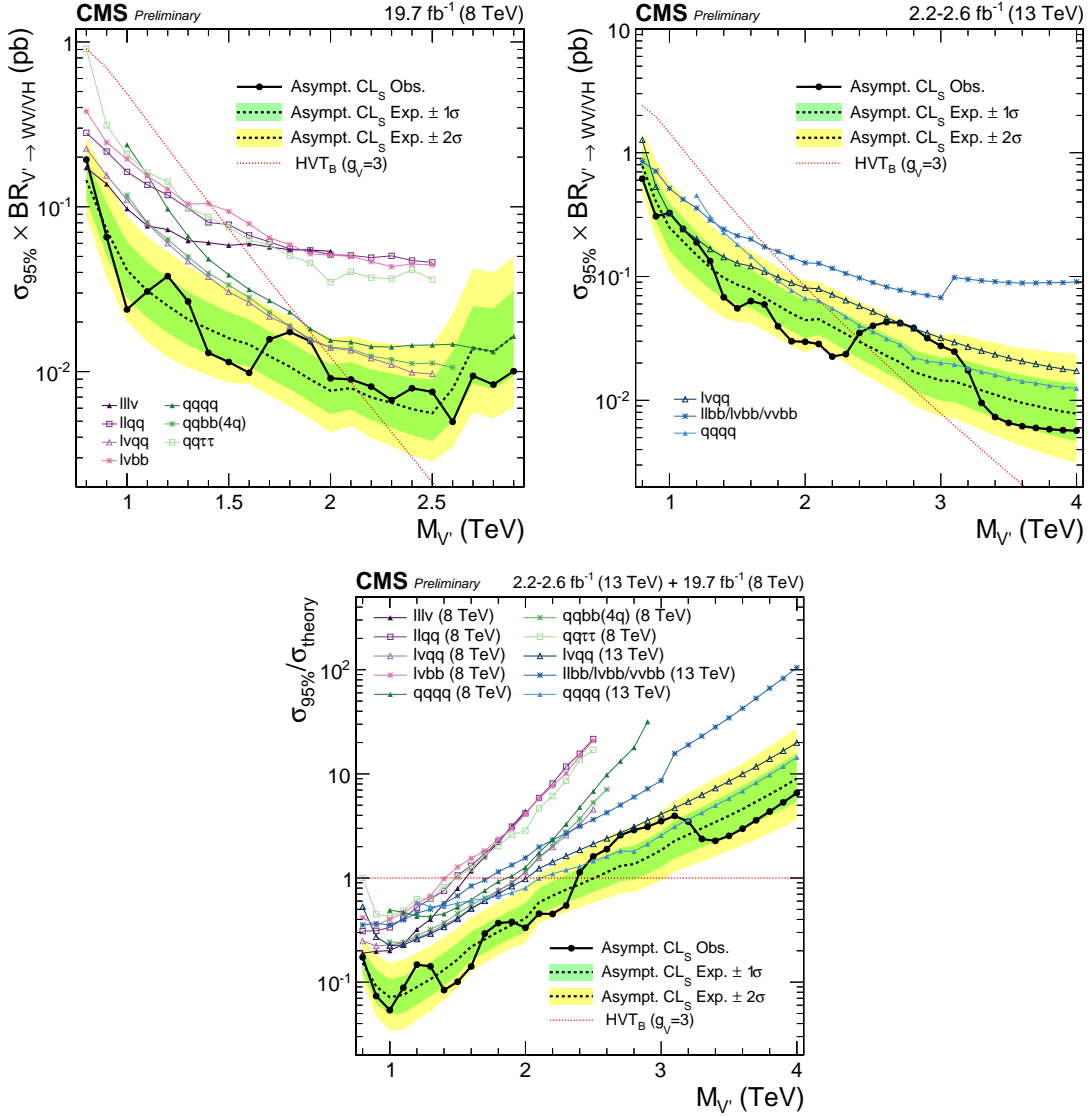


Figure 13.5: (top left) Observed (black solid) and expected (black dashed) exclusion limits at 95% CL on $\sigma(pp \rightarrow V' \rightarrow WV/VH)$ ($V' = W', Z'$ and $V=W,Z$) as a function of the resonance mass obtained by combining the 8 TeV diboson searches. The curve corresponding to the cross sections predicted by the HVT model B is overlaid. (top right) Observed (black solid) and expected (black dashed) exclusion limits at 95% CL on $\sigma(pp \rightarrow V' \rightarrow WV/VH)$ as a function of the resonance mass obtained by combining the 13 TeV diboson searches. The curve corresponding to the cross sections predicted by the HVT model B is overlaid. (bottom) Exclusion limits at 95% CL on the signal strength as a function of the resonance mass obtained by combining the 8 and 13 TeV diboson searches. In all the three plots the different colored lines correspond to the searches entering the combination.

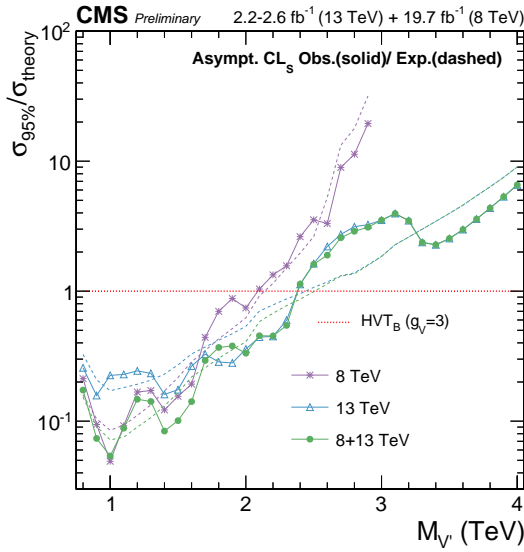


Figure 13.6: Comparison of the observed (solid) and expected (dashed) exclusion limits at 95% CL obtained by combining only 8 TeV or only 13 TeV searches to the results from the combination of all the 8 and 13 TeV results.

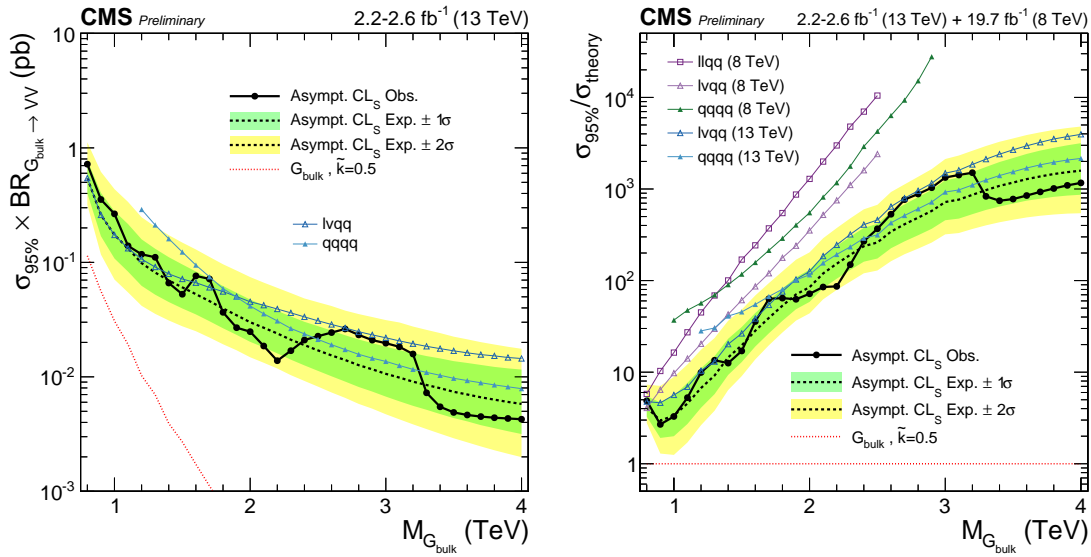


Figure 13.7: (left) Observed (black solid) and expected (black dashed) exclusion limits at 95% CL on $\sigma(pp \rightarrow G_{\text{bulk}} \rightarrow VV)$ ($V=W,Z$) as a function of the resonance mass obtained by combining the 13 TeV diboson searches. The curve corresponding to the cross sections predicted by bulk graviton model is overlaid. (right) Exclusion limits at 95% CL on the signal strength as a function of the resonance mass obtained by combining the 8 and 13 TeV diboson searches. In all the three plots the different colored lines correspond to the searches entering the combination.

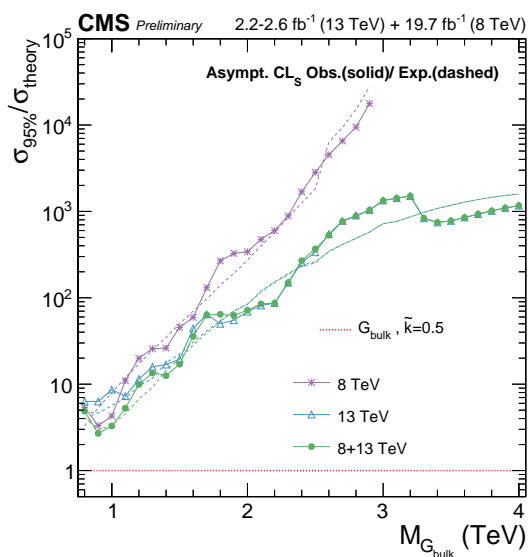


Figure 13.8: Comparison of the observed (solid) and expected (dashed) exclusion limits at 95% CL obtained by combining only 8 TeV or only 13 TeV searches to the results from the combination of all the 8 and 13 TeV results.

CHAPTER 14

Conclusions

Part II

Calibration and Upgrade of the CMS Pixel Barrel Detector

introduction chapter: why pixels are so important for physics

The CMS Pixel Barrel Detector

16.1 Design of the CMS Pixel Barrel Detector

16.2 Detector modules

16.2.1 Sensor

16.2.2 Readout Chip

16.2.3 Token Bit Manager

16.3 Readout and control system

16.3.1 Analog readout chain

16.3.2 Front End Driver

16.3.3 Supply Tube

16.3.4 Communication and Control Unit

16.3.5 Front End Controller

16.4 Pixel Online Software

16.5 Performance at $\sqrt{s} = 8$ and 13 TeV

Optimization and commissioning for LHC Run II

17.1 Radiation damage after LHC Run I

17.2 Optimization for LHC Run II

17.2.1 Overview of pixel calibrations

17.2.2 Temperature dependence

17.3 Commissioning for LHC Run II

17.3.1 Installation into CMS

17.3.2 Check out of optical connections

17.3.3 Adjustment of readout chain settings

17.3.4 Optimisation of signal performance

Phase I Upgrade of the CMS Pixel Barrel Detector

18.1 Motivations

18.2 Summary of changes

18.3 The digital readout chain

18.4 The Phase I supply tubes

18.5 The test stand

18.6 Supply tubes assembly and commissioning

18.7 Detector commissioning

CHAPTER 19

Conclusions

Part III

Summary

